UNIVERSITÄT
LEIPZIG

REPORT
Halbleiterphysik
Semiconductor Physics
2018

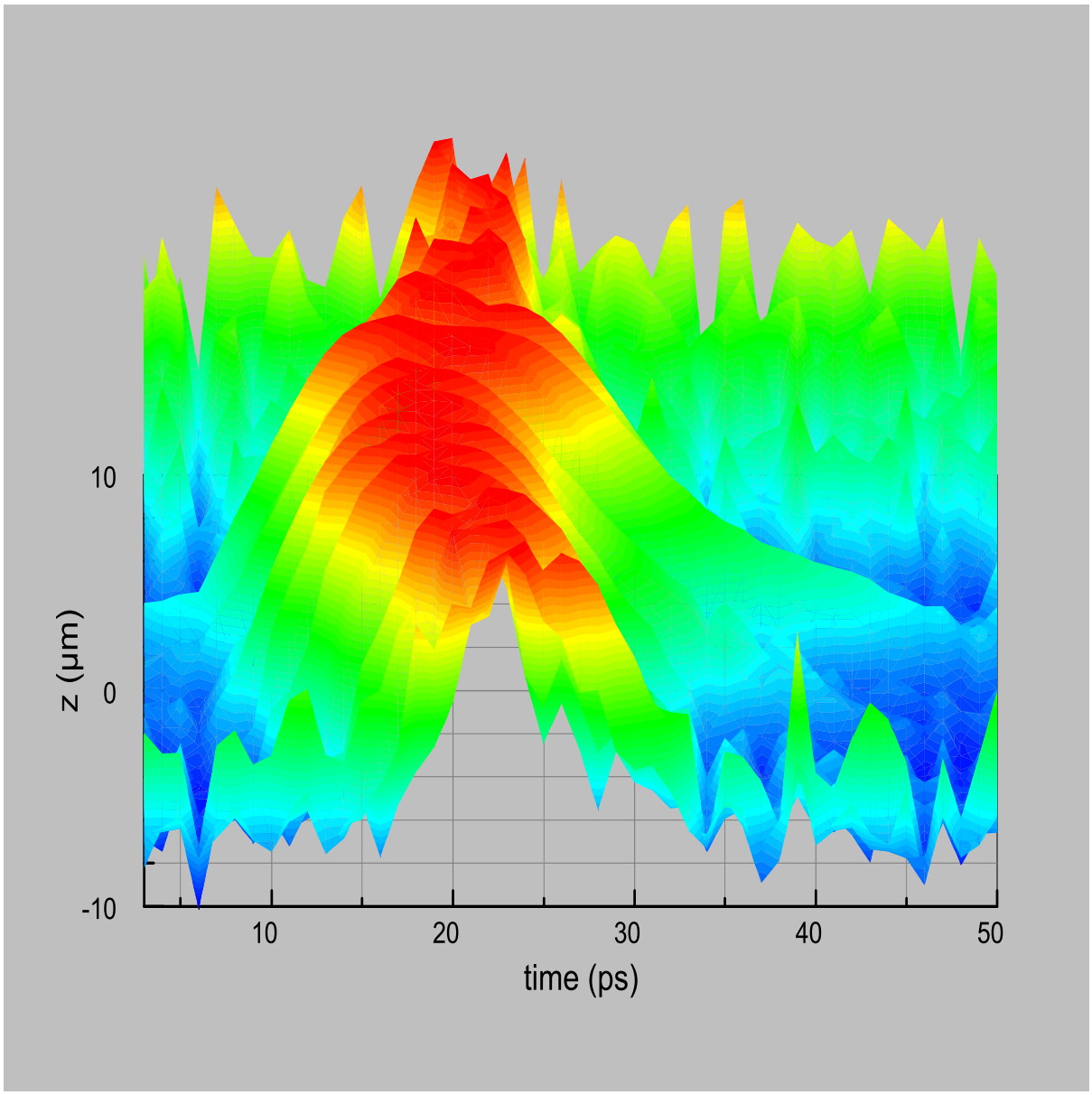

The Semiconductor Physics Group of Universität Leipzig, Report 2018
M. Grundmann (Ed.)

Technical Editor: Anja Heck

online available at
http://research.uni-leipzig.de/hlp/

Front cover

■ Spatiotemporal evolution of a whispering gallery mode exciton-polariton Bose-Einstein condensate at 3.188 eV in a ZnO microwire after femtosecond-excitation with a one micrometer sized laser spot. The emission intensity is colour coded. Within 10 ps, the condensate spreads along the microwire axis about ± 10 μm (z-direction in the image) and was observed as long as 40 ps. ("Spatiotemporal evolution of coherent polariton modes in ZnO microwire cavities at room temperature", T. Michalsky, M. Wille, M. Grundmann, and R. Schmidt-Grund, Nano Letters **18**, 6820 (2018)).

Back cover

■ Scanning electron microscopy image of a γ-CuI thin film on a glass substrate, proposed conduction paths of holes (blue) as well as electrons in a two-dimensional electron gas (2DEG, red) are indicated. The electrical transport properties of such highly textured γ-CuI thin films were described in detail by our group in Advanced Materials Interfaces **5**, 1701411 (2018). The hole transport in this p-type material is dominated by a tunneling mechanism across grain boundaries. A defect band located at these boundaries forms a 2DEG and results in the band bending required for tunneling transport. The inset shows such a grain boundary in magnified view with the corresponding band bending, the possible location of the defect band (white/red rectangle) and the tunneling path of the holes through the grain boundary.

Abteilung Halbleiterphysik

Felix-Bloch-Institut für Festkörperphysik

Fakultät für
Physik und Geowissenschaften

Universität Leipzig

Semiconductor Physics Group

Felix Bloch Institute for Solid State Physics

Faculty of Physics and Earth Sciences

Universität Leipzig

Report 2018

Address

Semiconductor Physics Group

Linnéstraße 5
D-04103 Leipzig, Germany

Phone: +49 341 97-32650
Fax: +49 341 97-32668
WWW: http://research.uni-leipzig.de/hlp/
Mailing address: Postfach 230001, D-04081 Leipzig, Germany

Preface

Our research report gives you a summery of the recent activities and discoveries of the Semiconductor Physics group. We hope it finds your interest and gives you a scientific stimulus. Among others, you will find novel findings on fundamental aspects of optical activity and the gyrotropy tensor using KTP as model material, ultrafast time-resolved ellipsometry on ZnO, sesquioxide alloys and strained heterostructures in the $(In,Al,Ga)_2O_3$ system and experimental evidence for exceptional 'Voigt' points and their topology in anisotropic ZnO-based microcavities among other topics.

A highlight of the year was the first Felix Bloch Lecture Leipzig on "Controlling Spin Dynamics with Light" delivered by Prof. Theo Rasing from the Institute of Molecules and Materials of Radboud University Nijmegen. Afterwards, a bronze plate with the portrait of Felix Bloch by Leipzig sculptor Markus Gläser was unveiled in the foyer of the physics building in the presence of Felix Bloch's son Frank and grandson Elias.

We have developed and experimentally investigated our theory of pseudomorphic strain in heterostructures with arbitrary interface orientation for rhombohedral/trigonal (and thus also hexagonal) and monoclinic (and thus also orthorhombic, tetragonal and cubic) crystal classes.

This is of particular relevance for $(Al,Ga)_2O_3$ layers on (monoclinic) β-Ga_2O_3 and (rhombohedral) α-Al_2O_3 substrates. The pulsed laser deposition used for the fabrication of such heterostructures has been ameliorated with the concept of continuous vertical composition spreads through the use of elliptically segmented targets (Chap. 2.1); for this work Max Kneiß has received the BuildMoNa Award 2019 (first prize).

We like to draw your attention to the fact that a long-standing issue has been solved within a fruitful cooperation with Humboldt Universität. The Schottky contact between a noble metal oxide (PtO_x) and an oxide semiconductor (zinc-tin-oxide, ZTO) is indeed proven to be of Schottky-type since due to reduction of the noble metal oxide, the contact contains a pure metal layer. Connected to the role of oxygen vacancies is a long paper summarizing many years of DLTS research on the E3 level in ZnO.

We are largely indebted to our funding agencies in particular Deutsche Forschungsgemeinschaft (DFG). We are grateful for the continued funding of Sonderforschungsbereich SFB 762 "Functionality of Oxide Interfaces" that runs in its final period (2016–2019) and our project on nanowire heterostructures in the Forschergruppe FOR 1616 "Nanowire Optoelectronics" which has concluded by now (2015–2018). Sächsische Aufbaubank (SAB) is supporting our efforts on combinatorial pulsed laser deposition within the new project COSIMA (2017–2020) that has enriched our group with a Müller matrix ellipsometer, a low-temperature Hall effect wafer prober and a new laboratory for combinatorial pulsed laser deposition. Our project on flexible oxide electronic circuits is funded in the DFG SPP FFLexCom (SPP 1796) and has been renewed (2015–2021). Work has begun in the ZONE project on (Mg,Zn)(O,N) thin films in a joint ANR-DFG project together with CNRS-CRHEA, Valbonne. The work of our students, researchers and guests together with our academic and industrial partners near and far was fruitful and enjoyable and thus it is with great pleasure that the Semiconductor Physics Group presents their progress report.

Leipzig,
March 2019

Marius Grundmann

Contents

I

Report of the Semiconductor Physics Group

1

Structure and Staff of the Semiconductor Physics Group

Prof. Dr. Marius Grundmann

Secretary

Anja Heck
Sandra Meurer
Birgit Wendisch

Technical staff

Dipl.-Phys. Gabriele Benndorf
Monika Hahn
Dipl.-Ing. Holger Hochmuth
Dipl.-Phys. Jörg Lenzner
Axel Märcker
Gabriele Ramm
Roswitha Riedel
Dipl.-Ing. Ulrike Teschner

Academic staff

Dr. Robert Karsthof
Prof. Dr. Michael Lorenz
PD Dr. Rainer Pickenhain
Dr. Anna Reinhardt
Prof. Dr. Bernd Rheinländer (retired)
Dr. Peter Schlupp
Dr. Rüdiger Schmidt-Grund
Dr. Daniel Splith
Dr. Chris Sturm
Dr. Holger von Wenckstern
Dr. Chang Yang
Dr. Zhipeng Zhang

PhD candidates

Michitaka Fukumoto, M.Sc. (guest)
Oliver Herrfurth, M.Sc.
Stefan Hohenberger, M.Sc.
Tanja Jawinski, M.Sc.
Max Kneiß, M.Sc.
Evgeny Krüger, M.Sc.
Tillmann Stralka, M.Sc.
Lukas Trefflich, M.Sc.
Sofie Vogt, M.Sc.
Antonia Welk, M.Sc.
Anna Werner, M.Sc.
Vitaly Zviagin, M.Sc.

Students

Yousif Abou Leila
Michael Bar
Felix-Florian Delatowski
Sebastian Henn
Ron Hildebrandt
Florian Jung
Mizuki Kakei
Mario Klebahn
Cathatina Krömmelbein
Oliver Lahr
Sandra Montag
Andreas Müller
Sophie Müller
Andre Nabatov Sergi Ortega Micó
Eduard Rose
Fabian Schöppach
Philipp Storm
Laurenz Thyen
Christopher Walter
Benjamin Wehr
Jonathan Wernersson

2

Reports

2.1 Pulsed laser deposition with radially segmented targets for compositional gradients in growth direction

M. Kneiß, P. Storm, G. Benndorf, M. Grundmann, H. von Wenckstern

For researchers growing and studying functional layers, the precise control of the composition of thin film in devices is highly desired. Be it impurity doping for conductivity control, ternary alloy compositions for devices utilizing heterostructures, such as quantum-well LEDs or infrared photodetectors as well as MODFETS, or composition graded buffer layers to compensate for lattice mismatches towards cost-effective substrate materials [1]. Pulsed laser deposition (PLD) is a powerful tool for the growth of highly crystalline thin film layers mostly transferring the stoichiometry of the employed target material to the layer deposited. Therefore, to induce a variation of the thin film composition, the composition of particle flux needs to be adjustable, which is an established method for techniques such as molecular beam epitaxy or metal-organic chemical vapor deposition. In PLD, this requires the use of a different target or complicated multi-beam [2] or mirror setups [3].

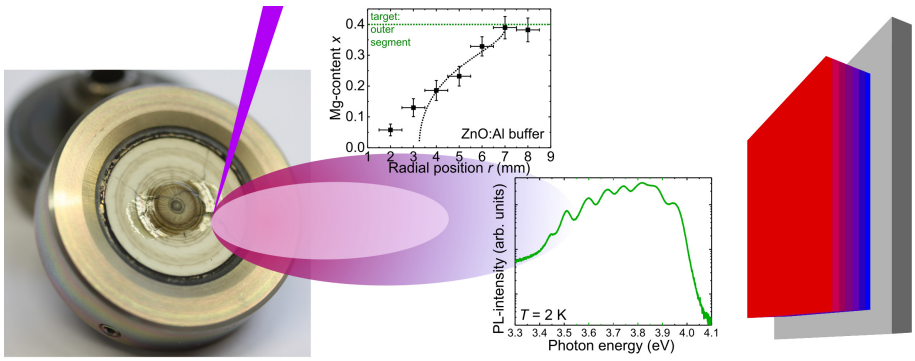

Figure 2.1: Elliptically-segmented $Mg_{0.4}Zn_{0.6}O/ZnO$ target used in this study after several depositions. The schematic on the right shows the variation of the Mg content in growth direction. The inset graphics show the low-temperature photoluminescence spectrum of such a composition-graded thin film and the incorporated Mg-content in dependence on the radial position of the laser spot on the target determined for homogeneous layers.

Until now, the variation of the particle flux composition was not possible in PLD by ablating a single target only, not to speak of a continuous composition grading in growth direction of a thin film. We already have reported about a continuous composition spread technique employing segmented targets that resulted in a lateral composition variation on the substrate wafer [4]. However, thin films with a well-defined and controllable composition as well as composition gradients in growth direction are not possible with this technique. Both of these issues can be addressed by an approach employing radially-segmented targets which we have developed [5], in particular we use elliptically-segmented targets where the inner segment has a different composition than the outer segment, see also Figs. 2.1 and 2.2.

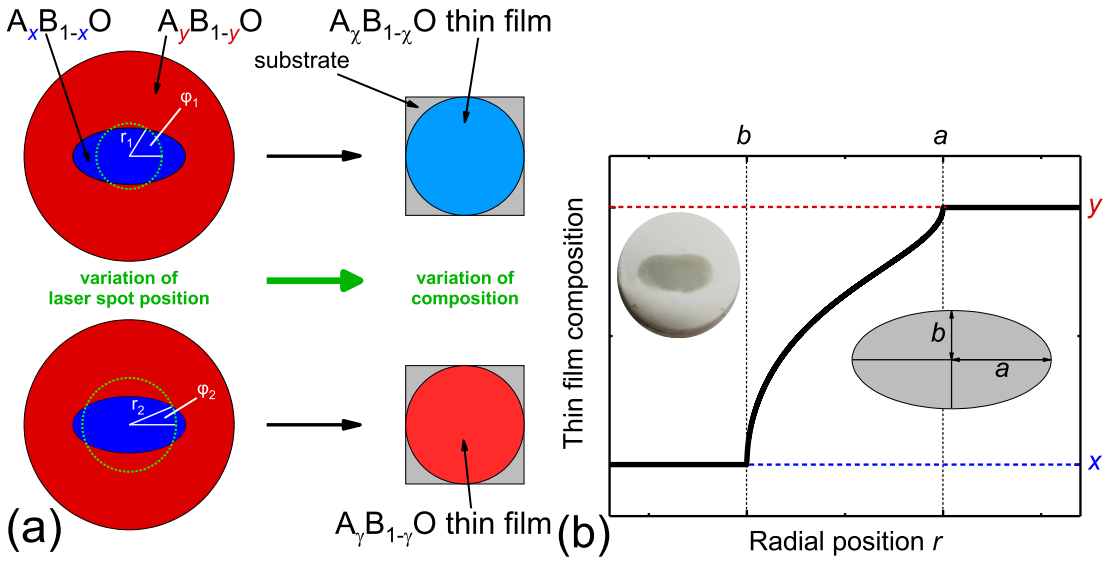

Figure 2.2: (a) Schematic depiction of the increase of path length ratio of the track of the laser spot in the outer segment to the inner segment when the radial position of the laser spot is increased from r_1 to r_2 on a rotating target. The corresponding change in the average particle flux composition in the PLD plasma results in different thin film compositions χ and γ for the two radial positions. (b) Expected thin film composition in dependence on the radial position r of the laser spot on the target assuming an ideal point-like laser spot and stoichiometric transfer of the target material. The inset shows the $Mg_{0.4}Zn_{0.6}O/ZnO$ target prior to deposition.

In our standard PLD approach, the target would be rotated and the radial position of the laser spot on the target surface changed continuously to ensure a homogeneous ablation of the target surface. For the novel technique, we fix the radial position of the laser spot such that the laser ablates a circular track on the target surface, see also Fig. 2.2 (a). The laser now ablates alternatingly the outer and the inner segment of the target, such that the particle flux composition is changing constantly between the stoichiometry of outer and inner segment. The thin film composition resulting from this circular ablation is given by the time-average of the particle flux composition, which in turn is given by the path length ratio of the laser spot between outer and inner segment of the target. Calculating the expected thin film composition theoretically, assuming an ideal point-like laser spot and a stoichiometric transfer from the target, gives the curve displayed in Fig. 2.2 (b) enabling a continuous variation of the thin film composition. This both enables the deposition of homogeneous thin films with any desired cation ratio between that of the inner and outer segment as well as the growth of layers with

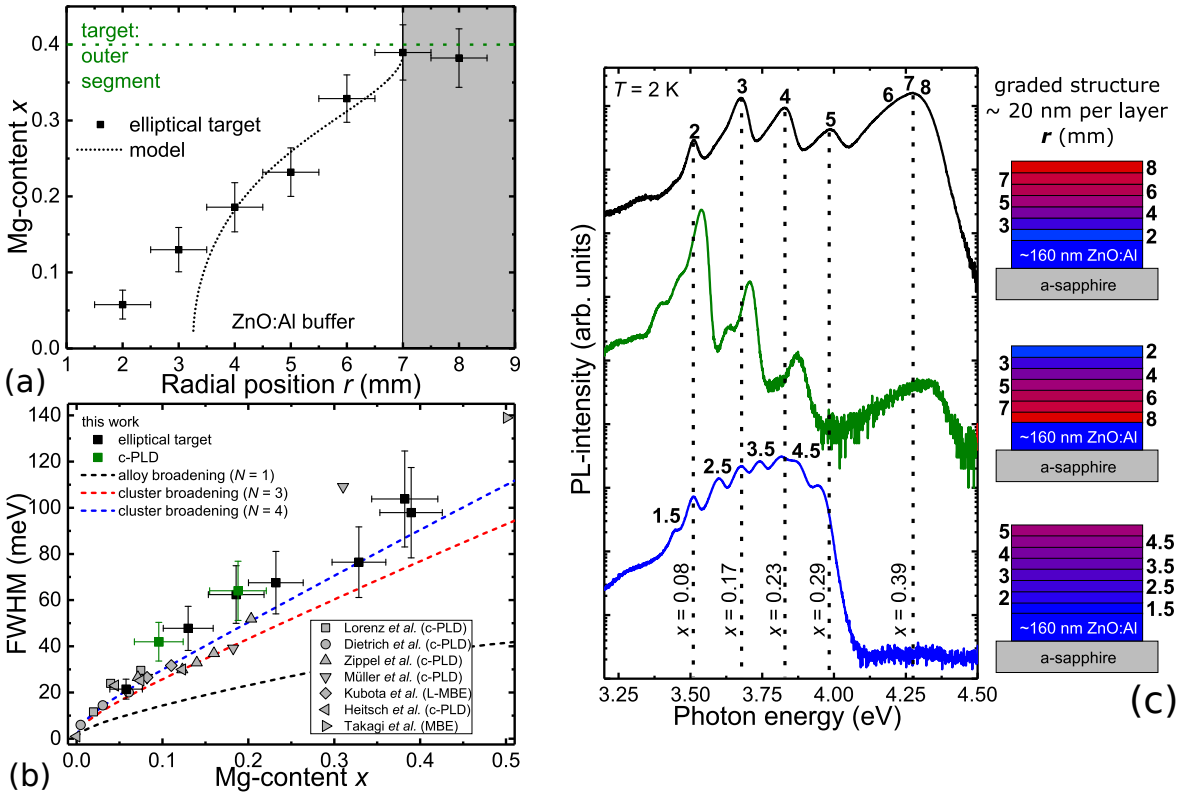

Figure 2.3: (a) Mg-content x of homogeneous $Mg_xZn_{1-x}O$ layers on Al-doped ZnO buffer layers in dependence on the radial position r. The ideal model curve of the expected composition is given as black dashed line. (b) Broadening (full width at half maximum FWHM) of the excitonic emission peak in low-temperature PL spectra of the homogeneous layers in dependence on their Mg-content and in comparison to literature values [6–12] as well as samples grown by conventional PLD. Dashed lines are theoretical models for alloy broadening. (c) Low temperature PL spectra of thin films with composition gradient in growth direction. Schematic of the structures are given next to the spectra with the corresponding value of r for each layer.

a composition gradient in growth direction when the radial position is varied in-situ. We therefore call this technique vertical continuous composition spread (VCCS). We employed an elliptically-segmented $Mg_{0.4}Zn_{0.6}O$/ZnO target (shown in the inset in Fig. 2.2 (b) prior to and in Fig. 2.1 after several depositions). We have grown both homogeneous $Mg_xZn_{1-x}O$ thin films with a thickness of ≈ 40 nm on Al-doped ZnO buffer layers as well as layer systems with a step-graded composition variation in growth direction. We could show that we can vary the Mg-content in the thin films within the whole composition range of the target with reasonable agreement of the radial dependence to the model theory, see Fig. 2.3 (a). From low-temperature photoluminescence (PL) measurements, it was further confirmed that a homogeneous distribution of Mg-atoms in the layers occurred. The broadening of the excitonic emission of the alloy layers (Fig. 2.3 (b)) is similar to thin films grown by conventional PLD, literature data and model curves. X-ray diffraction and atomic force microscopy confirmed similar structural and surface quality of our layers compared to conventional PLD (not shown). In low-temperature PL measurements of the step-graded $Mg_xZn_{1-x}O$ thin films, excitonic emission peaks could be identified for each layer (Fig. 2.3 (c)). Their energetic positions are in agreement with the expected Mg-content for the respective radial positions. Even

narrow graded thin films with well-pronounced emission peaks corresponding to each layer in the structure are possible (Fig. 2.3 (c) lowest curve). Therefore, a significant diffusion of Mg-atoms between the single layers can be excluded. With this, we have clearly demonstrated that we have developed a practically applicable PLD technique for the growth of homogeneous layers with any desired composition as well as composition gradients in growth direction. Since nearly any alloy system or impurity dopant is within the reach of this technique, there are numerous applications possible, such as strain engineering, dopant profiling, the creation of discrete material libraries or precise band gap engineering for heterostructures.

[1] Inoue *et al.*, IEEE Trans. Electron Devices **55**, 483 (2008)
[2] Eason *et al.*, J. Phys. D: Appl. Phys. **47**, 034007 (2014)
[3] Fischer *et al.*, Rev. Sci. Instrum. **83**, 043901 (2012)
[4] von Wenckstern *et al.*, CrystEngComm **15**, 10020 (2013)
[5] Kneiß *et al.*, ACS Comb. Sci. **20**, 643 (2018)
[6] Takagi *et al.*, Jpn. J. Appl. Phys. **42**, L401 (2003)
[7] Heitsch *et al.*, J. Appl. Phys. **101**, 083521 (2007)
[8] Müller *et al.*, J. Appl. Phys. **107**, 013704 (2010)
[9] Kubota *et al.*, Appl. Phys. Lett. **90**, 141903 (2007)
[10] Lorenz *et al.*, Thin Solid Films **518**, 4623 (2010)
[11] Zippel *et al.*, J. Lumin. **130**, 520 (2010)
[12] Dietrich *et al.*, New J. Phys. **12**, 033030 (2010)

2.2 Strain in pseudomorphic rhombohedral/trigonal heterostructures

M. Grundmann

Epitaxial heterostructures are the basis of basically all modern devices. Generally, they involve materials with different lattice constants, leading to pseudomorphic strain for layer thickness below the onset of plastic relaxation. First this has been investigated for cubic materials, such as silicon and III-V semiconductors, also representing the simplest case. Then, wurtzite-based heterostructures were investigated for GaN- and ZnO-based heterostructures; here polar, non-polar and semi-polar directions arise [1]. Recently, monoclinic heterostructures based on β-Ga_2O_3 were theoretically treated by us [2].

Here, we discuss pseudomorphic heterostructures of corundum-structure materials, i.e. in particular rhombohedral, α-phase $(Al,Ga)_2O_3$ layers on alumina [3]. The usual unit cell of alumina is depicted in Fig. 2.4.

We have calculated analytically, in the framework of linear elastic continuum theory, the epitaxial in-plane and out-of-plane strain components for pseudomorphic growth of rhombohedral heterostructures for all substrate orientations, including the c-, a-, m-, n-, and r-planes [3]. Numerical examples were given for the sesquioxide semiconductor system of Al-rich $(Al,Ga)_2O_3/Al_2O_3$. From the deformation of the unit cell, various X-ray peak positions and lattice plane tilts have been calculated. In Fig. 2.5 the r-plane

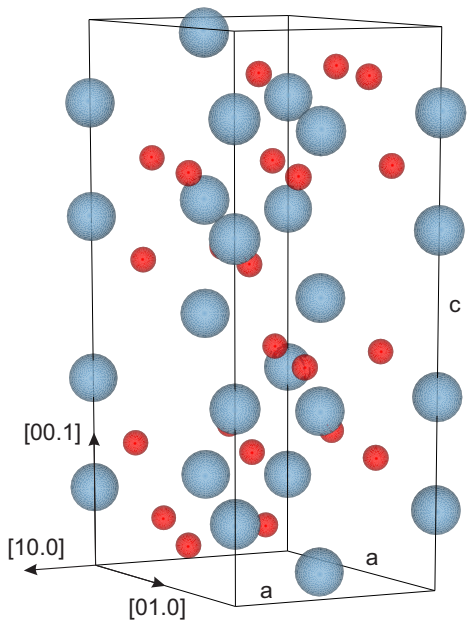

Figure 2.4: One sixth of the hexagonal unit cell of rhombohedral α-Al_2O_3 (oxygen atoms are shown in red, aluminum atoms in blue). The crystal directions and lattice constants are indicated. Figure prepared with VESTA [4].

(out-of-plane) lattice constant is depicted for pseudomorphic and fully relaxed growth on r-plane alumina.

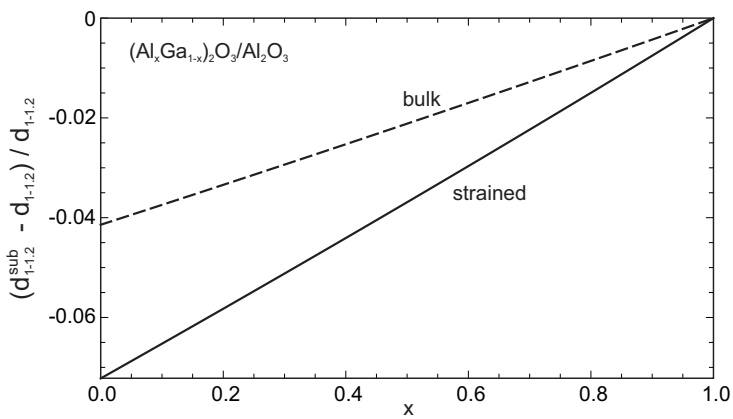

Figure 2.5: Bulk/relaxed and pseudomorphically strained r-plane (out-of-plane) lattice constant relative to the substrate lattice constant of α-phase $(Al_xGa_{1-x})_2O_3$ on r-plane Al_2O_3.

We note that by setting the elastic constant C_{14} to zero, our theory covers as well the simpler case of hexagonal (wurtzite) heterostructures discussed in [1].

[1] M. Grundmann, Jesús Zúñiga-Pérez, *Pseudomorphic ZnO-based heterostructures: from polar through all semipolar to nonpolar orientations*, phys. stat. sol. (b) **253**, 351–360 (2016)

[2] M. Grundmann, *Strain in Pseudomorphic Monoclinic Ga_2O_3-based Heterostructures*, phys. stat. sol. (b) **254**, 1700134 (2017)

[3] M. Grundmann, *Elastic Theory of Pseudomorphic Monoclinic and Rhombohedral Heterostructures*, J. Appl. Phys. **124**, 185302:1-10 (2018)

[4] K. Momma, F. Izumi, *VESTA 3 for three-dimensional visualization of crystal, volumetric and morphology data*, J. Appl. Crystallogr. **44**, 1272–1276 (2011)

2.3 Pseudomorphic growth of $(Al_{1-x}Ga_x)_2O_3$ thin films on R-plane sapphire

M. Lorenz, S. Hohenberger, E. Rose, M. Grundmann

Single-crystalline α-$(Al,Ga)_2O_3$ is interesting for the fabrication of high-quality semiconductor and dielectric heterostructures due to the similar ionic radii and the availability of high-quality sapphire substrates [1]. From the literature review published in [1], a clear gap is visible for epitaxial growth of α-$(Al_{1-x}Ga_x)_2O_3$ films on the Al-rich side. Therefore, the aim of this work [1] was to demonstrate coherent pseudomorphic growth of α-$(Al_{1-x}Ga_x)_2O_3$ films on R-plane (01.2) sapphire substrates. Eventually, such thin films can be used in dielectric superlattices.

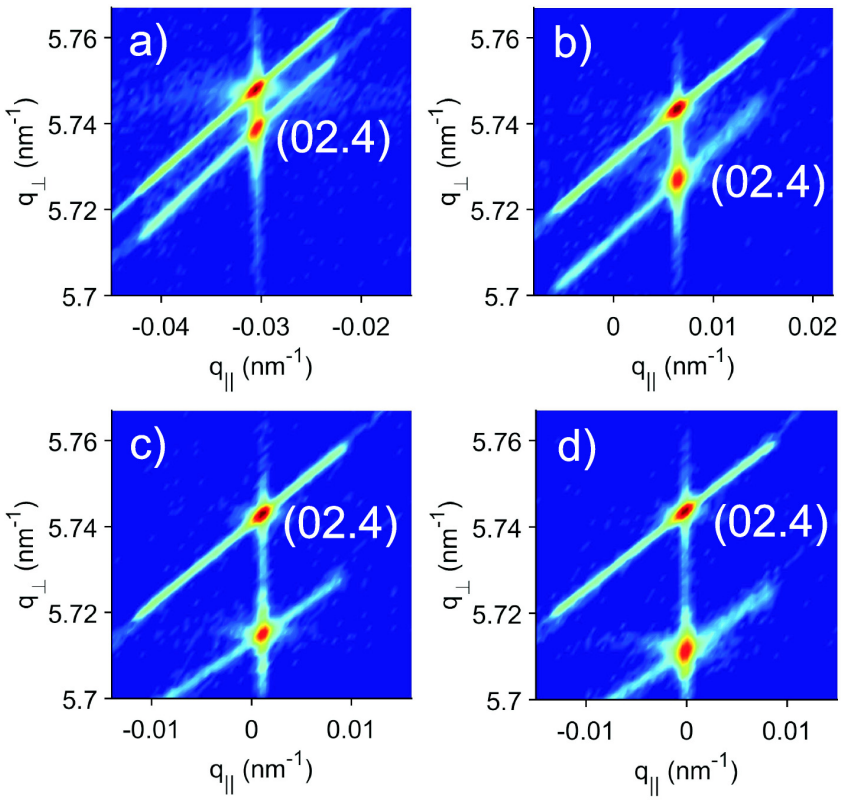

Figure 2.6: RSMs around symmetric (02.4) reflections, measured with the fast frame-based option of the PIXcel^{3D} detector of samples with increasing Ga-content, i.e. increasing peak splitting: a) x = 0.0209, b) x = 0.0377, c) x = 0.0635, and d) x = 0.0745. The more intense upper peak stems from the substrate in all maps. Figure adopted from [1].

Atomically smooth, pseudomorphic $(Al_{1-x}Ga_x)_2O_3$ thin films were grown for $0 \leq x < 0.08$ on R-plane sapphire (01.2) by pulsed laser deposition. The laser targets with

nominal Ga-contents x = 0, 0.1, and 0.2 were sintered pellets pressed from high purity Al_2O_3 and Ga_2O_3 powders. The oxygen partial pressure during growth was optimized to 10^{-3} mbar. The growth temperature obtained by the CO_2 laser heater was varied between 500°C and 1,000°C. Substrates were single-side epi polished r-plane sapphire (01.2) single crystals (10×10×0.5 mm^3). Films up to 720 nm thickness show atomically stepped surfaces with monolayer terraces, similar to the substrates prior to growth, for AFM images and further details see [1].

X-ray diffraction (XRD) measurements were performed using a PANalytical X'pert PRO MRD with the line focus of a copper X-ray tube. As incident beam optics either a 4×Ge(220) monochromator ($K\alpha_1$-radiation) or a parabolic mirror ($K\alpha$-radiation) was used. For detection either a secondary monochromator with proportional counter (triple-axis) or the variable receiving slit of a PIXcel^{3D} array detector was used [1]. A careful analysis of 13 symmetric, skew-symmetric and asymmetric XRD peaks agrees quite well with the continuum elastic strain theory of pseudomorphic distortion in corundum heterostructures by M. Grundmann [2].

Figure 2.6 shows reciprocal space maps (RSMs) around the symmetric (02.4) reflections, indicating the increasing splitting of substrate and film peaks with increasing Ga content x. For x = 0, no splitting was observed even in triple-axis XRD scans, indicating a perfect lattice match. Ref. [1] provides a detailed comparison on the experimental and theoretical splitting of film and substrate peaks for the 13 reflections, as well as the measured tilts of asymmetric film lattice planes. An even better overall agreement of experimental and theoretical peak splitting could be obtained using slightly modified c/a ratios, see the minor corrections of the order 10^{-4} in Table 2 of Ref. [1]. The standard deviations of the differences theory-experiment are considerably reduced by using these slightly corrected c/a ratios, indicating the very high sensitivity of the elastic theory [2] and the precision of the high-resolution XRD measurements [1].

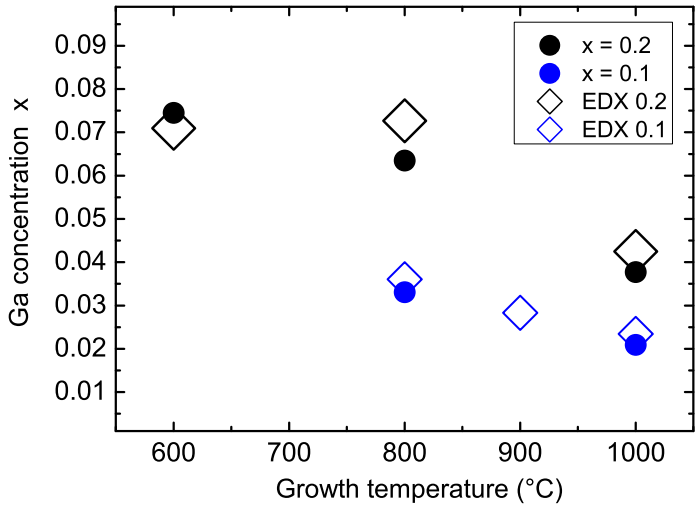

Figure 2.7: Ga-concentration x calculated from fits to experimental peak splitting *(circles)* and measured by EDX analysis *(diamonds)* in dependence of growth temperature, for films grown from PLD targets with Ga contents x = 0.1 *(blue)* and 0.2 *(black)*. Size of EDX symbols corresponds to their experimental uncertainty. Figure adopted from [1].

The Ga contents x obtained from best fits of the spacing of the (02.4), (04.8), and (00.6), (00.12) film and substrate XRD reflections is compared in Figure 2.7 with energy dispersive X-ray (EDX) analyses of the same samples. Taking into account the natural uncertainties of EDX, a reasonable agreement of theoretical and experimental Ga-contents of our epitaxial $(Al_{1-x}Ga_x)_2O_3$ films was obtained [1].

[1] M. Lorenz, S. Hohenberger, E. Rose, and M. Grundmann, Appl. Phys. Lett. **113**, 231902: 1-5 (2018)
[2] M. Grundmann, J. Appl. Phys. **124**, 185302: 1-10 (2018)

2.4 Properties of binary and ternary orthorhombic group-III sesquioxide thin films grown by pulsed laser deposition

The wide bandgap semiconductor gallium oxide has potential application in electronic high-power devices, because of its large breakdown field and high Baliga figure of merit [1]. Additional possible application fields are quantum well infrared photodetectors, UV-photodetectors, touch panel displays, or optical communication systems [2]. Ga_2O_3 can be stabilized in various polymorphs [3]. While the majority of publications focuses on the thermodynamically most stable β-phase, recently, the orthorhombic κ-phase gained interest due to its predicted large spontaneous polarization of 23 μC/cm^2 along the c-axis [4]. This would lead to a discontinuous change of the polarization at the interface of κ-Ga_2O_3 based, ternary heterostructures resulting in electron accumulation at the interface, which can be utilized to perform applications such as high-electron mobility transistors. Therefore, it is crucial to determine deposition conditions allowing the growth of binary as well as ternary layers with tailored material properties. In the following sections, we will discuss growth conditions and behavior of binary κ-Ga_2O_3 thin films grown by pulsed laser deposition (PLD) on different substrates [5]. Further, we discuss material properties of a κ-$(In_xGa_{1-x})_2O_3$ thin film grown with continuous composition spread [6] (CCS) by pulsed laser deposition on c-plane sapphire. Both, the binary and the ternary target were doped with tin to facilitate formation of the orthorhombic phase [7]. Resulting samples were investigated by means of X-ray diffraction (XRD), transmission, energy-dispersive X-ray spectroscopy (EDX), and atomic force microscopy (AFM).

2.4.1 Tin-assisted PLD-growth of binary κ-Ga_2O_3 thin films

M. Kneiß,* A. Hassa,* D. Splith,* C. Sturm,* H. von Wenckstern,* T. Schultz,† N. Koch,† M. Lorenz,* and M. Grundmann*

*Universität Leipzig, Felix-Bloch-Institut für Festkörperphysik
†Humboldt Universität zu Berlin, Institut für Physik

Kracht *et al.* [7] found that offering tin as as a catalyst during molecular beam epitaxy (MBE) of Ga_2O_3 is beneficial for stabilizing the κ-phase on c-plane sapphire. Similarly,

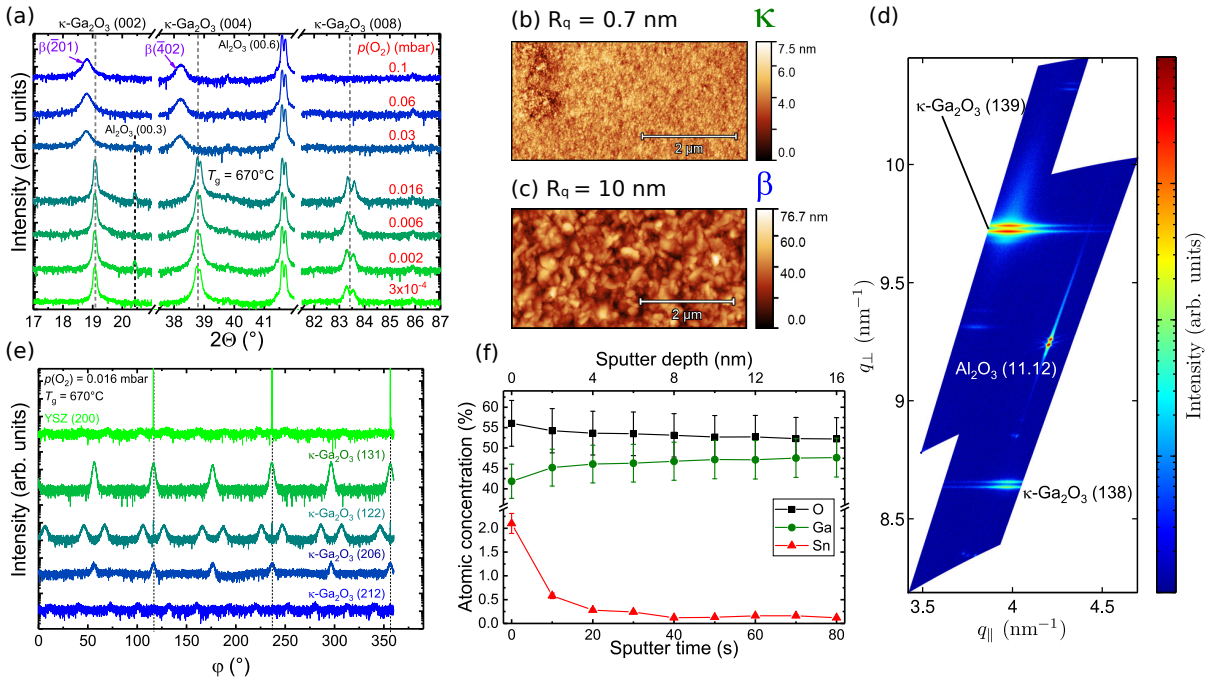

Figure 2.8: (a) XRD 2θ-ω scans of a series of Ga_2O_3 thin films deposited via PLD from a tin-doped target on c-sapphire substrates at various oxygen partial pressures $p(O_2)$ and a substrate temperature $T_g = 670°C$. (b) and (c): AFM images of Ga_2O_3 thin films in the (b) κ- and (c) β-phase. The thin films were deposited at nominally identical process parameters of $p(O_2) = 0.016$ mbar and $T_g = 670°C$ from a (b) tin-doped and (c) nominally undoped target. RMS roughness R_q as indicated. (d) Reciprocal space map of a κ-Ga_2O_3 thin film on c-sapphire around the asymmetric Al_2O_3(11.12) reflection. (e) XRD ϕ scans of a κ-Ga_2O_3 thin film on YSZ(111) for several skew-symmetric substrate and film reflections as indicated. (f) Depth-resolved atomic concentrations of Ga, O and Sn for a κ-Ga_2O_3 thin film on c-sapphire determined from depth-resolved XPS measurements.

for PLD grown thin films, Orita et al. [8] obtained thin films in the κ-phase under certain conditions by employing tin-doped targets. To shed a light on the growth mechanism of this phase in PLD and the determination of important material parameters, we performed an in-depth investigation on Ga_2O_3 thin films grown from tin-containing targets ($Ga_2O_3 + 1$ wt.% SnO_2) on various substrates such as c-sapphire, YSZ(111), STO(111), and MgO(111) [5]. Upon a variation of the oxygen partial pressure ($p(O_2)$) during the PLD process, we found that the orthorhombic κ-phase can be synthesized only for $p(O_2) \leq 0.016$ mbar, while for higher pressures the thin films crystallize in the thermodynamically stable monoclinic β-phase. Further, for a given $p(O_2)$ the critical pressure of 0.016 mbar, the κ-phase is only stabilized at growth temperatures above 500°C. Apparent is the significant increase in intensity and decrease of the broadening of the reflections in XRD 2θ-ω scans of the thin films in the κ-phase as compared to those in the β-phase, as shown in Fig. 2.8(a). At the same time, for identical process parameters, thin films grown from nominally undoped targets crystallize solely in the β-phase with much larger surface roughnesses, as revealed by AFM images in Fig. 2.8(b) and (c), emphasizing the superior surface quality of thin films in the κ-phase. Rocking curve measurements as well as reciprocal space maps (see e.g. Fig. 2.8(d)) proved once more the high crystalline quality of the κ-phase thin films. Lattice parameters determined from

these measurements (a = 5.053 Å, b = 8.701 Å and c = 9.265 Å) are in good agreement to literature data [9]. We were further able to unambiguously prove the orthorhombic symmetry of the κ-phase as well as the epitaxial growth on all used substrates by XRD ϕ-scans of several skew-symmetric film and substrate reflections (see Fig. 2.8(e) for a thin film on YSZ(111)). The twelve-fold occurring (122) and (212) reflections are only expected in the orthorhombic system. Correspondingly, we found epitaxial growth of the thin films in three rotational domains rotated by 120° with respect to each other. The in-plane epitaxial relationships were determined as α-Al_2O_3 $\langle\bar{1}0.0\rangle||\langle010\rangle$ κ-Ga_2O_3 and α-Al_2O_3 $\langle\bar{1}2.0\rangle||\langle100\rangle$ κ-Ga_2O_3 for c-sapphire as well as cubic $\langle\bar{2}11\rangle||\langle100\rangle$ κ-Ga_2O_3 and cubic $\langle0\bar{1}1\rangle||\langle010\rangle$ κ-Ga_2O_3 for the cubic substrates. To further clarify the role of tin for the PLD growth of the κ-phase, depth-resolved X-ray photoelectron spectroscopy (XPS) measurements were performed. The resulting atomic concentrations of the elemental species Ga, O and Sn are shown in dependence on the sputtering depth in Fig. 2.8(f). While almost no tin is incorporated in the bulk of the thin film, a clear enrichment of tin was observed towards the surface of the sample. We propose a liquid tin layer floating on top of the thin film during growth that enables the stabilization of the κ-phase in a vapor-liquid-solid process (surfactant-mediated epitaxy [10]). We could further confirm the transparency of our thin films up to the optical bandgap of the material of $\approx$ 4.9 eV.

In summary, our κ-Ga_2O_3 layers are structurally and morphologically superior to thin films in the β-phase and represent an excellent basis for further research on the respective alloy systems and corresponding heterostructures for device applications. A detailed investigation by us on the PLD growth of binary κ-Ga_2O_3 can be found in Ref. 5.

2.4.2 Structural and optical investigations of κ-$(In_xGa_{1-x})_2O_3$ thin films

A. Hassa, M. Kneiß, D. Splith, C. Sturm, H. von Wenckstern, and M. Grundmann

A two inch in diameter thin film of κ-$(In_xGa_{1-x})_2O_3$ was prepared by PLD with CCS approach [6]. As ablation target we used two segments consisting of tin-doped gallium and indium oxides, respectively. The chemical cation composition in the film, depicted in Fig. 2.9(a), shows an In-content ranging between 1 at.% and 83.5 at.%. The cation distribution exhibits a non-linear behavior as visible in Fig. 2.9(b). For a z-position below 15 mm, the linescan shows a slight and for $z > 15$ mm a rapid increase of x being connected to phase separation. To identify the different crystallographic phases, XRD measurements were performed. The results of 55 2θ-ω measurements acquired along the gradient are depicted in Fig. 2.9(c) and reveal three different phases, which can be assigned to the orthorhombic κ-Ga_2O_3 modification for $x \leq 0.35$, to hexagonal $InGaO_3$ (II) for $0.35 < x < 0.5$, and to the cubic bixbyite structure for $x \geq 0.5$. In the following we only will discuss the region with an In-content below 35 at.% assigned to the orthorhombic phase. The reflexes of the (001) orientation of κ-Ga_2O_3 and the reflexes of the (-201) orientation of β-Ga_2O_3 lie close to each other, but that of the κ-phase appear at slightly higher angles. In order to confirm that the thin film is indeed in the κ-phase, ϕ-scans were performed. Fig. 2.9(d) exhibits XRD ϕ-scans of skew-symmetric reflections corresponding to the (131), (122) and (206) lattice planes

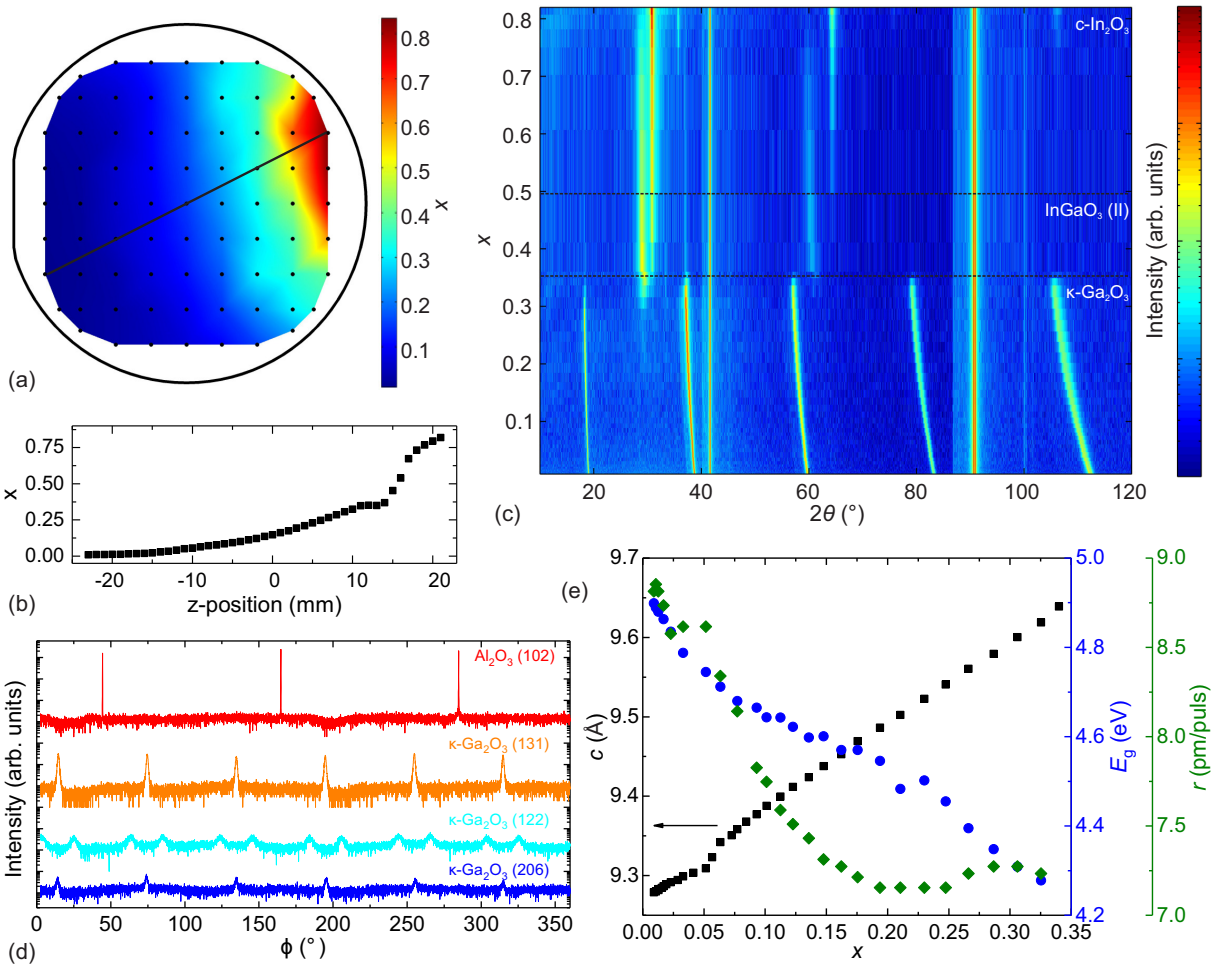

Figure 2.9: (a) False color representation of the In-content x of a $(In_xGa_{1-x})_2O_3$ thin film grown on a 2 inch in diameter c-plane sapphire substrate, (b) shows an EDX-linescan along the compositional gradient as indicated by the black line in (a). (c) False color plot of 55 XRD 2θ-ω measurements acquired along the gradient direction. (d) XRD ϕ-scans of a sample piece at $x \sim 0.01$. (e) The c-lattice constant determined from XRD patterns as well as the band gap E_g and growth rate r obtained from spectroscopic ellipsometry measurements as a function of the In-content x.

of the κ-phase. For the (131) and the (206) planes, six-fold reflections were observed with separations of 60°, which indicates epitaxial growth on the c-sapphire substrate. For the (122) lattice plane, twelve reflections occur corroborating the orthorhombic symmetry, because only in this structure twelve peaks are expected due to mirror planes. Fig. 2.9(e) shows the dependence of the c-lattice constant as well as the bandgap energy E_g and the growth rate r on the In-content. The c-lattice constant increases nearly linear with increasing x and can be described by $c = [\,(9.269 \pm 0.004) + (1.097 \pm 0.01) \cdot x\,]$ Å. Spectroscopic ellipsometry measurements were utilized to estimate E_g and the sample thickness d to calculate r (= d/ pulses), subsequently. The bandgap energy decreases with increasing x from 4.9 eV down to 4.3 eV for $0 \leq x \leq 0.35$. The growth rate shows different behavior for different x regimes. It starts for $x = 0.01$ at $\tau = 8.7$ pm/pulse and saturates around 7.2 pm/pulse for $x \geq 0.2$. Further informations can be found in more detail in Ref. 11.

[1] Higashiwaki *et al.*, Applied Physics Letters **100**, 013504 (2012)
[2] von Wenckstern, Adv. Electron. Mater **3**, 1600350 (2017)
[3] Roy *et al.*, Journal of the American Chemical Society **74**, 719–722 (1952)
[4] Maccioni *et al.*, Appl. Phys. Express **9**, 04102 (2016)
[5] Kneiß *et al.*, APL Materials **7**, 022516 (2019)
[6] von Wenckstern *et al.*, CrystEngComm **15**, 10020 (2013)
[7] Kracht *et al.*, Phys. Rev. Appl. **8**, 054002 (2017)
[8] Orita *et al.*, Thin Solid Films **411**, 134 (2002)
[9] Cora *et al.*, CrystEngComm **19**, 1509 (2017)
[10] Iwanari and Takayanagi, Jpn. J. Appl. Phys., Part 2 **30**, L1978 (1991)
[11] Hassa *et al.*, APL Materials **7**, 022525 (2019)

This work was supported by European Social Fund within the Young Investigator Group "Oxide Heterostructures" (SAB 100310460).

2.5 Investigation of cation vacancy concentrations in $(In_xGa_{1-x})_2O_3$ thin films by positron annihilation spectroscopy

V. Prozheeva,* H. von Wenckstern,† F. Toumisto,* M. Grundmann†

*Aalto University, Department of Applied Physics, Espoo, Finland
†Universität Leipzig, Felix-Bloch-Institut für Festkörperphysik

Various nominally undoped $(In_xGa_{1-x})_2O_3$ thin films with lateral variation of the alloy composition were grown on (00.1)Al_2O_3 and (100)MgO substrates by a continuous composition spread approach for pulsed-laser deposition [1]. Positron annihilation spectroscopy (PAS) in Doppler broadening mode was used to investigate the formation of cation vacancies as a function of the alloy composition [2]. Since In_2O_3 and Ga_2O_3 have different equilibrium crystal structure (cubic bixbyite for In_2O_3 and monoclinic beta-gallia structure for Ga_2O_3), the influence of alloying was studied for the cubic and the monoclinic modification.

In nominally undoped monoclinic samples ($x \leq 0,02$) on (00.1)Al_2O_3 the cation vacancy (V_M) concentration increases with increasing indium content as indicated by the increase of the S parameter depicted in fig. 2.10a). For binary Ga_2O_3 the density of V_M is estimated to $(2-4) \times 10^{16}\,cm^{-3}$. Binary Ga_2O_3 thin films grown by metal-organic vapor phase epitaxy have significantly larger gallium vacancy concentrations with values above $10^{17}\,cm^{-3}$ [3]. (S, W)-plots (not shown) reveal that the nature of these cation vacancies in our ternary layers corresponds to V_M in the monoclinic beta-gallia structure. For an indium content between 0.2 and 0.8 the cubic and the hexagonal $InGaO_3$ II modifications are observed besides the monoclinic phase. Here the type of the predominant cation vacancy changes to V_M in the cubic bixbyite lattice modification. For cubic $(In_xGa_{1-x})_2O_3$ on (00.1)Al_2O_3 the same type of cation vacancy is dominant even for Ga-rich samples, for which the composition dependence of the S-parameter is depicted in fig. 2.10b). The above findings and the larger value of the S-parameter in fig. 2.10b) demonstrate that the cation vacancy concentration in cubic $(In_xGa_{1-x})_2O_3$ PLD layers is higher than in monoclinic $(In_xGa_{1-x})_2O_3$ PLD thin films.

Monoclinic $(In_xGa_{1-x})_2O_3$ on (100)MgO substrate have significantly lower cation vacancy concentration than layers on (00.1)Al_2O_3. The vacancy concentration increases with increasing indium content. For $0.3 < x < 0.65$ samples on (100)MgO are X-ray amorphous, however, positron trapping at cation vacancies occurs and from (S, W)-plots (not shown) these vacancies correspond to V_{In} in cubic In_2O_3. The concentration of V_{In} is highest for $x = 0.5$ and decreases in a similar way for higher and lower In content. For $x > 0.65$ thin films have bixbyite crystal structure. Here, the cation vacancy concentration is above 10^{17} cm^{-3} and increases expectedly with increasing Ga admixture. Overall, the cation vacancy concentration in cubic $(In_xGa_{1-x})_2O_3$ is significantly lower than the free carrier density and hence it is not a relevant compensation center.

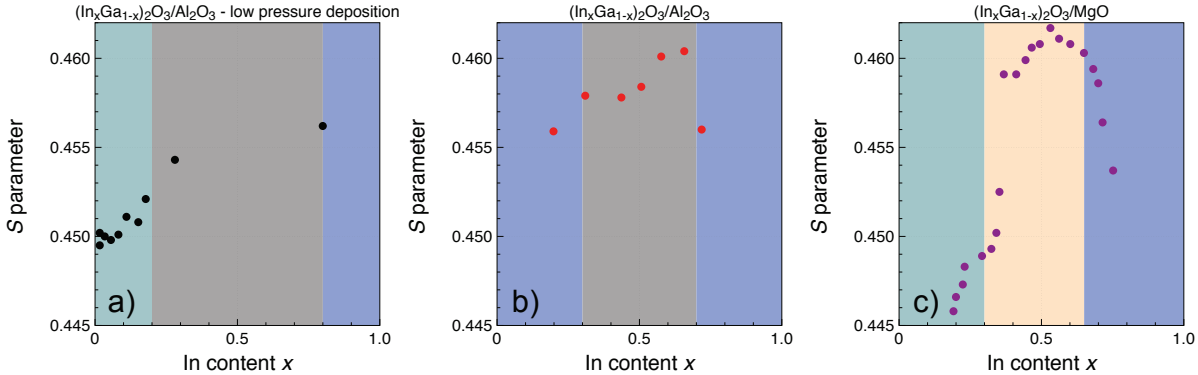

Figure 2.10: Dependence of he S-parameter on the indium content for $(In_xGa_{1-x})_2O_3$ thin films on a,b) (00.1)Al_2O_3 and c) (100) MgO substrate. Samples were grown at an oxygen partial pressure of a) 3×10^{-4} mbar and b,c) 8×10^{-2} mbar. The background color highlights samples with monoclinic (greenish), cubic (blueish), mixed (gray) or amorphous (orange) phase.

[1] H. von Wenckstern, Z. Zhang, F. Schmidt, J. Lenzner, H. Hochmuth, and M. Grundmann, CrystEngComm **15**, 10020 (2013).
[2] V. Prozheeva, R. Hölldobler, H. von Wenckstern, M. Grundmann, and F. Tuomisto, J. Appl. Phys. **123**, 125705 (2018).
[3] E. Korhonen, F. Tuomisto, D. Gogova, G. Wagner, M. Baldini, Z. Galazka, R. Schewski, and M. Albrecht, Appl. Phys. Lett. **106**, 242103 (2015).

2.6 Influence of oxygen deficiency on the rectifying behavior of transparent-semiconducting-oxide-metal interfaces

P. Schlupp,* S. Vogt,* T. Schultz,† H. vonWenckstern,* N. Koch,† M. Grundmann*

*Universität Leipzig, Felix-Bloch-Institut für Festkörperphysik
†Humboldt Universität zu Berlin, Institut für Physik

Conductive oxide materials were used for a long time mainly as transparent electrodes (e.g. In_2O_3 : Sn, ZnO:Ga) [1]. In recent years, also their semiconducting properties

came into focus. ZnO, SnO_2, Ga_2O_3 and In_2O_3 as well as amorphous oxide materials like In-Ga-Zn-O or Zn-Sn-O are of interest because of various desired properties like transparency, high electron mobility or high breakdown fields [2–5]. For investigation as well as for applications development of technology allowing reproducible fabrication of highly rectifying diodes is crucial. Since oxide materials are mainly unipolar, rectifying contacts are realized by Schottky barrier diodes.

It is known, that the amount of oxygen in the material has a strong influence on the electrical and optical properties. Especially oxygen deficiency plays an important role on surface band bending and surface accumulation of electrons [6, 7]. The formation of oxygen vacancies near the surface strongly influences the performance of Schottky barrier diodes [8, 9].

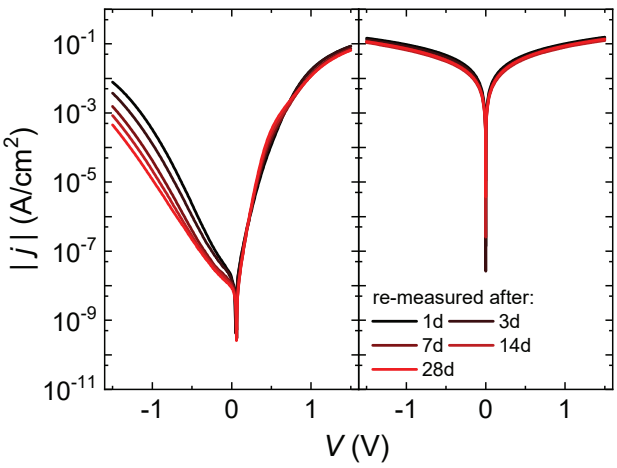

Figure 2.11: IV-characteristics of the ZTO/PtO_δ/Pt (left) and the ZTO/Pt (right) Schottky barrier diodes measured after times of fabrication as indicated.

To investigate the influence of oxygen on the formation and the stability of Schottky barrier diodes, current-voltage (IV) measurements and X-ray photoelectron spectroscopy (XPS) were applied to Pt-Schottky contacts on amorphous zinc tin oxide (ZTO) [10]. The ZTO thin films were fabricated by pulsed laser deposition and have an electron density of about 3×10^{17} cm^{-3} which was confirmed by Hall-effect measurement. Two types of Pt-contact were deposited as Schottky contacts: (i) sputtering in argon resulted in metallic Pt contacts and (ii) sputtering in oxygen capped by a Pt layer sputtered in argon resulted in PtO_δ contacts.

The IV-characteristics of the ZTO/PtO_δ/Pt (left) and the ZTO/Pt contacts (right) are depicted in figure 2.11. The ZTO/Pt contact does not show a rectifying behavior at all. Its IV-characteristics does not change within 28 days after the deposition of the contacts. In contrast, the ZTO/PtO_δ/Pt contact exhibits current rectification of about one order of magnitude at day 1, which increases to about two orders of magnitude at day 28. This change is mainly due to a decrease of the reverse current, the thin film resistance does not change. Therefore, we conclude that an interface effect is responsible for the change and oxygen may play a crucial role.

A piece of both samples, the ZTO/Pt as well as the ZTO/PtO_δ/Pt, was investigated by depth-resolved XPS. The contact material was removed stepwise by sputtering using argon with an acceleration voltage of 300 V. The elemental concentration of both

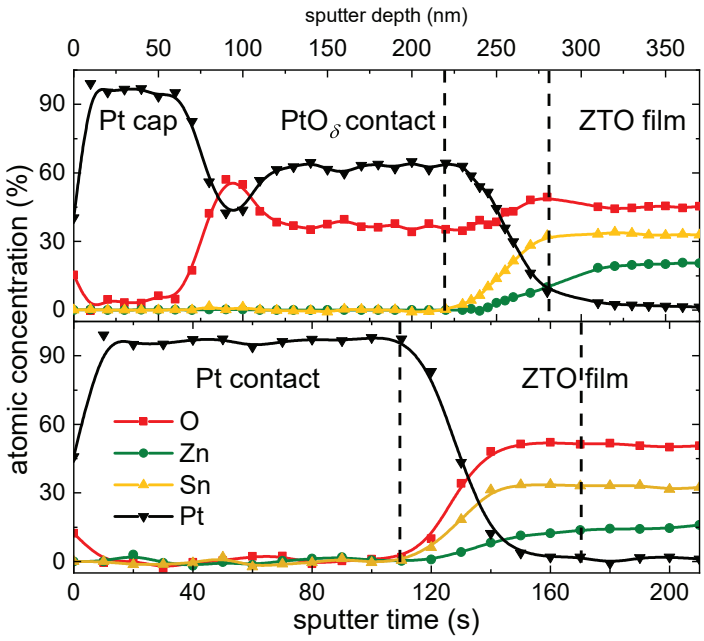

Figure 2.12: Elemental concentration in dependence of the depth of the ZTO/PtO$_\delta$/Pt (top) and the ZTO/Pt contacts (bottom).

samples is depicted in figure 2.12 starting at the Pt surface (low sputter times). The PtO$_\delta$ layer contains a large amount of oxygen. At the interface (reached after 275 s), the oxygen content increases. From the XPS signal it can be seen (not shown) that this increased oxygen amount is bound to the Sn atoms. At the interface of the ZTO/Pt contact a signal that can be assigned to PtO as well as an additional peak of the Sn in the vicinity of an oxygen vacancy was observed. Therefore we conclude, that in the ZTO/PtO$_\delta$/Pt contact oxygen ions move from the oxygen reservoir within the PtO$_\delta$ layer into ZTO and saturate undercoordinated cations in the vicinity of the interface. The high electron density of the ZTO in the vicinity of the interface is lowered resulting in higher rectification of the Schottky barrier diode.

Using the Pt 4f peak, the Pt(OH)$_4$ and the PtO content were resolved for the ZTO/PtO$_\delta$/Pt. The intensity at day 1 and day 30 after fabrication of the contacts in dependence of the sputter depth is depicted in figure 2.13. The Pt(OH)$_4$ content in the sample did not change significantly in this time scale, however, a reduction towards the interface is visible. In contrast, the PtO content seems to decrease over time. Its content is reduced by about 50 %. From these results we conclude that the Pt(OH)$_4$ at the interface is completely reduced within the first 24 h resulting in improved diode characteristics compared to the metallic Pt contacts. The reduction of the PtO is much slower and the oxygen movement improves the diodes further over time decreasing the electron density at the interface-near ZTO. This leads to improved IV-characteristics which can be seen in figure 2.11.

The aging of the Schottky barrier diodes may be accelerated by the application of an external bias to the devices. This accelerates the movement of the oxygen ions into the ZTO. To prove this, a voltage of −1.5 V was repeatedly applied for 500 s to the diodes. A decrease of the reverse current is observed for the ZTO/PtO$_\delta$/Pt diode with increasing application time, whereas the ZTO/Pt diode remains unchanged. This

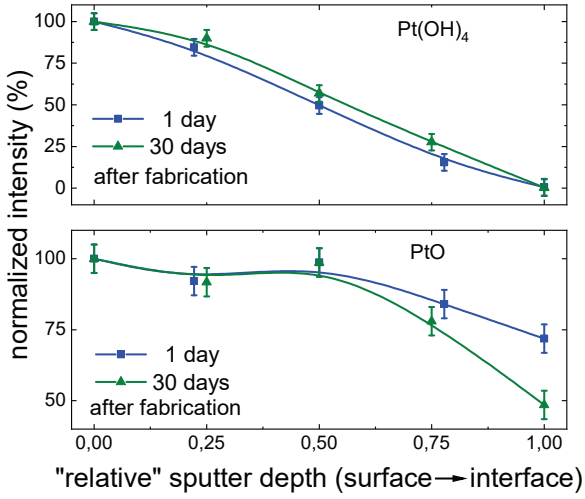

Figure 2.13: Change of the $Pt(OH)_4$ (top) and PtO (bottom) component of the Pt $4f$ peak for a ZTO/PtO_δ/Pt Schottky contact.

mechanism is believed to be present also at other oxide-semiconductor-metal interfaces and our results provide a general methodology for achieving highly rectifying Schottky barrier diodes to these materials.

[1] K.L. Chopra, S. Major, D.K. Pandya: Thin Solid Films. **102**, 1-46 (1983)
[2] M. Grundmann, H. Frenzel, A. Lajn, M. Lorenz, F.-L. Schein, H. von Wenckstern: Physica Status Solidi A **207**, 1437-1449 (2010)
[3] H. von Wenckstern: Advanced Electronic Materials **3**, 1600350 (2017)
[4] T. Kamiya, K. Nomura, H. Hosono: Science and Technology of Advanced Materials **11**, 044305 (2010)
[5] H.Q. Chiang, J.F. Wagner, R.L. Hoffman, J. Jeong, D.A. Keszler: Applied Physics Letters **86**, 013503 (2005)
[6] T. Berthold, J. Rombach, T. Stauden, V. Polyakov, V. Cimalla, S. Krischok, O. Bierwagen, M. Himmerlich: Journal of Applied Physics **120**, 245301 (2016)
[7] B.J. Coppa, R.F. Davis, R.J. Nemanich: Applied Physics Letters **82**, 400 (2003)
[8] M.W. Allen, S.M. Durban: Applied Physics Letters **92**, 122110 (2008)
[9] S. Müller, H. von Wenckstern, F. Schmidt, D. Splith, R. Heinold, M. Allen, M. Grundmann: Journal of Applied Physics **116**, 194506 (2014)
[10] T. Schultz, S. Vogt, P. Schlupp, H. von Wenckstern, N. Koch, M. Grundmann: Physical Review Applied **9**, 064001 (2018)

2.7 MESFETs and inverters based on amorphous zinc-tin-oxide thin films prepared at room temperature

S. Vogt, H. von Wenckstern, M. Grundmann

Amorphous oxide semiconductors (AOSs) have great potential for future electronic applications due to low fabrication costs and their superior performance compared

to amorphous Si [1]. A non-toxic and abundantly available compound belonging to the group of AOSs is zinc-tin-oxide (ZTO). The influence of the deposition method and conditions as well as the influence of the cation composition on the electrical properties of ZTO have been investigated [2–4]. Highly rectifying diodes based on amorphous ZTO have been reported for different gate contact materials such as metal oxides and *p*-type oxide semiconductors [6–10]. The first ZTO based metal-insulator field-effect transistor (MISFET) was presented by Chiang *et al.* in 2005 [11]. In 2016 the first metal-semiconductor field-effect transistor (MESFET) using silver oxide as gate material and amorphous ZTO as *n*-type channel was reported by Dang *et al.* [12]. However, the deposition process required elevated temperatures and an additional thermal annealing at 525°C to improve the device performance.

In this work we present amorphous ZTO based MESFETs fabricated at room temperature. The *n*-type ZTO channels were deposited by long throw magnetron sputtering [4]. It was previously found that an increase of the free carrier density towards the substrate inhibited the depletion of the ZTO channel for our ZTO layers. It was speculated that oxygen vacancies at the interface to the substrate may be the cause of the increasing free carrier density [13]. To prevent this effect, a novel sputtering process was implemented. The sputtering process was started in a gas mixture of 25 sccm oxygen and 30 sccm argon and subsequently, the oxygen content was continuously reduced to 0 sccm in 720 s. On top of this oxygen variation layer, a conductive channel was sputtered for a predefined time span under 30 sccm argon.

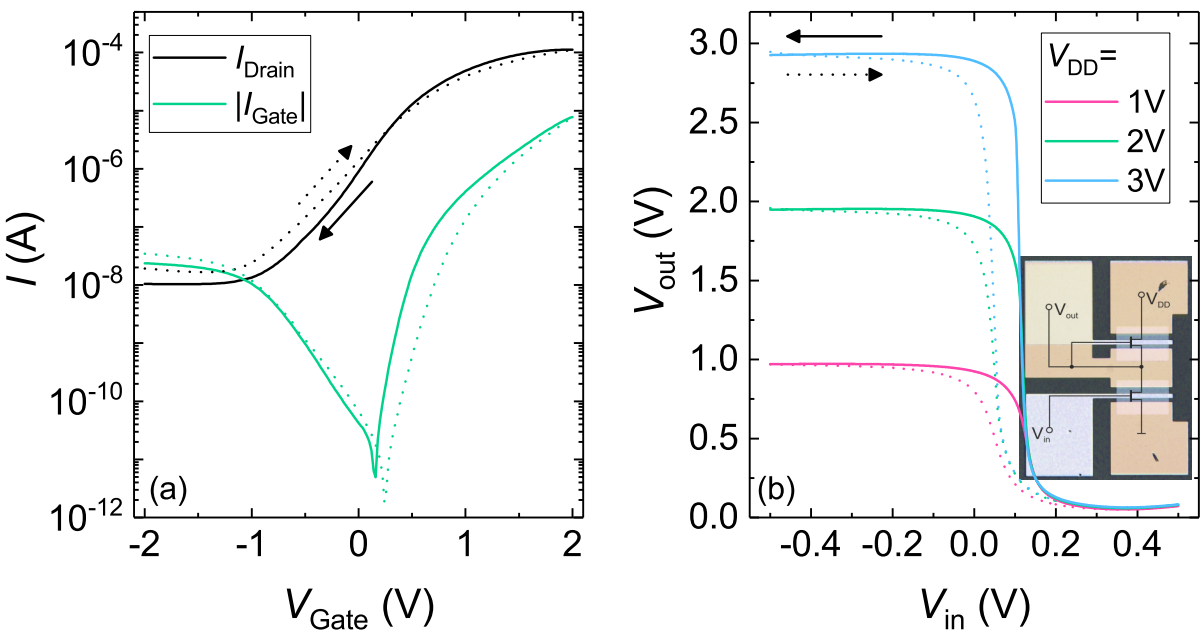

Figure 2.14: Transfer characteristics (a) of a MESFET based on amorphous zinc-tin-oxide and using platinum oxide as gate material and the voltage transfer characteristics (b) for an inverter based on such a MESFET.

The gate contacts of the MESFETs and the inverter were formed by reactively sputtered platinum covered by a metallic platinum layer [5]. The ohmic contacts were realized by sputtered gold. Three different ZTO layer thicknesses between 19 and 24 nm

were investigated. A higher thin film thickness led to an increase of the free carrier density from 6×10^{17} to 2×10^{18} cm^{-}3 (always normalized to the entire ZTO layer thickness). In Figure 2.14 (a) the transfer characteristic for a MESFET with a ZTO layer thickness of 24 nm is depicted. A current on-to-off ratio of 1.1×10^4 with a threshold voltage of $V_T \approx 0$ V and a sub-threshold swing of 370 mV dec^{-1} were measured for this device. A maximum current on-to-off ratio of 1.8×10^6 was achieved for a ZTO layer thickness of 19 nm ($V_T \approx 0.5$ V). Thus a smaller ZTO layer thickness results in normally off devices. An improvement of the devices was observed for the application of a negative bias at the gate contact. It led to a reduction of the reverse gate leakage current and an increasing steepness of the transfer characteristics.

To demonstrate a logic device based on these thin films, a 24 nm thick ZTO layer was used to fabricate inverters. The used layout and the resulting voltage transfer characteristic are shown in Figure 2.14 (b). The characteristics exhibit a hysteresis between forward and reverse voltage sweep direction, which is most likely due to a small change in the threshold voltage for these two sweep directions. An uncertainty level below 0.25 V and a peak gain magnitude as high as 110 for an operating voltage of $V_{DD} = 3$ V were obtained, which exceed previous reports on ZTO based inverters [14].

[1] H. Hosono *et al.*: J. Non-Cryst. Solids. **198-200**, 165 (1996)
[2] M. K. Jayaraj *et al.*: J. Vac. Sci. Technol. B **26**, 495 (2008)
[3] S. Bitter *et al.*: ACS Comb. Sci. **18**, 4, 188-194 (2016)
[4] H. Frenzel *et al.*: Physica Status Solidi (a) **212**, 7, 1482-1486 (2015)
[5] A. Lajn *et al.*: J. Vac. Sci. Technol. B **27**, 3, 1769 (2009)
[6] Y. Son *et al.*: ACS Appl. Mater. Interfaces **8**. 36, 23801-23809 (2016)
[7] S. Bitter *et al.*: ACS Appl. Mater. Interfaces **9**, 31, 26574-26581 (2017)
[8] P. Schlupp *et al.*: Adv. Electron. Mater. **1**, 1400023 (2015)
[9] P. Schlupp *et al.*: Physica Status Solidi (a) **214**, 10, 1700210 (2017)
[10] M. Grundmann *et al.*: J. Phys. D: Appl. Phys. **49**, 21, 213001 (2016)
[11] H. Chiang *et al.*: Appl. Phys. Letters **86**, 1, 013503 (2005)
[12] G. Dang *et al.*: Appl. Phys. Express **9**, 041101 (2016)
[13] T. Schultz *et al.*: Phys. Rev. Appl. **9**, 6, 064001 (2018)
[14] S. Tsai *et al.*: ECS J. Solid State Sci. Technol. **4**, 5, P176-P180 (2015)

2.8 Full-swing, high-gain inverters based on ZnSnO JFETs and MESFETs

O. Lahr, Z. Zhang, F. Grotjahn, P. Schlupp, S. Vogt, H. von Wenckstern, A. Thiede, M. Grundmann

Amorphous semiconducting oxides (AOS), consisting of heavy metal cations, exhibit remarkable transport properties despite their disordered structure [1]. The possibility of low-temperature deposition associated with their high transparency in the visible range enable the cost-efficient fabrication of transparent and even bendable circuits. One promising candidate for sustainable novel technology is the AOS zinc-tin-oxide (ZTO) for which first room-temperature (RT) fabricated metal-semiconductor field-effect transistors (MESFETs) and inverter structures have recently been reported by

us [2].
Here, we present MESFETs and junction field-effect transistors (JFETs) as well as inverters using amorphous *n*-ZTO as channel material. The channels were deposited at RT by long-throw magnetron sputtering using a target with a 67 wt.% SnO_2 and 33 wt.% ZnO composition [3]. In case of MESFETs, reactively sputtered PtO_x with a Pt capping layer was used as gate material to reduce the free-carrier density close to the ZTO/PtO_x interface due to a saturation of under-coordinated cation bonds [4]. Additionally, a thin semi-insulating ZTO layer was primarily sputtered below the gate to further decrease the leakage current through the gate diode [5]. For JFET-based devices a NiO gate contact was deposited on top of i-ZTO by pulsed laser deposition at RT and capped with a thin Au layer.
RT transfer characteristics of the best MESFET and JFET are depicted in Fig. 2.15 (a). Both devices exhibit a clear field-effect with on/off current ratios of about 8 orders of magnitude. The sub-threshold swing and maximum transconductance of the MESFET (JFET) are 242 (229) mV/dec and 236 (148) μS, respectively. Additionally, repeated measurements after a period of 200 days prove the long-term stability of the characterized devices concerning their electrical properties and performance. We investigated the cascading of MESFET- and JFET-based inverters using a FET logic (SDFL) implementing PtO_x/ZTO Schottky barrier diodes and NiO/ZTO pn-heterodiodes for level shifting, as depicted in Fig. 2.15. The corresponding voltage transfer characteristics of a MESFET-(JFET)-based inverter, as depicted in Fig. 2.16 (a), exhibit a maximum gain of 294 (347) and an uncertainty level as low as 0.27 (0.26) V (level shift not considered) at an operating voltage of $V_{DD} = 5$ V. In Fig. 2.16 (b) and (c) we depict the peak gain magnitude *pgm* and the uncertainty level V_{UC} for various operating voltages of inverters without level shifting diodes and for inverters with one or two level shifting diodes connected to the input. The uncertainty level is higher for inverters with level shift, however, a value of 380 mV is not exceeded for V_{DD} up to 5 V.

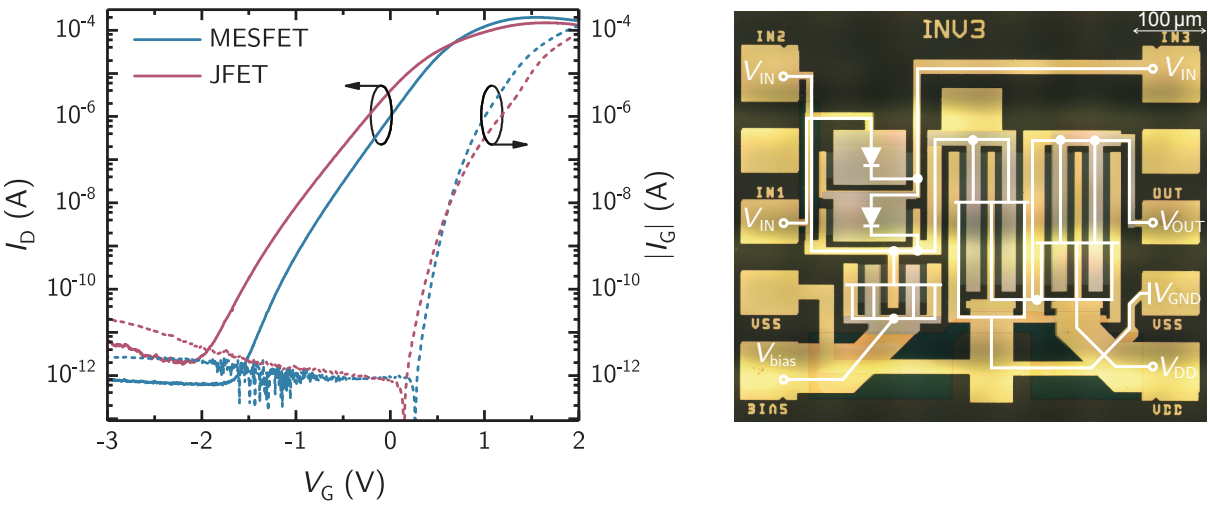

(a) **(b)**

Figure 2.15: (a) RT transfer characteristic of the best MESFET and JFET with corresponding source-gate characteristics for $V_D = 2$ V. (b) Microscopic image with overlayed circuit schematic of a SDFL inverter.

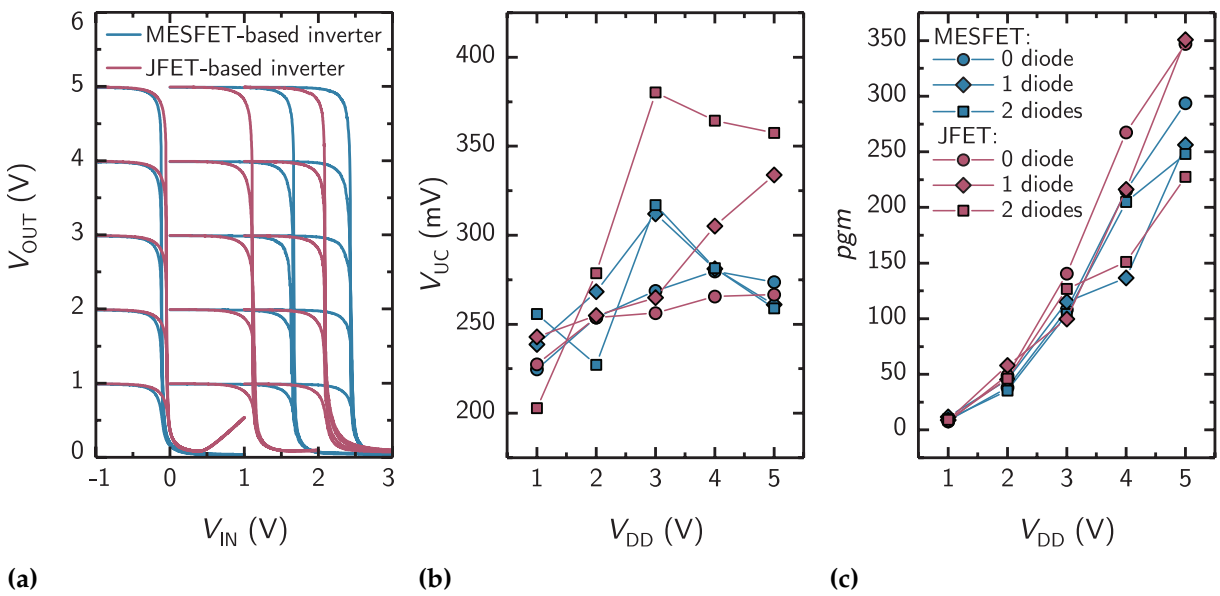

Figure 2.16: (a) Voltage transfer characteristics of ZTO-based SDFL inverters and dependence of (b) *pgm* and (c) V_{UC} on V_{DD} for no, one or two level shifting diodes.

Amorphous ZTO-based inverter circuits reported here, comprising MESFETs and JFETs, were entirely fabricated at the lowest processing temperature and exhibit by far the highest gain despite operating at lowest supply voltages, compared to literature results on ZTO-based devices. In order to cascade such inverters, level shifting is necessary and was realized here by employing the SDFL approach. Our inverters exhibited stable *pgm* and V_{UC} values under operation with level shift making both FET types highly suited for realization of ring oscillators [6].

[1] H. Hosono, Journal of Non-Crystalline Solids 351 (2006).
[2] S. Vogt *et al.*, Applied Physics Letters 113 (2018).
[3] H. Frenzel *et al.* Physica Status Solidi 212 (2015).
[4] T. Schultz *et al.*, Physical Review Applied 9 (2018).
[5] P. Schlupp *et al.*, Advanced Electronic Materials 1 (2015).
[6] F. Klüpfel *et al.*, Advanced Electronic Materials 2 (2016).

2.9 Properties of $In_2S_3/ZnCo_2O_4$ pin-heterostructures

T. Jawinski,* H. von Wenckstern,* L.A. Wägele,† R. Scheer,† M. Grundmann*

*Universität Leipzig, Felix-Bloch-Institut für Festkörperphysik
†Martin-Luther-Universität Halle-Wittenberg

Indium thiospinel semiconductors may potentially be used in intermediate band (IB) solar cells [1]. For that, transition metal ions have to substitute indium at octahedral lattice positions. For a sufficient transition metal concentration a delocalized defect band

will form enabling transition from the valance band to the IB and from the IB to the conduction band leading to a substantial increase of the maximum efficiency of IB solar cells compared to conventional single junction solar cells [1]. So far, epitaxial growth of p-type In_2S_3 thin films was not reported. Hence, realization of pn-heterostructures has to be investigated for potential exploitation of In_2S_3 in IB solar cells. We have fabricated highly rectifying vertical heterostructures on undoped and vanadium-doped In_2S_3 [2]. All In_2S_3 layers were deposited by molecular beam epitaxy on AZO-layers. On top, thin films of $ZnCo_2O_4$ (ZCO) were grown by pulsed-laser deposition. The electrical properties of the heterostructures were investigated by current-voltage measurements for temperatures between 100 and 300K. The reverse current of the diodes has an activation energy of about 1.6 eV for the undoped and 1.3 eV for the V-doped sample, respectively, and indicate defect assisted recombination as reverse current transport process.

Room temperature current-density–voltage characteristics of AZO/ZCO/In_2S_3:V pn-diodes are depicted in figure 2.17 for various vanadium doping concentration. A current rectification of more than six orders of magnitude is achieved for diodes comprising nominally undoped In_2S_3 layers. The incorporation of vanadium leads to a slightly reduced (increased) forward (reverse) current and with that lower current rectification, however, the electrical properties of these diodes are sufficient for photo-voltaic activity. For both type of diodes an open-circuit voltage and a short-circuit current of 300 mV and 0.29 mA/cm^2 were determined upon illumination with an AM1.5 spectra (100 mW/cm^2).

[1] P. Palacios, I. Aguilera, K. Sánchez, J. C. Conesa, and P. Wahnón, Phys. Rev. Lett. **101**, 046403 (2008).
[2] T. Jawinski, L. A. Wägele, R. Scheer, M. Grundmann, and H. von Wenckstern, physica status solidi (a), **215**, 1700827 (2018).

2.10 Negative-U properties of the deep level E3 in ZnO

R. Pickenhain,* H. von Wenckstern,* M. Schmidt,† A. Pöppl,* G. Benndorf,* R. Böttcher,* M. Grundmann*

*Universität Leipzig, Felix-Bloch-Institut für Festkörperphysik
†Helmholtz-Zentrum für Umweltforschung, Leipzig

A common electronic defect in the wide bandgap semiconductor zinc oxide (ZnO) is the so-called E3 defect having one transition level about 300 meV below the conduction band minimum. E3 has been found in material of various source including bulk single crystals and heteroepitaxial thin films [1]. Despite numerous experimental and theoretical studies, the microscopic origin of the E3 defect is not resolved, conclusively. We comprehensively investigated properties of the E3 defect by temperature-dependent capacitance measurements, deep-level transient spectroscopy (DLTS), electron paramagnetic resonance, temperature-dependent photo luminescence (PL) measurements and optical DLTS (ODLTS).

The capacitance, DLTS and ODLTS measurements reveal that E3 can capture up to two electrons; the capture of the first occurs very quickly, an energetic barrier of

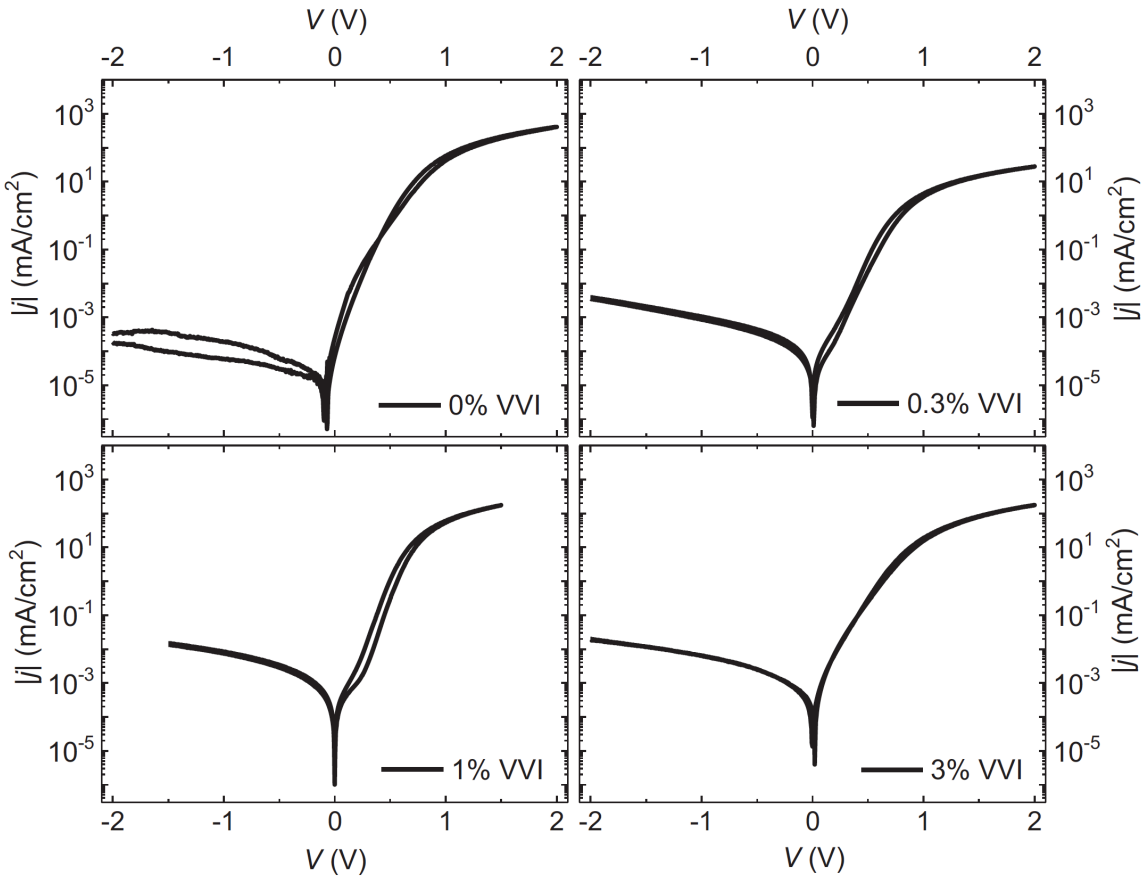

Figure 2.17: Room temperature current-density–voltage characteristics of representative AZO/In_2S_3:V/ZCO-diodes with varying V/(V+In)-ratios. The oxygen partial pressure during deposition was 0.03 mbar.

about 100 meV exists for the capture of the second electron. The capture of the second electron leads to strong lattice relaxation. In a thermal emission process these two electrons are emitted simultaneously, implying that the E3 defect is a negative-U center. We determined the photoionization cross-sections for the three possible transitions $\epsilon(+2/+1)$, $\epsilon(+1/0)$ and $\epsilon(+2/0)$. If thermal emission is suppressed optical excitation with energy between 550 meV and 1 eV will induce the optical emission of both electrons into the conduction band. Photon energies above 1 eV will excite a single electron into the conduction band and reconfigure the level into the meta-stable singly occupied state that would correspond to V_O^+. Further, we have demonstrated, that E3 is involved in a radiative recombination that can be excited with sub-bandgap energy photons and that has its maximum intensity at about 2.1 eV. By temperature dependent measurements we demonstrated, that this transition can only be excited for temperatures at which the E3 defect is not occupied by electrons. If this is the case, we only observed the commonly reported defect band emission. Next, the samples were investigated by electron paramagnetic resonance (EPR) measurements as a function of temperature and optical excitation energy. We found that numerous properties of the E3 defect, determined by DLTS, ODLTS and PL, and the oxygen vacancy, investigated by the EPR experiments, are similar. These include temperature range in which E3 $\epsilon(+2/+1)$ transition level or V_O^+ is observable, temperature dependence of E3-related emission

band and EPR V_O^+ intensity, excitation energy dependence of photo cross-section of the E3 $\epsilon(+2/+1)$ transition and EPR V_O^+ line amplitude being depicted in fig. 2.18. These similarities suggest that the nature of the E3 defect is the oxygen vacancy.

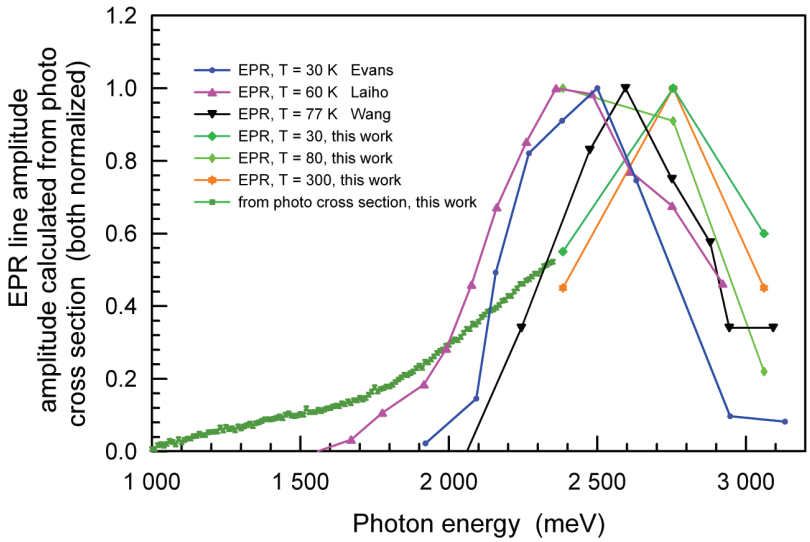

Figure 2.18: Collection of available literature data on the the dependence of the V_O^+ EPR signal strength on incident photon energy, our own EPR results and the photo ionization cross-section of the E3 $\epsilon(+2/+1)$ transition level calculated from ODLTS data.

[1] R. Pickenhain, M. Schmidt, H. von Wenckstern, G. Benndorf, A. Pöppl, R. Böttcher, and M. Grundmann, phys. stat. sol. (b), **255**, 1700670 (2018).

2.11 Magnetoelectric coupling in $BaTiO_3$-$BiFeO_3$ multilayers – an interface effect?

S. Hohenberger, J. Jochum*, K. Temst*, M. Grundmann, M. Lorenz

*Institute for Nuclear and Radiation Physics, KU Leuven, Belgium

Composite multiferroic heterostrctures, consisting of ferroelectric and (anti-) ferromagnetic materials, promise to play a central role in the utilization of the magnetoelectric (ME) effect in e.g. data storage and magnetic sensing applications [1]. A particularly successful approach has been the combination of the only known single-phase ME multiferroic $BiFeO_3$ (BFO) [2] with the archetypal ferroelectric $BaTiO_3$ (BTO) in epitaxial multilayer thin films [3–6]. Up to a tenfold increase of the ME coupling coefficient α_{ME}

relative to the single layer value for BFO of 6 $Vcm^{-1}Oe^{-1}$ [2] was reported.
Our previous work [3] suggests a significant influence of the thickness of either the BFO layer, or the double layer thickness d_{dl} of BTO and BFO together, on the magnitude of ME coupling in these multilayers. This calls into question the results reported in [4] and [5], which compared samples deposited at various oxygen pressures and concluded a dependency on p_{O_2}. A closer look at the investigated samples reveals that the laser pulse numbers for the films deposited at varied p_{O_2} were kept constant, leading to different double layer thicknesses, as the deposition rates strongly depend on the background gas pressure. For example the 0.01 mbar and 0.25 mbar samples in [5] have respective double layer thicknesses of 38.6 nm and 13.8 nm, with α_{ME} values of 13.4 $Vcm^{-1}Oe^{-1}$ and 49.7 $Vcm^{-1}Oe^{-1}$. A TEM investigation revealed a higher level of microstrain in the low-α_{ME} sample, which was attributed to increased oxygen deficiency due to lower p_{O_2}.
In an effort to re-evaluate and distinguish the influences of oxygen partial pressure, double-layer thickness, and BTO-to-BFO thickness ratio, three sample series were grown by pulsed laser deposition on Nb-doped $SrTiO_3$ under closely controlled deposition conditions. The first series of multilayer samples was created with p_{O_2} ranging from 0.01 mbar to 0.25 mbar and tightly controlled d_{dl} of 20.0 ± 0.2 nm. For the second series, a constant 1:1 BTO:BFO ratio was maintained while varying d_{dl} from 4.6 ± 0.2 nm to 20.1 ± 1.0 nm. For the last series, d_{BTO} and d_BFO were varied from 2 nm to 18 nm, while keeping a constant d_{dl} of 19.7 ± 0.3 nm. The substrate temperature was maintained at 680 °C and p_{O_2} was 0.25 mbar for the ratio- and d_{dl}-series.
Fig. 2.19 a)-c) shows the measurement values of α_{ME} at 300 K in 0 T H_{DC} obtained via the dynamical method in 10 Oe H_{AC} for the respective sample series, as measured at the KU Leuven in Belgium. In [4] a monotonic decline of α_{ME} with decreasing p_{O_2} was apparent. However, the measurements presented in Fig. 2.19 a) show an initial decline of α_{ME} from 0.25 mbar to 0.1 mbar, which is reverted toward lower p_{O_2}. The value of α_{ME} for 0.01 mbar is even slightly larger than for 0.25 mbar, reaching 110 $Vcm^{-1}Oe^{-1}$. The explicit variation of d_{dl} reveals a monotonous dependency of α_{ME} on d_{dl}, see Fig. 2.19 b). The absolute as-measured ME voltage U_{ME} is similar for all five presented samples with 35.3 ± 1.9 mV, which results in a thickness-normalized α_{ME}-value of 480 $Vcm^{-1}Oe^{-1}$ for the $d_{dl} = 4.6$ nm sample and a $\propto 1/x$ dependency of α_{ME} on d_{dl}. Hence, the reported dependence of α_{ME} on p_{O_2} [4, 5] must be regarded in part as a result of the varying d_{dl}. The variation of BTO-BFO thickness ratios from 1:9 to 9:1 in series of multilayers with $d_{dl} = 19.7 \pm 0.3$ nm, as presented in Fig. 2.19 c) has no substantial effect on α_{ME}. Across the ratio series, U_{ME} values vary only slightly around 35.1 ± 0.6 mV and the resulting α_{ME} values around 110 ± 3 $Vcm^{-1}Oe^{-1}$. In strain-coupled ME heterostructures consisting of piezoelectric and magnetostrictive materials, the dependency of α_{ME} on the volume fraction of the piezoelectric phase typically resembles an inverted bell curve [7], much unlike the plateau-behavior presented in Fig. 2.19 c). The variation of α_{ME} reported in [3] and shown in Fig. 2.19 b) can be said to depend on the total d_dl, and not just the individual BFO-layer thickness.

These measurements combined suggest that the true origin of the greatly enhanced ME coupling in the presented BTO-BFO multilayers does not lie strictly in mechanical coupling and microstrain distribution, but is rather to be considered an interface effect.

Various heterostructures have been reported where interface effects, rather than strain mediate the ME coupling. In $BaTiO_3/La_{2/3}Sr_{1/3}MnO_3$ heterostructures, e.g., or-

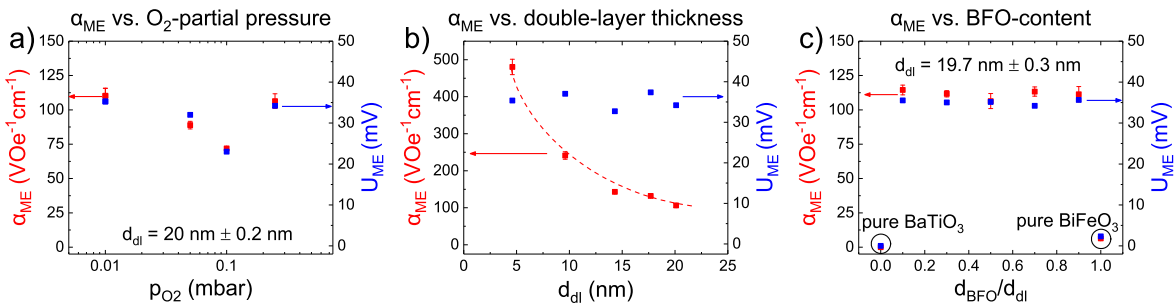

Figure 2.19: Magnetoelectric voltage (blue) and thickness-normalized magnetoelectric coupling coefficient (red) for multilayers under variation of a) oxygen pressure p_{O_2}, b) double-layer-thickness d_{dl}, and c) BTO-BFO ratio.

bital reconstruction was identified as the source of ME coupling [8]. The possibility of a thickness-dependent crossover from strain- to charge-mediated ME coupling was reported for $La_{0.7}Sr_{0.3}MnO_3/PbZr_{0.2}Ti_{0.8}O_3$ [9]. The occurrence of a similar effect could explain the observed non-dependency of the ME voltage on d_{dl} and the BTO-BFO ratio. This could also explain the scaling of α_{ME} with the number of double layers of BTO-BFO reported in [6], which showed a linear increase of α_{ME} from $16.1 \pm 3\,\mathrm{Vcm^{-1}Oe^{-1}}$ to $27.6 \pm 3\,\mathrm{Vcm^{-1}Oe^{-1}}$ for 2 to 20 double layers of $\propto 22\,\mathrm{nm}$ thickness.

[1] J. Ma *et al.*, *Adv. Mater.* **23**, 1062 (2011)
[2] J. Wang *et al.*, *Science*, **299** (5613), 1719-1722 (2003)
[3] S. Hohenberger *et al.*, *J. Phys. D: Appl. Phys.* **51**, 184002 (2018)
[4] M. Lorenz *et al.*, *Appl. Phys. Lett.* **106**, 012905 (2015)
[5] M. Lorenz *et al.*, *Adv. Mater. Interfaces*, 1500822 (2016)
[6] V. Lazenka *et al.*, *Appl. Phys. Lett.* **110**, 092902 (2017)
[7] M. I. Bichurin *et al.*, *Phys. Rev. B* **68**, 05402 (2003)
[8] B. Cui *et al.*, *Adv. Mater.* **27**, 6651 (2015)
[9] S. Spurgeon *et al.*, *ACS Nano* **8** (1), 894 (2014)

2.12 Femtosecond time-resolved spectroscopic ellipsometry

O. Herrfurth, L. Trefflich, M. Rebarz*, S. Espinoza*, T. Pflug†, M. Olbrich†, J.A. Leveillee‡, A. Schleife‡, M. Grundmann, A. Horn†, J. Andreasson*§, R. Schmidt-Grund

*ELI Beamlines, Institute of Physics, Czech Academy of Science, Prague, Czech Republic
†Laserinstitut Hochschule Mittweida,Schillerstr. 10, 09648 Mittweida, Germany
‡Department of Materials Science and Engineering, University of Illinois at Urbana-Champaign, Urbana, USA
§Condensed Matter Physics, Department of Physics, Chalmers University of Technology, Gothenburg, Sweden

2.12.1 Transient birefringence and dichroism in *m*-ZnO

The recently established collaboration between ELI Beamlines (Czech Republic) and Universität Leipzig led to the development of a set-up for pump-probe femtosecond time-resolved spectroscopic ellipsometry (tSE). It enables ellipsometric measurements with very high time resolution (200 fs) in a broad observable spectral range (1.8 eV to 3.6 eV). First experiment were conducted on 30 nm thin *c*-plane oriented chemZnO film on an amorphous glass substrate grown by pulsed laser deposition [1]. In this work, the dielectric function (DF) was modelled as isotropic because the experimental set-up is mostly sensitive to the DF tensor component perpendicular to the crystal's optic axis such that the optical anisotropy of ZnO is neglected. In subsequent experiments, the full DF tensor was obtained from measurements parallel and perpendicular to the crystal's optic axis on an *m*-plane oriented ZnO thin film grown by molecular beam epitaxy. The estimated UV-pump induced density of electron-hole pairs is $2 \times 10^{19}\mathrm{cm}^{-3}$. As a result, we observe transient birefringence and dichroism (Fig. 2.20) upon UV-pumping in the visible spectral range that is transparent under equilibrium conditions. The film becomes dichroic for a few ps in the spectral range below 2.0 eV and reveals an additional pseudo-isotropic point where $n_e = n_o$ but $\kappa_e \neq \kappa_o$. Comparison to the ZnO bandstructure and first-principles dielectric-function calculations provide evidence for inter-valence-band transitions of hot charge carriers near the M point in the Brillouin zone. The dipole transitions are governed by selection rules for light polarized perpendicular or parallel to the material's optic axis which can cause the transient optical anisotropy.

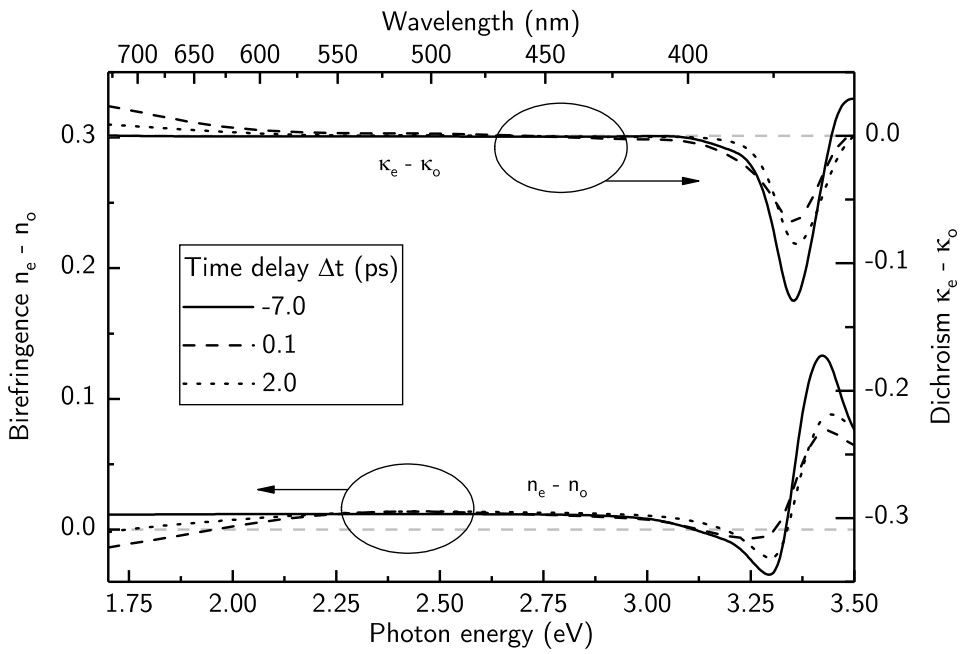

Figure 2.20: Transient optical anisotropy shown as birefringence $n_e - n_o$ and dichroism $\kappa_e - \kappa_o$ for selected pump-probe time delays Δt.

2.12.2 Comparison of the dielectric function with existing models for highly excited ZnO and conventional transient spectroscopy

In comparison to ellipsometry, conventional reflectance and transmittance measurements lack any phase information of the electromagnetic waves interacting with the sample. This is usually compensated for by before-hand assumptions on the physical processes that, however, can lead to incorrect conclusions. Reflectance and transmittance spectra can be reconstructed from the knowledge of the DF. We generate reflectance spectra based on the DF obtained by tSE and compare them to theoretical values of Versteegh et al. [2] which were refined by Wille et al. [3]. The underlying DF of Wille et al. allows to explain gain and lasing mechanisms in ZnO micro- and nanowires [4]. Both theoretical approaches are based on a solution of the Bethe-Salpeter equation [5] for a simplified ZnO-like bulk system. The reflectance spectra are exemplary for various different pump-probe reflectance studies on ZnO [6–9].

Symbols in Fig. 2.21 show the DF as obtained in this work at selected pump-probe time delays; lines represent theoretical curves according to Wille et al. for various carrier densities. Both studies find a decrease in the real and the imaginary part of the DF with increasing carrier density. The model of Wille et al. is about 100 meV blueshifted and predicts $\varepsilon_2 < 0$ which can lead to optical gain and lasing. This is not observed in our experiment due to the reflection geometry. Optical gain can only occur due to stimulated emission involving photons of equal wavevector (magnitude and direction). So-called gain spectroscopy was only reported in transmission geometry. Furthermore, it is seen that the theoretical curve of Wille et al. is not able to explain the features related to exciton-phonon complexes at 3.4 eV since electron-phonon interaction is neglected in the model. In the spectral range far below the band gap which is not covered by Wille et al., we find increased absorption which is related to the IVB absorption. The relative difference spectra of transmittance (panel b in Fig. 2.21) and reflectance (panel c) are computed for a structure consisting of 30 nm *c*-plane oriented ZnO on a glass substrate which is equivalent to the sample studied in this work. Reflection from the substrate backside is ignored. Changes around the absorption edge of ZnO are of the same order of magnitude for both using the DF from theoretical model (lines) and applying the DF obtained in this work. Surprisingly, in the spectral range of the IVB aborption the transmittance is increased although absorption appears. It is clear that the increased transmittance is related to decreased reflectance caused by the decrease in ε_1 and hence refractive index. This is in accordance with the Kramers-Kronig relations and is related to both, the occurring inter-valence-band absorption as well as the absorption bleaching at the absorption edge. We would like to emphasize here that interpretation of the conventional reflectance or transmittance changes can lead to erroneous conclusions about their physical origin because effects caused by changes in the real and imaginary part of the DF cannot be separated. Assuming a non-varying refractive index is insufficient and retrieval by exploiting the Kramers-Kronig relations is usually hampered by the limited spectral range.

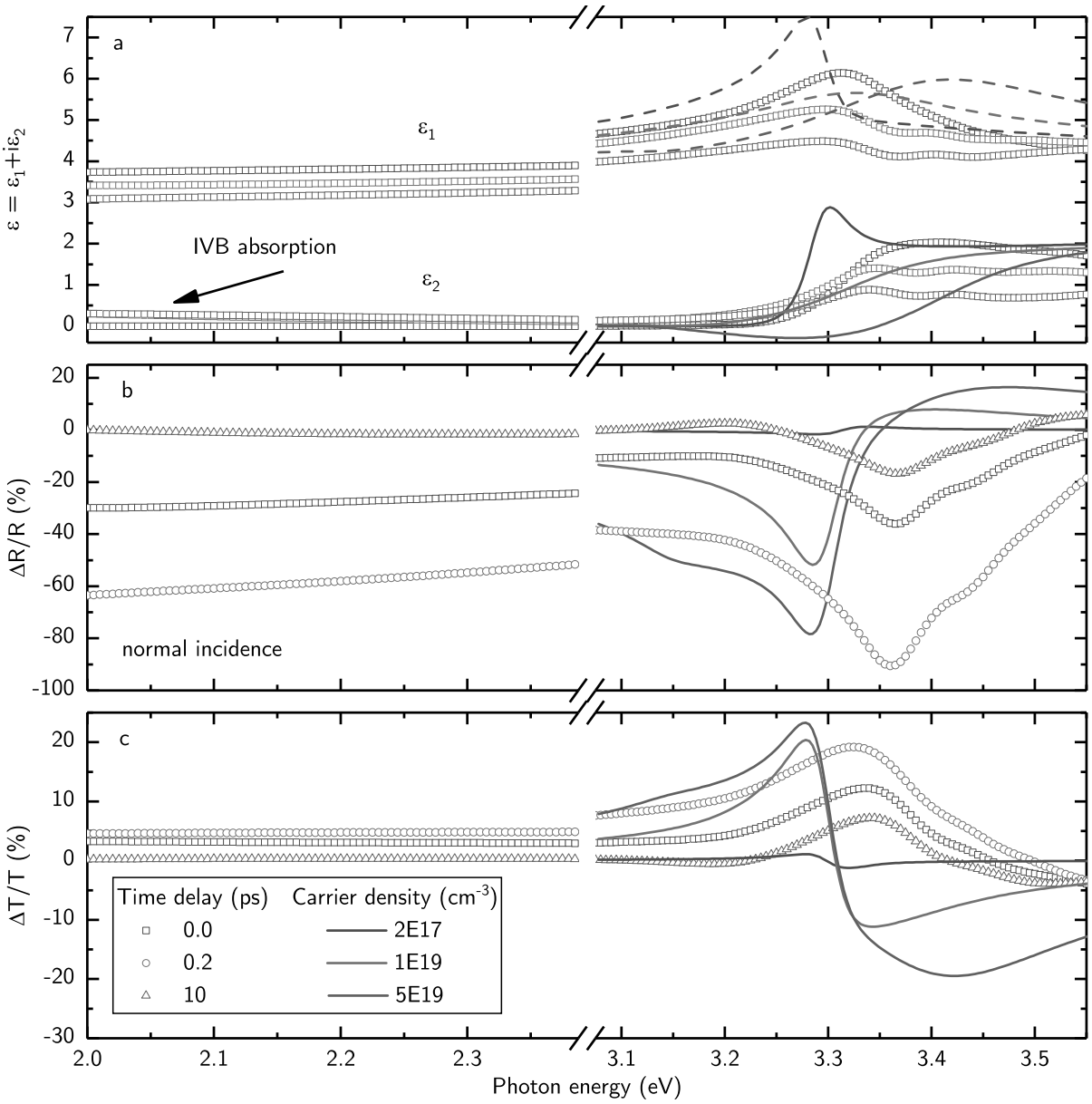

Figure 2.21: **a** DF of highly excited ZnO. Symbols represent the spectra obtained in this work at three different delays after photo-excitation. Lines show the expected spectra according to the model of Wille et al. for three different charge-carrier densities. **b** Computed transient reflectance and **c**: transmittance difference spectra at normal incidence for a 30 nm thin ZnO film on fused silica substrate according to the DFs in **a**. Note that although IVB absorption sets in, transmittance at lower energies increases upon pumping while reflectance decreases. This is caused by the lowered refractive index.

2.12.3 Spatially and time-resolved single-wavelength pump-probe ellipsometry on a *c*-ZnO thin film

Additional information on the transient physical processes in highly excited semiconductors can be obtained by performing time-resolved ellipsometry with spatial resolution [10, 11]. To this aim, joint experiments with the Laserinstitut Mittweida were conducted [11]. We report on spatially and time-resolved pump-probe ellipsometry

measurements performed on the same c-plane oriented ZnO thin film as in reference [1] using ultrafast single-wavelength probe radiation ranging from the near-IR to visible spectral range with a time resolution of approximately 50 fs. The ellipsometer is built in PSC_RA configuration which is favourable compared to the PC_RSA configuration [10] due to the non-moving spot of the probe beam. The imaging optics enables a magnification of factor 20 and the spatial resolution (<1 µm) is limited by the respective probe wavelength and the pixel size of the CCD detector. The thickness of the ZnO film is in the order of the optical penetration depth of the applied pump radiation (266 nm wavelength) whereby homogeneous optical excitation by single-photon absorption can be assumed throughout the entire film thickness. The fluence of the pump radiation is well below the ablation threshold and the induced charge carrier density is estimated to be approximately $1 \times 10^{20}\,\mathrm{cm}^{-3}$. The ellipsometric angles Ψ and Δ (Fig. 2.22) are obtained by numerical evaluation of reflectance-difference images for each measured angle of the compensator.

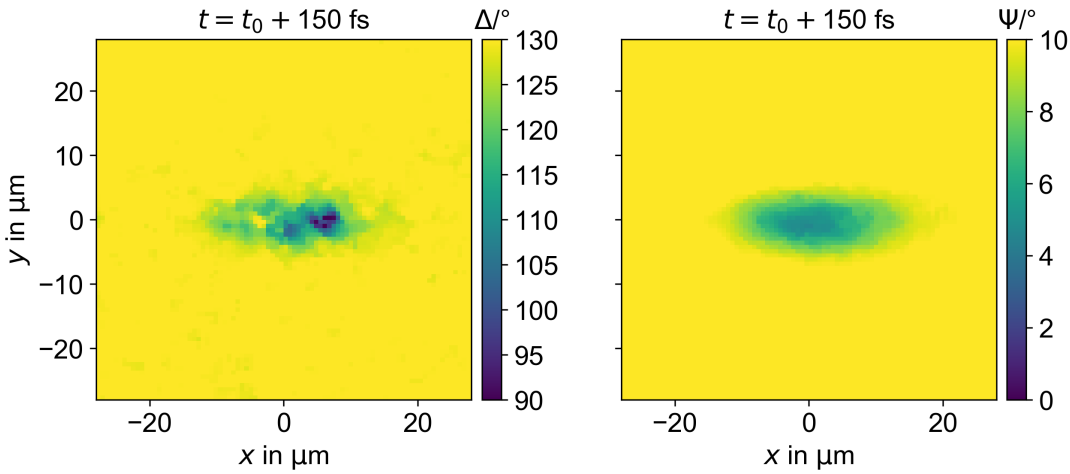

Figure 2.22: Spatially resolved ellipsometric angles Ψ and Δ obtained by pump-probe ellipsometry at time delay 150 fs and probe wavelength 515 nm. The dark area in the center corresponds to the spot of the pump laser.

Therewith, the transient wavelength-by-wavelength dielectric function (DF) is calculated via the transfer-matrix algorithm. We find a transient increase of the imaginary part of the DF simultaneous to a drop of the real part. This effect may be attributed to electronic transitions between different valence bands being possible as optically excited holes scatter to the edges of the Brillouin zone.

[1] S. Richter, *et al.*: arXiv:http://arxiv.org/abs/1902.05832v1 (2019)
[2] M. A. M. Versteegh, *et al.*: Phys. Rev. B **84** (2011) doi:10.1103/physrevb.84.035207
[3] M. Wille, *et al.*: Nanotechnology **27**, 225702 (2016) doi:10.1088/0957-4484/27/22/225702
[4] M. Wille, *et al.*: Appl. Phys. Lett. **109**, 061102 (2016) doi:10.1063/1.4960660
[5] H. Haug, S. W. Koch: *Quantum Theory of the Optical and Electronic Properties of Semiconductors* (WORLD SCIENTIFIC, 1990) doi:10.1142/0936

[6] T. Shih, *et al.*: Appl. Phys. A **96**, 363 (2009)
doi:10.1007/s00339-009-5196-0
[7] C. J. Cook, *et al.*: in *Oxide-based Materials and Devices*, edited by F. H. Teherani, *et al.*. (SPIE, 2010)
doi:10.1117/12.845636
[8] T. Shih, *et al.*: J. Appl. Phys. **109**, 043504 (2011)
doi:10.1063/1.3549614
[9] P.-C. Ou, *et al.*: Appl. Phys. B **106**, 399 (2011)
doi:10.1007/s00340-011-4706-x
[10] J. Csontos, *et al.*: Appl. Surface Science **421**, 325 (2017)
doi:10.1016/j.apsusc.2017.03.186
[11] T. Pflug, *et al.*: Appl. Phys. A **124**, 116 (2018)
doi:10.1007/s00339-018-1550-4

2.13 Voigt exceptional-points in an anisotropic ZnO-based planar microcavity: square-root topology and polarization vortices

S. Richter, H.-G. Zirnstein*, E. Krüger, J. Zúñiga-Pérez†, C. Deparis†, L. Trefflich, C. Sturm, B. Rosenow*, M. Grundmann, R. Schmidt-Grund

*Universität Leipzig, Institut für Theoretische Physik, Brüderstr. 16, 04103 Leipzig, Germany
†Université Côte d'Azur, CRHEA-CNRS, rue Bernard Gregóry, 06560 Valbonne, France

Exceptional points (EP) that represent topological charges, are of great interest in the recent research of topological non-trivial photonic systems. A particular class of such exceptional points are Voigt points [1], which represent the propagation directions in anisotropic crystals along which optical modes degenerate, leading to a single circularly polarized eigenmode. However, the presence of such EPs is not limited to bulk single crystals and can occur in a variety of systems described by non-Hermitian Hamiltonians, as e.g. planar microcavities with broken cylindrical symmetry [2], which allows to exploit a special kind of exceptional points, associated to propagation of circularly polarized light along specific directions, in widespread optoelectronic devices (e.g. VCSELs). The various design degrees of freedom of such microcavities render them an ideal model systems and allow to circumvent the limitations caused by the difficulties of modifying material absorption by counting on the dissipation by photon loss, instead. Thus, the occurence and direction of such exceptional points can be controlled by the geometrical microcavity design.

Here we report on dielectric, anisotropic optical microcavities, based on nonpolar m-plane oriented ZnO that implements a non-Hermitian system and mimicks the behaviour of natural Voigt points in anisotropic bulk crystals. The bottom distributed Bragg reflector (DBR), consisting of 16 pairs ZnO and $Mg_{0.29}Zn_{0.71}O$, as well as the cavity layer were fabricated by means of molecular beam epitaxy using m-plane oriented ZnO substrates [3], such that all ZnO and $Mg_{0.29}Zn_{0.71}O$ layers are m-plane oriented. The top-DBR was prepared non-epitaxially by pulsed laser deposition and consists of 6 pairs of Al_2O_3 and YSZ (Y-stabilized ZrO_2). The cavity layer thickness is tuned to 9/8 of the

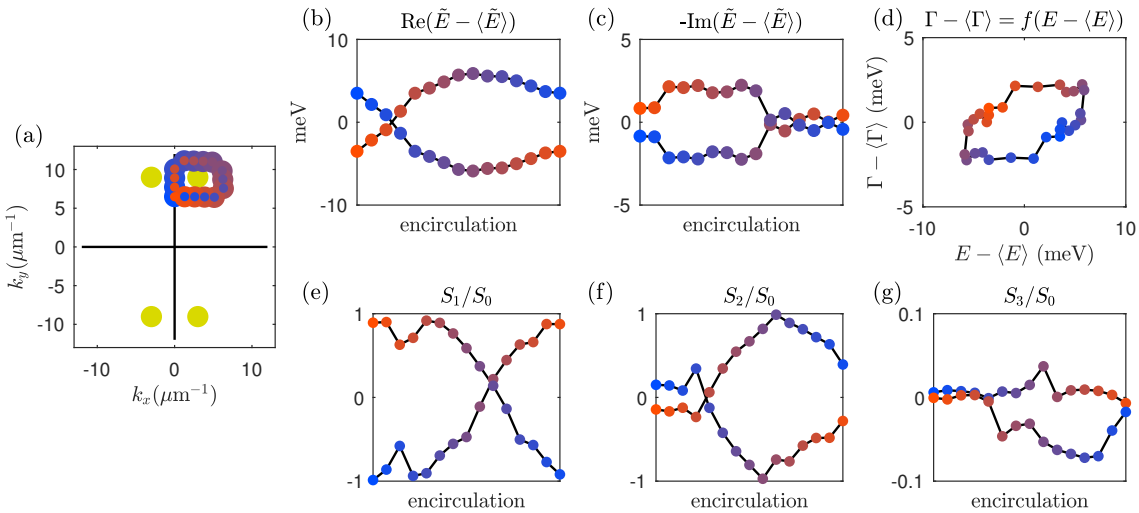

Figure 2.23: Overview of the trajectory corresponding to a clockwise encirclement of a Voigt exceptional point. (a): trajectory in the momentum space ($k_{||}$), (b): mode energy and (c): broadening along the path. Encircling once flips one mode to the other. (d): mode broadening as a function of mode energy along the path. (e,f,g): Stokes parameter spectra of the modes from the amplitudes of the Lorentz oscillators along the trajectory.

central wavelength of the DBR ($\approx$ 400 nm) and corresponds to a cavity photon mode energy of about 3 eV, such that the structure is working in the transparent spectral range of all used materials.

Polarization-resolved reflection experiments depending on the angle of incidence and sample azimuth angle were used to map the momentum space of the radiative modes. The achieved Stokes parameter spectra $\vec{S}(E)$ have been modeled simultaneously in a spectral range of 100 meV around the cavity modes, using Lorentzian peaks to describe the mode energy and broadening. The experimental positions of exhibited exceptional points, which can be identified as degeneracies of the complex mode energy, are reproduced by our theoretical calculations. The square-root topology of the mode energy surface around the Voigt exceptional points was proved by encircling such a point in the momentum space. As can be seen in Fig. 2.23 one roundtrip in momentum space yields a continuous exchange of the two modes, i.e. the energetically higher (and spectrally narrower) mode becomes the energetically lower (and broader) one and vice versa. Indeed only encircling the Voigt point twice restores the initial situation, as observed in the first experimental demonstration of exceptional points in a microwave cavity [4], proving that the observed Voigt points are indeed exceptional points.

[1] W. Voigt: The London, Edinburgh, and Dublin Philosophical Magazine and Journal of Science **4**, 19 (1902)
doi:10.1080/14786440209462820

[2] S. Richter *et al.*: Phys. Rev. A **95**, 023836 (2017)
doi:10.1103/PhysRevA.95.023836

[3] J. Zúñiga-Pérez *et al.*: Appl. Phys. Lett. **108**, 251904 (2016)
doi:10.1063/1.4954796

[4] C. Dembowski *et al.*: Phys. Rev. Lett. **86**, 787 (2001)
doi:10.1103/PhysRevLett.86.787

2.14 Structural and optical properties of carbon nanodot based planar microcavities

L. Trefflich, F. Dissinger*, C. Sturm, S.R. Waldvogel*, M. Grundmann, R. Schmidt-Grund

*Institute for Organic Chemistry, Johannes Gutenberg Universität Mainz, 55128 Mainz

Carbon nanodots (cdots) are discrete quasisphericle nanoparticles with diameters below 10 nm [1]. They can be synthesized from many carbon sources like tea, gras, coffee, and citric acid [1]. They are very eco-friendly and biocompatible [2] and show some interesting properties like photocatalysis [3] and a strong, tunable photoluminescence [4]. This has led to a number of interesting applications like chemical sensing[5] and the use as acitve laser material [6]. Our goal is to incorporate carbon nanodots in a verticle planar microcavity for LED and laser applications. In a verticle microcavity, the cavity layer has to fullfill the condition $n(\lambda) \cdot d = \lambda/2$, with the wavelength-dependent refractive index $n(\lambda)$, the layer thickness d and the design-wavelength λ. For a cdot emission wavelength of around 400 nm and a typical refractive index of gelatin of around 1.5 (at 400 nm) we find a minimum cavity thickness in the range of 130 nm. This is much larger than the cdot itself. Therefor, we need to incorporate them into a matrix which thickness we can control. A suitable cavity material has to fullfill a couple more conditions. The material has to be transparent, in order to avoid reabsorption of the cdot luminescence. Furthermore, the material should be ecofriendly and show no photoluminescence itself. We decided on commercial gelatin as a cavity material. In the first section of this work we report about the stuctural properties of the microcavities. In the second section we investigate the optical properties using angularly resolved microreflectivitiy measurements as well as microphotolumincescence spectroscopy.

2.14.1 Sample Fabrication and Structural Properties

The microcavity consists of two distributed bragg reflectors (DBR) and a cavity layer inbetween. The bottom DBR is made of 12 layer pairs YSZ and Al_2O_3 grown by pulsed laser deposition [7]. For the cavity layer we solved 10 mg cdots in ethanol using a ultrasonic cleaner and filtered the solution with a filter with 200 nm pore size. We than mixed 0.2 ml of this ethanol-cdot-solution with 1 ml liquid gelatin at 45°C. This mixture was then spincoated on the bottom DBR at 180 RPS for 3 min resulting in a layer thickness of around 600 nm. The top DBR was grown on top of that, again with pulsed laser depositon at room temperature. It has only 10 layerpairs, which gives a slightly lower reflectivity and helps to guide the light out of the upper side of the microcavity. Figure 2.24(a) shows an optical image of the whole sample. Large scale inhomogenities are easily visible due to a not fully optimized spin coating process. A scanning transmission electron microscope (STEM) image of a focussed ion beam (FIB) cut cross-section (figure 2.24(b)) shows a good homogeneity of the DBRs with smooth interfaces and a homogeneous cavity layer on the scale of a few micrometers.

2.14.2 Optical properties

Angularly resolved reflectivity measurements (spot size 5 μm) were used to determine the quality of the microcavity (figure 2.25(a)). The quadratic angular dispersion of the

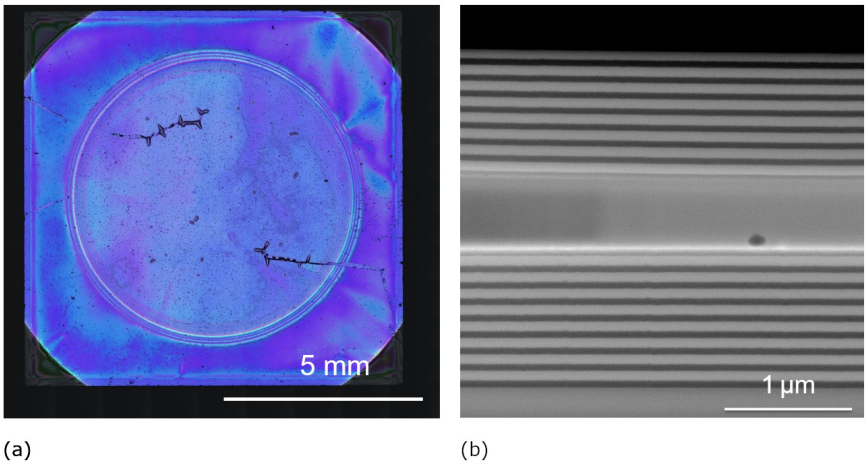

Figure 2.24: (a) Laser scanning microscope image of a carbon nanodot based planar microcavity. Millimeter scale inhomogeneities due to a not yet fully optimized spincoating process are visible. The top DBR has a smaller diameter to allow measurments of the cavity layer itself. (b) STEM image of a FIB lamella cut through the microcavity. The c-sapphire substrate, the bottom DBR, the gelatin cdot cavity mode as well as the top DBR are clearly visible. The cavity layer is homogeneous on the micrometer scale.

cavity mode is clearly visible. The energy of the cavity modes shifts from 3.00 eV at normal incidence to 3.06 eV for incidence angles of ±20° respectively. The qualtiy factor of the cavity mode decreases with increasing incidence angles, visible by the increasing linewidth of the mode. Therefor, the smallest linewidth is achieved at normal incidence. A linescan at normal incidence is shown in figure 2.25(b). The stop band of the resonator begins at 3.26 eV and ends at 2.64 eV. By fitting a Lorentzian model to the data, the energy of the cavitymode was determined to 3.00 eV with a linewidth 4.3 meV. We can therefore calculate the qualityfactor at normal incidence to 702 indicating a good quality resonator structure when investigated with a microspot.

Microphotoluminescence spectroscopy (excitation with Coherent Mira HP, 360nm, 200fs, 3MHz) shows strong photoluminescence in the energy range of the cavity mode (figure 2.26(a)). Because of the integration over all incidence angles between ±20° we see a broadened, asymmetric cavity mode. For increasing excitation densities we see a s-curved shape of the input-output charcteristic (figure 2.26(b)). Howhever, the slope is always lower than a linear increase, indicating only spontaneous emission with high losses from the sample. For excitation densities larger than 1 mJ we find a saturation behaviour because we are reaching the damage threshold of the carbon nanoparticles. The cavity mode shows a slight shift towards shorter wavelengths.To compensate for the increasing thermal losses at higher excitation intensities, the cavity mode shifts towards higher energies. Timeresolved measurements using a time-correlated single photon counting (TCSPC) setup show a biexponential decay for the luminescence of the cavity layer itself with time constants of 0.2 ns and 1.2 ns respectively. However, the luminescence of the cavity mode decreases with a time constant of 90 ps, which is roughly the time resolution of the setup. We can therefore conclude that there is amplification of the cdot emission through the cavity mode.

[1] P. Roy *et al.*: Mater Today **8**, 18 (2015)

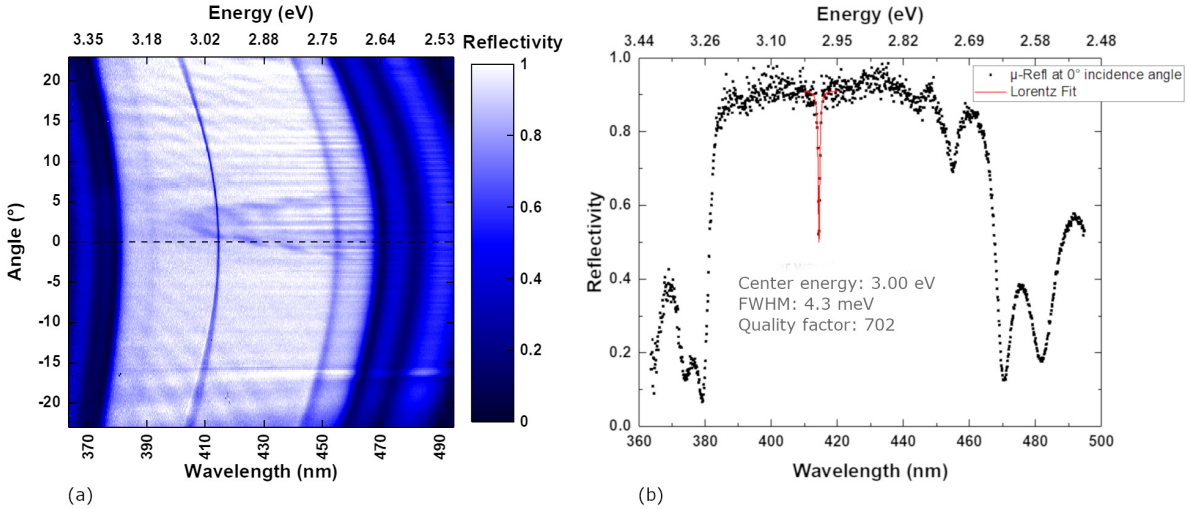

Figure 2.25: (a) Angularly resolved reflectivity measurement of the carbon nanodot based planar microcavity. The stopband of the microcavity (white area) and the cavity mode at 3.00 eV at normal incidence are visible. The cavity mode shows a quadratic angular dispersion, as expected. (b) Linescan of (a) for normal incidence (dashed line). A Lorentzian fit of the cavitymode gives an energy of 3.00 eV with a linewidth of 4.3 meV. That results in a quality factor of 702.

doi:10.1016/j.mattod.2015.04.005
[2] J.C.G.E. da Silva *et al.*: Trends Anal Chem **8**, 30 (2011)
doi:10.1016/j.trac.2011.04.009
[3] L. Cao *et al.*: J Am Chem Soc **13**, 133 (2011)
doi:10.1021/ja200804h
[4] Y. Sun *et al.*: J Am Chem Soc **24**, 128 (2006)
doi:10.1021/ja062677d
[5] Y. Dong *et al.*: Anal Chem **14**, 84 (2012)
doi:10.1021/ac3012126
[6] W.Zhang *et al.*: Nanoscale **9**, 5957 (2017)
doi:10.1039/c7nr01101f
[7] H. Hilmer *et al.*: AIP Conf Proc **1199**, 151 (2010)
doi:10.1063/1.3295340

2.15 Spectroscopic determination of cation distribution in ferrimagnetic spinel ferrite thin films

V. Zviagin, P. Huth [*], M. Bonholzer [†], C. Sturm, J. Lenzner, A. Setzer, R. Denecke [*], P. Esquinazi, M. Grundmann, R. Schmidt-Grund.

[*]Universtät Leipzig, Wilhelm-Ostwald-Institut für Physikalische und Theoretische Chemie, Linnéstr. 2, Germany.
[†]now at: Max-Planck-Institut für Extraterrestrische Physik, Giessenbachstr. 1, D-85748 Garching, Germany.

Remarkable capabilities of complex oxides are realized by the virtue of versatile ion

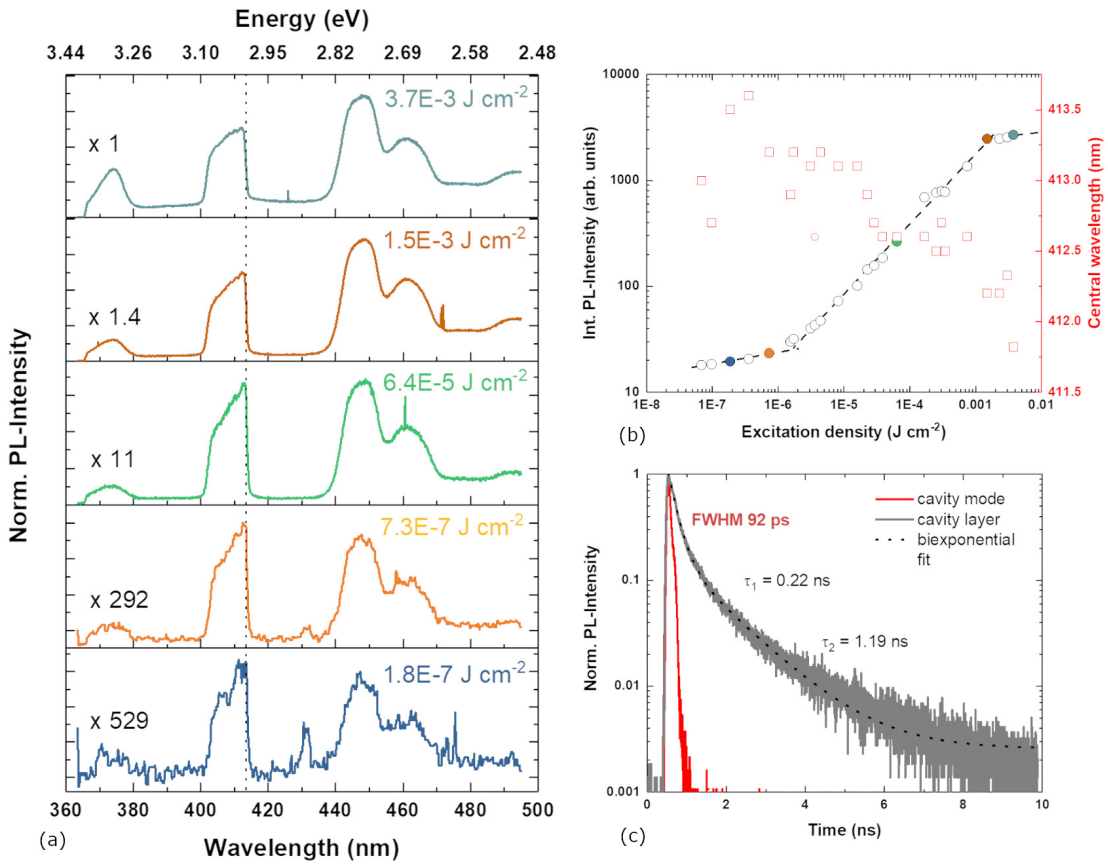

Figure 2.26: (a)Angularly integrated photoluminescence spectra of the carbon nanodot based microcavity for excitation densities from 1.8×10^{-7} Jcm^{-2}to 3.7×10^{-3} Jcm^{-2}. (b) The input-output characteristic of the device shows a slight s-curve with sublinear slope indicating only spontaneous emission. The damage threshold is reached for excitation densities higher than 1.5×10^{-3} Jcm^{-2}. The central wavelength of the cavity mode shows a slight shift towards shorter wavelengths. (c) The TCSPC measurements show a biexponential decay of the luminescence of the cavity mode with time constants of 0.2 ns and 1.2 ns. The luminecence of the cavity mode decays with a timeconstant of 90 ps. This is a clear sign for amplification of the cdot luminescence in the device.

arrangement within the crystallographic lattice. Particularly, transition metal oxides, MFe_2O_4 (M = Fe^{2+}, Zn^{2+}), exhibit a diversity of cation configurations, making them uniquely suitable for a vast scope of applications. As the inverse spinel configuration ($Fe^{2+}Fe_2^{3+}O_4$) is modified to a normal ($Zn^{2+}Fe_2^{3+}O_4$) by Zn substitution, the magnetic and electric properties of magnetite, a half-metallic ferromagnet, can be tuned to a ferrimagnetic semiconductor or to that of franklinite, a superparamagnetic insulator. Additionally, remarkable optoelectronic tunability, high thermal and chemical stability enables photoanode application of $ZnFe_2O_4$ for solar water oxidation[1]. $ZnFe_2O_4$ is considered to be antiferromagnetic with a Néel temperature of 10 K. It crystallizes in a normal spinel structure, where Zn^{2+} and Fe^{3+} cations occupy tetrahedral (Td) and octahedral (Oh) lattice site, respectively. The rise in conductivity in the insulating $ZnFe_2O_4$ with the decrease in deposition pressure has been related to the increase in Fe^{2+} concentration, due to intrinsic defects[2]. Theoretical works have shown that oxygen vacancies and tetrahedrally coordinated Fe^{3+} cations alter magnetic interactions, giving rise to

spontaneous magnetization at room temperature[3]. Furthermore, the formation of macroscopic defects, which show strong dependence on the substrate as well as the deposition temperature and atmosphere, result in an inhomogeneous cation configuration distribution within the thin film. Efforts to precisely determine the distribution of atomic species still remain technically challenging, and the mechanisms, responsible for the strong magnetic response in $ZnFe_2O_4$, are yet to be fully understood. The Zn^{2+} and Fe^{2+} cations preferentially occupy the Td- and Oh-sites, respectively, whereas the Fe^{3+} has no preference and could be distributed over both sites. Therefore, depending on the amount of disorder and inversion within the normal spinel structure, the formula for possible cation distribution can be given by $[(Zn^{2+}Fe^{3+}]_{Td}[Zn^{2+}Fe^{3+}Fe^{2+}]_{Oh}O_4^{2-}$.

Spectroscopic ellipsometry, in a wide spectral range (0.5 – 8.5) eV, was applied in order to probe the bulk cationic configuration in relation to the magnetic response, measured by superconducting quantum interference device (SQUID) and vibrating sample magnetometer (VSM). The dielectric function was approximated by a parametric model, consisting of Lorentzian, Gaussian and Critical Point Model functions, positioned at energies that correspond to electronic transitions. The model dielectric function (MDF) spectra was found to be dominated by transitions between d orbitals of Fe^{2+} ($\leq$1 eV), and transitions from O2p to Fe as well as Zn3d and 4s orbitals ($\geq$1 eV). Structural defects in the normal spinel, such as tetrahedral Fe^{3+} and octahedral Fe^{2+}, were evident from the strength of electronic transitions in the MDF spectra and showed a strong dependence on the substrate temperature and oxygen pressure, respectively. The transition involving Fe^{3+}_{Td} at 3.5 eV showed a strong magneto-optical response, determined by magneto-optical Kerr effect spectroscopy (MOKE)[4]. The presence of Fe^{3+} cations located on tetrahedrally coordinated lattice sites is due to the inversion mechanism, where the Zn^{2+} moves to octahedral and Fe^{3+} moves to tetrahedral lattice site, or to Fe^{3+} occupying nominally unoccupied tetrahedral lattice site. This would result in the antiferromagnetic oxygen mediated super-exchange (SE) interaction between Fe^{3+}_{Td} and Fe^{3+}_{Oh} to dominate over the ferromagnetic SE interaction between Fe^{3+}_{Oh} and Fe^{3+}_{Oh}. Therefore, the increase of the Fe^{3+}_{Td} cation transition strength in the MDF was directly correlated to the increase in magnetization saturation and remanence measured at 5 K with decreasing deposition temperature from 600 ℃ to 400 ℃[4]. Furthermore, the theoretical approximation of individual cation contribution to the X-ray photoelectron spectroscopy (XPS) Fe2p and 3p core level surface spectra allowed determination of Fe site occupation as well as an estimation of the relative concentration of individual cation.

$ZnFe_2O_4$ thin films were fabricated on $SrTiO_3$ substrates by pulsed laser deposition at 300 ℃ and at low (LPZFO) and high (HPZFO) oxygen partial pressures. The difference in the low energy features of the MDF is due to the presence of Fe^{2+}, as a likely result of oxygen vacancy formation in the LPZFO film, (Fig. 2.27(a)). The LPZFO and HPZFO films were subsequently annealed in oxygen and argon atmospheres, respectively, at temperatures varying from (250 – 375) ℃. The sample surface was found to become smooth and roughen after annealing in oxygen and argon environment, respectively. Annealing the films at 250 ℃ induces a small change in room temperature magnetization saturation which could be attributed to change in cation distribution in the surface layer. A significant change to the MDF line-shape, after annealing the films at higher temperatures, is coincident with the decrease in the magnetic response, (Fig. 2.27(b)). This behavior can be explained by a cation redistribution mechanism, as

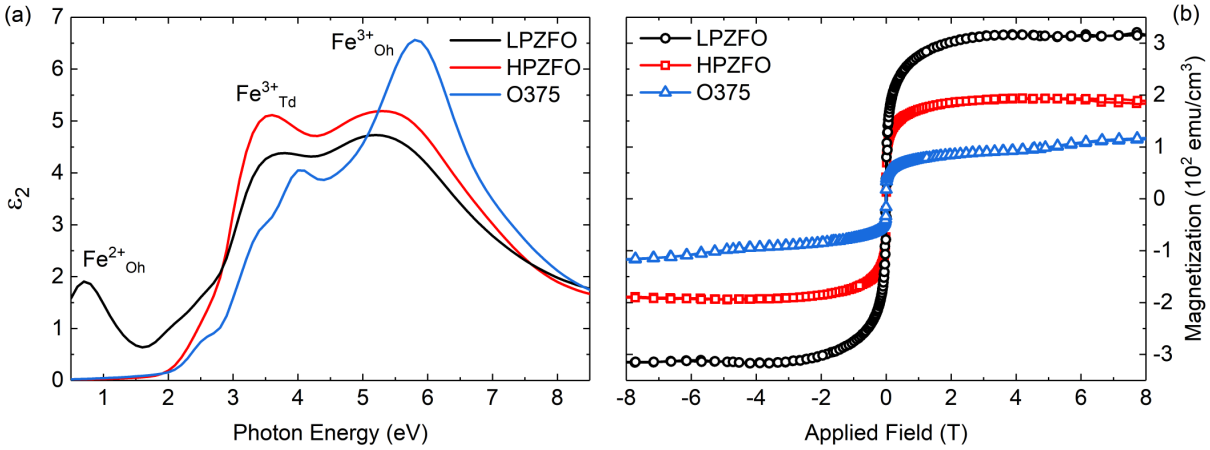

Figure 2.27: (a) Model dielectric function (ϵ_2), determined from spectroscopic ellipsometry for the $ZnFe_2O_4$ films grown at low (LPZFO) and high (HPZFO) oxygen pressure as well as annealed at 375 ℃ in oxygen atmosphere (O375). The distinct features result from transitions involving Fe cations on octahedral (Oh) and tetrahedral (Td) lattice sites. (b) Room temperature magnetization as a function of applied magnetic field for the respective films from (a).

the disordered spinel tends to a more stable, normal configuration. This is evident by a decrease (increase) in the peak involving tetrahedrally (octahedrally) coordinated Fe^{3+} cations in the MDF spectra.

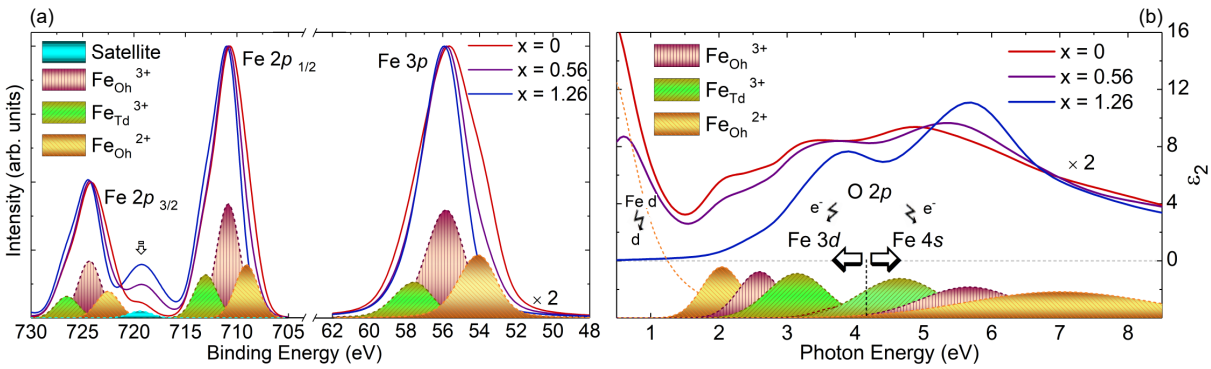

Figure 2.28: (a) Model approximation to the measured surface Fe2p and 3p XPS core level spectra without the Shirley background and (b) the bulk MDF for the x = 0, 0.56 and 1.56 thin films. XPS intensity of the resulting fit and ϵ_2 approximation line-shapes are multiplied by a factor of two for clarity. The individual Fe cation contribution to the modeled spectra for chemical composition determination are indicated by the shaded areas. The satellite contribution between the XPS $Fe2p_{3/2}$ and $2p_{1/2}$ core levels is indicated by an arrow.

The surface and bulk cation configuration was investigated as a function of Zn concentration in the $Zn_xFe_{3-x}O_4$ thin films with x varying from (0 – 1.26). The clear distinction in the XPS spectra with increase in Zn concentration is evident by the decrease of the low energy shoulder in both Fe2p and 3p core levels as well as the increase in the satellite peak at 719 eV, (Fig. 2.28(a)). The contribution of the MDF transitions involving Fe^{2+} cations decreases at a nearly linear rate as the Zn concentration increases, (Fig. 2.28(b)). This is due to the preservation of charge neutrality as Zn^{2+} replaces the Fe^{3+} on tetrahedral lattice sites. The surface morphology of the x = 0 film was found

to be dominated by large grain-like structures, which are likely due to the formation of antiphase boundaries. The homogeneous film formation in the x = 0.87 film is in coincidence with a uniform cation distribution (Fig. 2.29), smooth surface morphology and Bloch law behavior of the magnetization as a function of temperature. It was determined that the bulk (surface) of spinel ferrite film in its predominantly inverse configuration ($x \leq 0.56$), would be primarily occupied by Fe^{3+}_{Td} (Fe^{3+}_{Oh}), while that of a normal spinel (($x \geq 0.87$)) would be occupied by Fe^{3+}_{Oh} (Fe^{3+}_{Td}), (Fig. 2.29). While the former results in a diminishing ferrimagnetic order in inverse spinel magnetite, the latter mechanism could be responsible for the strong magnetic response in the disordered $ZnFe_2O_4$ thin film.

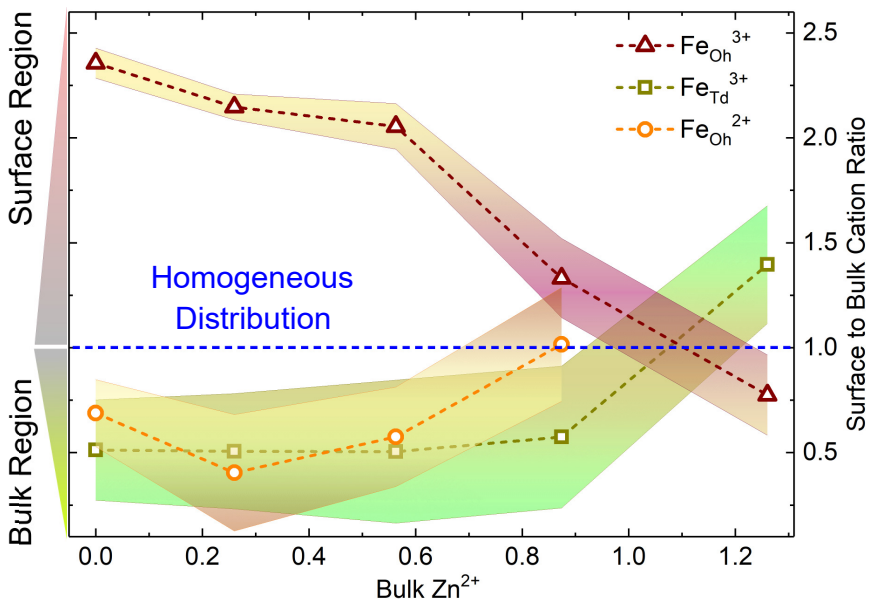

Figure 2.29: Relative surface to bulk cation concentration Fe ratio as a function of Zn^{2+}. The horizontal dashed line represents the ratio value for homogeneous distribution. The errors are indicated by the shaded regions.

[1] N. Guijarro *et al.*: Sustainable Energy Fuels **2**, 103 (2018) doi:10.1039/C7SE00448F
[2] K. Brachwitz *et al.*: Appl. Phys. Lett. **102**, 172104 (2013) doi:10.1063/1.4803475
[3] C. R. Torres *et al.*: Phys. Rev. B **89**, 104411 (2014) doi:10.1103/PhysRevB.89.104411
[4] V. Zviagin *et al.*: Phys. Status Solidi **253**, 429 (2016) doi:10.1002/pssb.201552361
[5] V. Zviagin *et al.*: Appl. Phys. Lett. **108**, 13 (2016) doi:10.1063/1.4944898

2.16 Temperature dependence of the dielectric function of thin film CuI in the spectral range (0.6 - 8.3) eV

E. Krüger, V. Zviagin, C. Yang, C. Sturm, R. Schmidt-Grund, M. Grundmann

γ -CuI is a wide band gap p-type semiconductor with a high exciton binding energy [1], high hole mobility [2] and the best known thermoelectric properties in comparison with other transparent p-type thermoelectric materials [3], and thus a promising material for transparent optoelectronic and thermoelectric devices. Although CuI thin films can be easily prepared at room temperature [4] and were already successfully applied in e.g. transparent p-n-heterojunctions [5], there have been a lack of detailed investigation of the optical properties, escpecially of the temperature dependent dielectric function in a wide spectral range, which is crucial for understanding the nature of the underlying transitions in the electronic structure, so far.

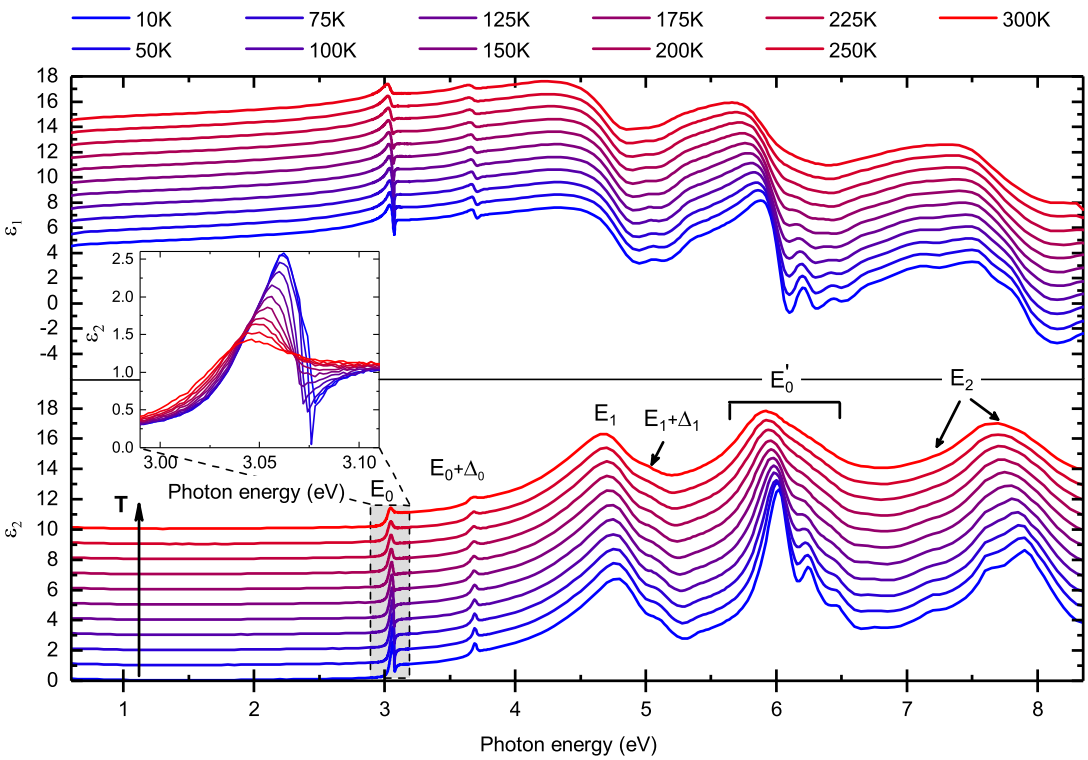

Figure 2.30: Spectra of the real (ε_1) and imaginary (ε_2) part of the dielectric function of the CuI thin film as a function of temperature. The spectra are shifted vertically by one against each other for better clarity. The inset shows ε_2 near the excitonic resonance E_0 (shaded area).

Thus, we determined the dielectric function of high quality γ-CuI thin film by means of spectroscopic ellipsometry in the spectral range from 0.6 eV up to 8.3 eV for temperatures from 10 K to 300 K [6]. In order to improve the crystalline quality as well as the surface morphology, which is favorable for reliable ellipsometry investigations, CuI thin films with different thicknesses in the range (30 – 150) nm were deposited on Al_2O_3 substrates at 360 °C and the film, exhibiting the best structural properties, was used for the temperature dependent ellipsometric measurements. Further ellipsometric measurements on similar thin films at room temperature were performed to verify, that the

achieved results are specific for CuI thin films. The dielectric function was determined numerically by a Kramers-Kronig consistent point-by-point regression analysis of the experimental data using the Levenberg-Marquardt algorithm and the transition energies were estimated from the zero crossing of the first-derivative spectra $d\varepsilon_2/dE$, which were smoothed using Savitzky-Golay-Filter [7] after the numerical differentiation.

As can be seen in Fig.2.30 the investigated thin film is almost fully transparent in the spectral range (1 – 3) eV. For photon energies above 3 eV the dielectric function is dominated by various peak structures, which are attributed to electronic transitions at different symmetry points in the Brillouin zone and are labelled as E_0 (3.1 eV, $E_0+\Delta_0$ (3.7 eV), E_1 (4.7 eV), $E_1+\Delta_1$ (5.1 eV), E_0 (6 eV), and E_2 (7.6 eV), in accordance with the nomenclature introduced by Cardona [8]. The observed split-off energies of 630 meV at the Γ -point and approximately 330 meV at the L-point coincide with recent band structure calculations [9]. In the investigated temperature range the change of the observed features is dominated by red shift of the transition peak energies as well as strong broadening with increasing temperature, related to thermal lattice expansion and increasing electron-phonon interaction with increasing temperature. Thus, the temperature dependence of the observed transition energies can be described by a Bose-Einstein model, presented by Viña *et al*. [10], and thus the electron-phonon coupling strength as well as the average phonon energy can be deduced. The determined temperature dependent energy shift of the transitions at the Γ -point ($E_0, E_0 + \Delta_0$) yields a coupling strength of about α = 0.08 meV/K, indicating weak electron-phonon coupling and an average phonon energy of 16 meV, which agrees with the LO-phonon energy in CuI. For high energy transitions ($E_1, E_1 + \Delta_1, E_0'$) the coupling constant was determined to be about 0.4 meV/K indicating a stronger electron-phonon coupling to phonons with an average energy of approximately 7 meV.

[1] T. Sauder *et al.*: Phys. Lett. A **101**, 55 (1984)
doi:10.1016/0375-9601(84)90092-6

[2] D. Chen *et al.*: Crystal Growth & Design **10**, 2057 (2010)
doi:10.1021/cg100270d

[3] C. Yang *et al.*: Nat. Commun. **8**, 16076 (2017)
doi:10.1088/1361-648X/aa9e2a

[4] M. Grundmann *et al.*: Phys. Status Solidi A **210** 1671 (2013)
doi:https://doi.org/10.1002/pssa.201329349

[5] C. Yang *et al.*: Sci. Rep. **6**, 21937 (2016)
doi:10.1021/ac60214a047

[6] E. Krüger *et al.*: Appl. Phys. Lett. **113**, 172102 (2018)
doi:10.1063/1.5051963

[7] A. Savitzky and M. J. E. Golay: Analytical Chemistry **36**, 1627 (1964)
doi:10.1021/ac60214a047

[8] M. Cardona: Phys. Rev. **129**, 69 (1963)
doi:10.1103/PhysRev.129.69

[9] Y. Li *et al.*: Phys. Rev. Mater. **2**, 035003 (2018)
doi:10.1103/PhysRevMaterials.2.035003

[10] L. Viña *et al.*: Phys. Rev. B **30**, 1979 (1984)
doi:10.1103/PhysRevB.30.1979

2.17 Applicability of the constitutive equations for optical active materials

C. Sturm, V. Zviagin, M. Grundmann

Optical activity is an intrinsic material property leading to a circular birefringence and dichroism. Typically, the optical activity is determined by transmission spectroscopy, which limits these investigations to the transparent spectral region. However, due to the boundary condition the change of the polarization state of the transmitted wave, caused by the optical activity, affects also the polarization of the reflected wave. This allows to determine the optical activity by ellipsometry as it was recently demonstrated on $AgGaS_2$ [2]. The optical response of such materials cannot be described by the dielectric function only and the constitutive equations have to be extended by the pseudo gyration tensor. Typically, three different approaches are proposed [1], namely the so-called Fedorov-Condon, Landau and Drude-Berreman approach. Although it was already shown that only the Fedorov-Condon approach does not lead to a violation of the conservation of the energy at the interface, all three approaches are still used in the literature for the analysis of optically active materials (cf. [3, 4]).

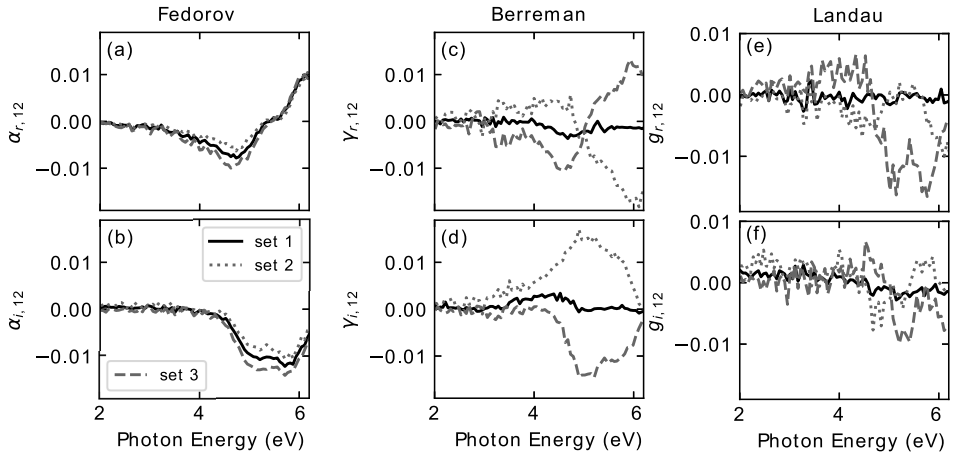

Figure 2.31: Determined gyration tensor by using the Fedorov (a,b), Berreman (c,d) and Landau approach (e,f) for the constitutive equations by taking into account different sets of crystallographic orientations

We investigated the impact of the choice of the constitutive equation on the optical properties. In doing so, we analyzed the optical response of potassium titanyl phosphate ($KTiOPO_4$, KTP), determined by spectroscopic ellipsometry for the different approaches of constitutive equations. Since KTP has an orthorhombic crystal structure and thus it is optically biaxial, for the determination of the optical properties by means of ellipsometry the optical response for different crystallographic orientations with respect to the laboratory system have to be measured and analyzed simultaneously. In order to investigate the validity of the different approaches, we analyzed three different sets of crystallographic orientations. Whereas the determined dielectric function for the different constitutive equations and crystallographic orientation yield similar results, the magnitude of the gyration tensor depends strongly on the choice of the constitutive equation [5]. In the case of the Fedorov-Condon approach, the gyration tensor is well

pronounced in the absorption spectral range and reaches values up to ±0.01. This is in contrast to the Landau and Drude-Berreman approach where the gyration tensor is negligible in the entire spectral range or rather only pronounced at an energy of about 4 eV (Fig. 2.31). Furthermore, we found that only in the case of the Fedorov-Condon approach, the determined gyration tensor does not depend on the crystallographic orientations which were taken into account. This finding can be explained by the fact, that the Fedorov-Condon approach consists of a symmetric set of constitutive equation where the impact of the optical activity on the magnetic field and flux density is directly taken into account whereas in the case of a non-symmetric set of constitutive equation, as given by the Landau and Drude-Berreman approach, this impact is described indirectly [5]. Thus, only a symmetric set of the constitutive equations as proposed by the Fedorov-Condon approach allows the unique determination of the pseudo gyration tensor.

[1] A. F. Konstantinova *et al.:* Crystallogr. Rep. **47**, 815, (2002) doi:10.1134/1.1509398
[2] O. Arteaga, Opt. Lett. **40**, 4277 (2015) doi:10.1364/OL.40.004277
[3] Y. Sah and J. G. Krishna: J. Opt. Soc. Am. A **18**, 1388 (2001) doi:10.1364/JOSAA.18.001388
[4] V. M. Agranovich and V. Ginzburg, *Crystal Optics with Spatial Dispersion, and Excitons* (Springer Science & Business Media, 2013)
[5] C. Sturm *et al*: Opt. Lett. **44**, 1351 (2019) doi:10.1364/OL.44.001351

2.18 Observation of the unpolarized Brewster point in the sky

M. Scholz*, O. Herrfurth, L. Trefflich, S. Richter, M. Grundmann, R. Schmidt-Grund

*Gymnasium Engelsdorf, Arthur-Winkler-Str. 6, 04319 Leipzig, Germany

Sunlight is mostly linearly polarized due to scattering from molecules in the atmosphere. The physical origin is Rayleigh scattering on molecular dipoles. It is interesting that multiple Rayleigh scattering processes lead to linearly polarized light with its polarization perpendicular to that of single Rayleigh scattering and the superposition of both results in the appearance of four unpolarized points in the sky [1, 2]. During a two-weeks pupil internship in 2016, a wide-angle map of the polarization pattern of the sky was measured and the Babinet point was observed above the sun as seen from the observer [3]. An improved set-up was build during a second internship in July 2018. The commercial digital camera was replaced by a very sensitive CCD camera equipped with a camera objective (±15° field of view). Thereby, the observable field of view is is smaller compared to the first experiment but the angular resolution increased. Employing a metal interference filter for 515 ± 12 nm wavelength further improves the resolution such that the unpolarized points in the sky are not smeared out by different spectral contributions. Polarization resolution was realized with a commercial "circular polarization filter", i.e a quarter-wave plate attached to linear polarizer. On Friday 13th July 2018 13:31, the unpolarized point below the sun and just above the horizon was

observed as demonstrated by the vortex of the polarization orientation in Fig. 2.32. This point is called "Brewster point" and it is hidden below the horizon most of the time because of the low declination of the sun. The declination was 62.2° at this time such that the Brewster point was just high enough to be observed. The polarization pattern is smeared out and the degree of polarization is far below one due to the depolarizing contributions of clouds and haze in the sky, which were not even visible to the bare eye but only could manifest themselves by depolarization.

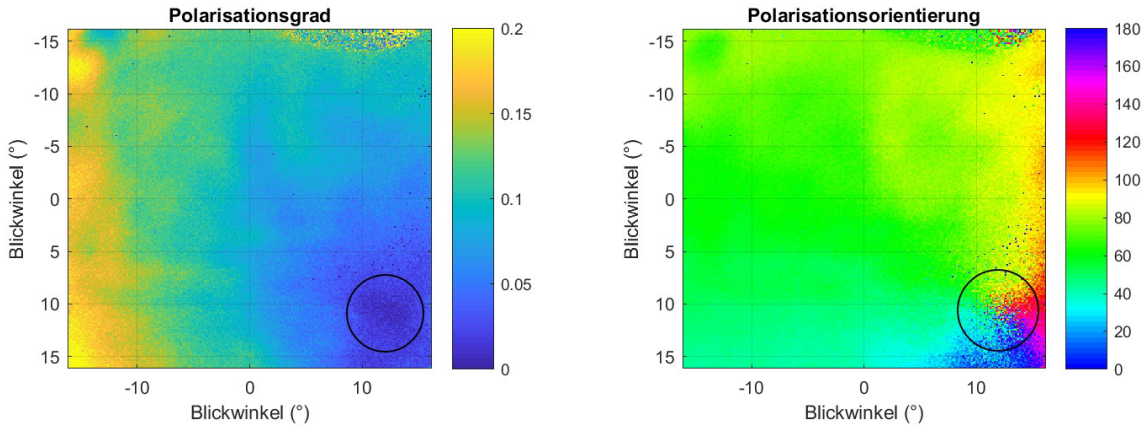

Figure 2.32: Degree of polarization (left) and orientation (right) of the polarized light (wavelength 515 ± 12 nm) observed in the sky above Leipzig (51°20′N 12°23′E) at the 13th July 2018, 13:31 just above the horizon. The declination of the sun was 62.2°. The vortex in the polarization orientation corresponds to the unpolarized Brewster point.

[1] S. Chandrasekhar: *Radiative transfer*, International series of monographs on physics (Clarendon Press, Oxford, 1950)
https://katalog.ub.uni-leipzig.de/Record/0001022152

[2] G. Horváth, *et al.*: Appl. Optics **41**, 543 (2002)
doi:10.1364/ao.41.000543

[3] M. Scholz et al.: *Polarization patterns of the sky*, in *Report Halbleiterphysik/Semiconductor Physics 2016*
http://research.uni-leipzig.de/hlp/publications/HLP-Report-2016.pdf

3

Funding, Organizational Duties, External Cooperations

3.1 Funding

Polarisationswechselwirkung in Laser-MBE Wurtzit-Perowskit-Heterostrukturen
Prof. Dr. M. Lorenz
SFB 762/3, TP A2 within SFB 762 *Funktionalität Oxidischer Grenzflächen*

Optische Untersuchungen zu magneto-elektro-optischen Wechselwirkungen in ihrer Dynamik in oxidischen Heterostrukturen
Dr. R. Schmidt-Grund
SFB 762/3, TP B03 within SFB 762 *Funktionalität Oxidischer Grenzflächen*

Lateraler Transport in oxidischen Feldeffekt-Strukturen
Dr. H. von Wenckstern, Prof. Dr. M. Grundmann
SFB 762/3, TP B04 within SFB 762 *Funktionalität Oxidischer Grenzflächen*

Spinabhängiges Tunneln in oxidischen Heterostrukturen
Prof. Dr. M. Grundmann, Prof. Dr. B. Rosenow
SFB 762/3, TP B06 within SFB 762 *Funktionalität Oxidischer Grenzflächen*

Quantum Gases and Liquids in Semiconductor Rods conformally coated with Bragg Mirrors
Dr. R. Schmidt-Grund, Prof. Dr. M. Grundmann
DFG SCHM 2710/2-2, TP P1 within FOR 1616 *Dynamics and Interactions of Semiconductor Nanowires for Optoelectronics*

Flexible analoge und digitale Grundschaltungen in amorphen Metalloxiden
Prof. Dr. M. Grundmann
DFG GR 1011/31-1, within SPP *High Frequency Flexible Bendable Electronics for Wireless Communication Systems (FFLexCom)*

Raman-Streuung in anisotropen Kristallen
Prof. Dr. M. Grundmann
GR 1011/33-1

Topologische Effekte in optisch-anisotropen Mikrokavitäten
Dr. R. Schmidt-Grund
DFG SCHM 2710/3-1

Wurtzitische Zink-basierte Oxynitride als vielversprechende photovoltaische Absorber: Epitaxie, Bandstruktur-Anpassung und Heterostrukturen
Dr. C. Yang
YA 511/1-1

Zink-Magnesium Oxinitride
Prof. Dr. M. Grundmann
GR 1011/36-1

LOMID - Large cost-effective OLED microdisplays and their applications
Prof. Dr. M. Grundmann, Dr. H. von Wenckstern
European Union, Horizon 2020 644101

COSIMA - Combinatorisches Oxide-Screening für Materialien und Anwendungen
Prof. Dr. M. Grundmann
Europäischer Fonds für regionale Entwicklung (EFRE)
100282338 and 100315366

Nachwuchsforschergruppe - Oxid-Heterostrukturen: Anwendungen in Bauelementen
Prof. Dr. M. Grundmann
Europäische Sozialfonds (ESF)
100310460

3.2 Organizational Duties

M. Grundmann

- Director of the Felix Bloch Institute for Solid State Physics
- Sprecher der Graduiertenschule "Leipzig School of Natural Sciences - Building with Molecules and Nano-objects" (BuildMoNa), http://www.buildmona.de/
- Stellvertretender Sprecher des Sonderforschungsbereiches "Funktionalität Oxidischer Grenzflächen" (SFB762), http://www.physik.uni-halle.de/sfb762/
- Stellvertretender Sprecher der Forschergruppe FOR 1616, http://www.for1616.uni-jena.de/
- Sprecher der Fächerübergreifenden Arbeitsgemeinschaft Halbleiterforschung Leipzig (FAHL), https://home.uni-leipzig.de/fahl/
- Mitglied des wissenschaftlichen Beirats des Leibniz-Instituts für Oberflächenmodifizierung e. V., Leipzig (IOM)
- Member Editorial Board: Physica Status Solidi (a), (b), RRL, MDPI nanomaterials
- Member International Advisory Board: Advanced Electronic Materials
- Project Reviewer: Deutsche Forschungsgemeinschaft (DFG), Alexander von Humboldt-Stiftung (AvH), Schweizerischer Nationalfonds zur Förderung der wissenschaftlichen Forschung (FNSNF), Fonds zur Förderung der Wissenschaften (FWF), EU, Ös-

terreichische Forschungsförderungsgesellschaft mbH (FFG), Agence Nationale de la Recherche (ANR, France)
- Referee: Applied Physics Letters, Electronics Letters, Journal of Applied Physics, Nature, Physica E, Physical Review B., Physical Review Letters, Physica Status Solidi, Advanced Materials, u.a.

M. Lorenz
- Member Editorial Board: Journal of Physics D: Applied Physics (IOP, Bristol, U.K.)
- Project Reviewer: Deutsche Forschungsgemeinschaft (DFG), Dutch Research Council NWO (Niederlande), Alexander von Humboldt Stiftung, Public Authority of Applied Education and Training (PAAET) – College of Technological Studies (Kuwait)
- Referee: ACS Applied Materials Interfaces, ACS Applied Nano Materials, Applied Physics Letters, Applied Surface Sciences, Applied Physics A, Crystal Growth and Design, CrystEngComm, Dalton Transactions, IEEE Transact. Magnetics, Journal of Alloys and Compounds, Journal of Physics D: Applied Physics, Journal of Applied Physics, Journal of Materials Research, Journal: Optics and Laser Technology, Journal of Magnetism and Magnetic Materials, Materials Science in Semiconductor Processing, Materials Horizons, Thin Solid Films

R. Schmidt-Grund
- Extended board member of German Association on Ellipsometry (Arbeitskreis Ellipsometrie – Paul Drude e.V.)
- Project Reviewer: Deutsche Forschungsgemeinschaft (DFG), US Department of Energy, Österreichische Akademie der Wissenschaften, German-Israeli Foundation for Scientific Research and Development
- Referee: Scientific journals (ACS, AIP, APS, DPG, Elsevier, IOP, MRS, Nature Publ. Group, OSA, PIER,Wiley)

C. Sturm
- Referee: Applied Optics, Applied Physic Letters

H. von Wenckstern
- Project Reviewer: Deutsche Forschungsgemeinschaft, U.S. Department of Energy – Office of Science, National Research Fondation RSA
- Associate Editor: Journal of Electronic Materials
- Referee: ACS Materials and Interfaces, Advanced Functional Materials, Annalen der Physik, Applied Physical Letters, APL Materials, Electronic Device Letters, Journal of Applied Physics, Material Science in Semiconductor Processing, Physica Status Solidi, Scientific Reports, Solid State Electronics, Superlattices and Microstructures, Thin Solid Films, u.a.

C. Yang
- Referee: Materials Horizons, Applied Physics Letters, Physical Review Applied, Nanoscale, Advanced Materials Interfaces

3.3 External Cooperations

Academic

- Leibniz-Institut für Oberflächenmodifizierung e. V., Leipzig, Germany
  Prof. Dr. A. Anders, Prof. Dr. S. Mayr, Dr. C. Bundesmann, Dr. A. Lotnyk
- Universität Leipzig, Fakultät für Chemie und Mineralogie, Germany
  Prof. Dr. H. Krautscheid, Prof. Dr. R. Denecke, Porf. Dr. O. Oeckler, Dr. S. Blaurock
- Universität Halle-Wittenberg, Germany
  Prof. Dr. I. Mertig, Prof. Dr. S.G. Ebbinghaus, Prof. Dr. W. Hergert, Prof. Dr. R. Scheer
- Fraunhofer-Institut für Mikrostruktur von Werkstoffen und Systemen IMWS, Halle (Saale), Germany
  Prof. Dr. T. Höche, Dr. C. Patzig, Dr. S. Selle
- Forschungszentrum Dresden-Rossendorf, Germany
  Dr. S. Zhou
- Technische Universität Berlin, Germany
  Prof. Dr. A. Hoffmann
- Humboldt-Universität zu Berlin, Germany
  Prof. Dr. N. Koch
- Leibniz-Institut für Festkörperelektronik – Paul Drude (PDI), Berlin, Germany
  Dr. O. Bierwagen
- Universität Magdeburg, Germany
  Porf. Dr. A. Dadgar, Dr. J. Bläsing
- Universität Jena, Germany
  Prof. Dr. C. Ronning, Prof. Dr. S. Botti
- University of Canterbury, Christchurch, New Zealand
  Prof. Dr. M. Allen
- Centre de Recherche sur l' Hétéro-Epitaxie et ses Applications (CNRS-CRHEA), Valbonne, France
  Dr. J. Zúñiga-Pérez, Dr. Guy Feuillet
- Western Michigan University, USA
  Prof. Dr. S. M. Durbin
- The Ohio State University, USA
  Prof. Dr. L. Brillson
- Katholieke Universiteit Leuven, Belgium
  Dr. V. Lazenka, Prof. Dr. K. Temst
- University of Oslo, Norway
  Prof. Dr. L. Vines

Industry

- Freiberger Compound Materials GmbH, Freiberg, Germany
  Dr. G. Leibiger

4

Publications

Journals

A. Bouvet-Marchand, A. Graillot, J. Volk, R. Dauksevicius, C. Sturm, E. Saoutieff, A. Viana, B. Christian, V. Lebedev, J. Radó, I.E. Lukács, M. Grundmann, D. Grosso, C. Loubat: *Design of UV-Crosslinked Polymeric Thin Layers for Encapsulation of Piezoelectric ZnO Nanowires for Pressure-Based Fingerprint Sensors*, J. Mat. Chem. C **6**(3), 605-613 (2018)

K. Brachwitz, T. Böntgen, J. Lenzner, K. Ghosh, M. Lorenz, M. Grundmann: *Evolution of magnetization in epitaxial $Zn_{1-x}Fe_xO_z$ thin films (0 = x = 0.66) grown by pulsed laser deposition*, J. Phys. D: Appl. Phys. **51**(24), 245003:1-7 (2018)

L.J. Brillson, G.M. Foster, J. Cox, W.T. Ruane, A.B. Jarjour, H. Gao, H. von Wenckstern, M. Grundmann, B. Wang, D.C. Look, A. Hyland, M.W. Allen: *Defect Characterization, Imaging, and Control in Wide-Bandgap Semiconductors and Devices*, J. Electr. Mat. **47**(9), 4980-4986 (2018)

J.W. Cox, G.M. Foster, A. Jarjour, H. von Wenckstern, M. Grundmann, L.J. Brillson: *Defect Manipulation to Control ZnO Micro-/Nanowire - Metal Contacts*, Nano Lett. **18**(11), 6974-6980 (2018)

H. Gao, S. Muralidharan, N. Pronin, M.R. Karim, S.M. White, T. Asel, G. Foster, S. Krishnamoorthy, S. Rajan, L.R. Cao, M. Higashiwaki, H. von Wenckstern, M. Grundmann, H. Zhao, D.C. Look, L.J. Brillson: *Optical signatures of deep level defects in Ga_2O_3*, Appl. Phys. Lett. **112**(24), 242102:1-5 (2018)

M. Grundmann: *Elastic Theory of Pseudomorphic Monoclinic and Rhombohedral Heterostructures*, J. Appl. Phys. **124**(18), 185302:1-10 (2018)

M. Grundmann: *Monolithic Forward-looking Photodetector for Use as Ultra-Compact Wavemeter with Wide Spectral Range*, phys. stat. sol. (a) **215**(24), 1800651:1-5 (2018)

M. Grundmann: *Report of The Physics Institutes of Universität Leipzig 2017*, Universität Leipzig, M. Grundmann, ed. (2018)

M. Grundmann: *Report Halbleiterphysik/Semiconductor Physics 2017*, Universität Leipzig, M. Grundmann, ed. (2018)

S. Hohenberger, V. Lazenka, K. Temst, C. Patzig, S. Selle, T. Höche, M. Grundmann, M. Lorenz: *Effect of double layer thickness on magnetoelectric coupling in multiferroic $BaTiO_3$-$Bi_0.95Gd_0.05FeO_3$ multilayers*, J. Phys. D: Appl. Phys. **51**(18), 184002:1-9 (2018)

A. Jarjour, J.W. Cox, W.T. Ruane, H. von Wenckstern, M. Grundmann, L.J. Brillson: *Single Metal Ohmic and Rectifying Contacts to ZnO Nanowires: A Defect Based Approach*, Ann. Phys. **530**(2), 1700335:1-6 (2018)

T. Jawinski, L.A. Wägele, R. Scheer, M. Grundmann, H. von Wenckstern: *Properties of In_2S_3-based pin-heterojunctions*, phys. stat. sol. (a) **215**(11), 1700827:1-6 (2018)

J.K. Jochum, M. Lorenz, H.P. Gunnlaugsson, C. Patzig, T. Höche, M. Grundmann, A. Vantomme, K. Temst, M.J. Van Bael, V. Lazenka: *Impact of magnetization and hyperfine field distribution on high magnetoelectric coupling strength in $BaTiO_3$-$BiFeO_3$ multilayers*, Nanoscale **10**(12), 5574-5580 (2018)

M. Kneiß, P. Storm, G. Benndorf, M. Grundmann, H. von Wenckstern: *Combinatorial material science and strain engineering enabled by pulsed laser deposition using radially segmented targets*, ACS Comb. Sci. **20**, 643-652 (2018)

M. Kneiß, C. Yang, J. Barzola-Quiquia, G. Benndorf, H. von Wenckstern, P. Esquinazi, M. Lorenz, M. Grundmann: *Suppression of grain boundary scattering in p-type transparent γ-CuI thin films due to interface tunneling currents*, Adv. Mater. Interf. **5**(6), 1701411:1-12 (2018)

E. Krüger, V. Zviagin, C. Yang, C. Sturm, R. Schmidt-Grund, M. Grundmann: *Temperature dependence of the dielectric function of thin film CuI in the spectral range (0.6-8.3) eV*, Appl. Phys. Lett. **113**(17), 172102:1-5 (2018)

C. Laube, J. Hellweg, C. Sturm, J. Griebel, M. Grundmann, A. Kahnt, B. Abel: *Photo-Induced-Heating of Graphitised Nanodiamonds monitored by the Raman-Diamond-Peak*, J. Phys. Chem. C **122**, 25685-25691 (2018)

M. Lorenz, S. Hohenberger, E. Rose, M. Grundmann: *Atomically stepped, pseudomorphic, corundum-phase $(Al_{1-x}Ga_x)_2O_3$ thin films ($0 = x < 0.08$) grown on R-plane sapphire*, Appl. Phys. Lett. **113**(23), 231902:1-5 (2018) (Editor's pick)

M. Lorenz:*Pulsed Laser Deposition*, chapter 5, File No. eap810 in Encyclopedia of Applied Physics (Wiley VCH, Weinheim) accepted May 2018, currently in production

T. Meister, F. Ellinger, J.W. Bartha, M. Berroth, J. Burghartz, M. Claus, L. Frey, A. Gagliardi, M. Grundmann, J. Hesselbarth, H. Klauk, K. Leo, P. Lugli, S. Mannsfeld, Y. Manoli, R. Negra, D. Neumaier, U. Pfeiffer, T. Riedl, S. Scheinert, U. Scherf, A. Thiede, G. Troester, M. Vossiek, R. Weigel, C. Wenger, G. Alavi, M. Becherer, C.A. Chavarin, M. Darwish, M. Ellinger, C.-Y. Fan, M. Fritsch, F. Grotjahn, M. Gunia, K. Haase, P. Hillger, K. Ishida, M. Jank, S. Knobelspies, M. Kuhl, G. Lupina, S.M. Naghadeh, N. Münzenrieder, S. Özbek, M. Rasteh, G.A. Salvatore, D. Schrüfer, C. Strobel, M. Theisen, C. Tückmantel, H. von Wenckstern, Z. Wang, Z. Zhang: *Program FFlexCom – High Frequency Flexible Bendable Electronics for Wireless Communication Systems*, 2017 IEEE International Conference on Microwaves, Antennas, Communications and Electronic Systems (COMCAS), p. 1-4 (2018)

T. Michalsky, M. Wille, M. Grundmann, R. Schmidt-Grund: *Tunable and switchable lasing in a ZnO microwire cavity at room temperature*, J. Phys. D: Appl. Phys. **51**(42), 425305:1-6 (2018)

T. Michalsky, M. Wille, M. Grundmann, R. Schmidt-Grund: *Spatiotemporal evolution of coherent polariton modes in ZnO microwire cavities*, Nano Lett. **18**(11), 6820-6825 (2018)

T. Michalsky, M. Wille, E. Krüger, C. Sturm, M. Grundmann, R. Schmidt-Grund: *Coherent polariton states and lasing in ZnO nano- and microstructures*, IEEE Photonics Society Summer Topical Meeting Series, p. 171-172 (2018), ISBN 978-1-5386-4076-0

H. Modarresi, E. Menéndez, V.V. Lazenka, N. Pavlovic, M. Bisht, M. Lorenz, C. Petermann, M. Grundmann, A. Hardy, M.K. Van Bael, M.J. Van Bael, A. Vantomme, K. Temst: *Morphology-induced spin frustration in granular $BiFeO_3$ thin films: Origin of the magnetic vertical shift*, Appl. Phys. Lett. **113**(14), 142402:1-5 (2018)

R. Pickenhain, M. Schmidt, H. von Wenckstern, G. Benndorf, A. Pöppl, R. Böttcher, M. Grundmann: *Negative U Properties of the Deep Level E3 in ZnO*, phys. stat. sol. (b) **255**, 1700670:1-16 (2018)

V. Prozheeva, R. Hölldobler, H. von Wenckstern, M. Grundmann, F. Tuomisto: *Effects of alloy composition and Si-doping on vacancy defect formation in $(In_xGa_{1-x})_2O_3$ thin films*, J. Appl. Phys. **123**(12), 125705:1-6 (2018)

S. Prucnal, Y. Berencén, M. Wang, J. Grenzer, M. Voelskow, R. Hübner, Y. Yamamoto, A. Scheit, F. Bärwolf, V. Zviagin, R. Schmidt-Grund, M. Grundmann, J. Zuk, M. Turek, A. Drozdziel, K. Pyszniak, R. Kudrawiec, M.P. Polak, L. Rebohle, W. Skorupa, M. Helm, S. Zhou: *Strain and band gap engineering in GeSn alloys via P doping*, Phys. Rev. Appl. **10**(6), 064055:1-11 (2018)

S. Richter, J Zúñiga-Pérez, C. Deparis, L. Trefflich, H.-G. Zirnstein, T. Michalsky, C. Sturm, B. Rosenow, M. Grundmann, R. Schmidt-Grund: *Exceptional Points in the Dispersion of Optically Anisotropic Planar Microcavities*, IEEE Photonics Society Summer Topical Meeting Series, p. 195-196 (2018), ISBN 978-1-5386-4076-0

T. Schulz, S. Bitter, P. Schlupp, H. von Wenckstern, N. Koch, M. Grundmann: *The influence of oxygen deficiency on the rectifying behavior of transparent semiconducting oxide-metal interfaces* , Phys. Rev. Appl. **9**, 064001:1-8 (2018) (Editor's suggestion)

D. Splith, S. Müller, H. von Wenckstern, M. Grundmann: *Modeling of Schottky barrier diode characteristics on heteroepitaxial β-gallium oxide thin films*, Proc. SPIE **10533**, 105330C:1-8 (2018), David J. Rogers, David C. Look, Ferechteh H. Teherani, eds.

S. Vogt, H. von Wenckstern, M. Grundmann: *MESFETs and inverters based on amorphous zinc-tin-oxide thin films prepared at room temperature*, Appl. Phys. Lett. **113**(13), 133501:1-5 (2018)

Talks

S. Espinoza, M. Rebarz, S. Richter, O. Herrfurth, M. Kloz, R. Schmidt-Grund, J. Andreasson, S. Zollner: *Phase-Filling Singularities in Femtosecond Transient Dielectric Spectra of Germanium*, DPG spring meeting, Berlin, Germany, March 2018

M. Grundmann: *Neues zur Kristalloptik bei Dissipation: Singuläre Achsen und Topologie Exzeptioneller Punkte*, Sächsische Akademie der Wissenschaften zu Leipzig, Plenarvortrag, Leipzig, Germany, June 2018 (invited)

M. Grundmann: *Birefringence in the Absorption Regime: Singular Optic Axes and Exceptional Points*, International and dissemination workshop of the Research Unit FOR1616, Weimar, Germany, September 2018 (invited)

M. Grundmann: *Birefringence Effects in Transparent Conductive Materials or Singular and Topological Optical States*, 7th International Symposium on Transparent Conductive Materials (TCM-7), Chania, Crete, Greece, October 2018 (invited)

M. Grundmann, C. Yang, E. Rose, M. Kneiß, P. Schlupp, Z. Zhang, H. von Wenckstern, M. Lorenz: *Towards High Performance p-Type Transparent Conductors and Semiconductors with Copper Iodide*, 7th International Symposium on Transparent Conductive Materials (TCM-7), Chania, Crete, Greece, October 2018

O. Herrfurth, S. Richter, M. Rebarz, S. Espinoza, J. Zúñiga-P'erez, A. Schleife, J. Leveilee, S. Zollner, J. Andreasson, M. Grundmann, R. Schmidt-Grund: *Transient birefringence and dichroism of a m-ZnO film studied by tSE*, 3rd ELIps Workshop, Dolní Brezany, Czech Republic, October 2018 (invited)

S. Hohenberger, J. Jochum, K. Temst, M. Lorenz, M. Grundmann: *Thickness dependent magnetoelectric coupling in $BaTiO_3$-$BiFeO_3$ multilayers*, E-MRS Fall Meeting, Warsaw, Poland, September 2018

M. Kneiß, P. Storm, G. Benndorf, H. von Wenckstern, M. Grundmann: *A pulsed laser deposition technique for continuous variation of alloy composition in growth direction: Demonstration on the transparent $Mg_xZn_{1-x}O$ alloy system*, Annual BuildMoNa Conference 2018, Leipzig, Germany, March 2018

M. Kneiß, P. Storm, G. Benndorf, H. von Wenckstern, M. Grundmann: *A pulsed laser deposition technique to control the composition of ternary thin films in growth direction demonstrated on the $Mg_xZn_{1-x}O$ alloy*, DPG Spring Meeting 2018, Berlin, Germany, March 2018

M. Kneiß, P. Storm, G. Benndorf, H. von Wenckstern, M. Grundmann: *A pulsed laser deposition technique for continuous variation of alloy composition in growth direction: Demonstration on the transparent $Mg_xZn_{1-x}O$ alloy system*, Electronic Materials Conference 2018, Santa Barbara, California, USA, June 2018

M. Kneiß, A. Hassa, D. Splith, H. von Wenckstern, M. Grundmann: *PLD-growth of ternary β-$(Al_xGa_{1-x})_2O_3$ thin films with $x \leq 0.28$ using a single elliptically-segmented target*, E-MRS Fall Meeting 2018, Warsaw, Poland, September 2018

E. Krüger, V. Zviagin, C. Yang, R. Schmidt-Grund, M. Grundmann: *Temperature dependent dielectric function of CuI*, DPG spring meeting, Berlin, Germany, March 2018

E. Krüger, V. Zviagin, C. Yang, R. Schmidt-Grund, M. Grundmann: *Temperature dependent dielectric function of CuI thin films*, 10th Workshop Ellipsometry, Chemnitz, Germany, March 2018

M. Lorenz: *Pulsed Laser Deposition of functional oxides for electronic applications*, Technische Hochschule Deggendorf, AG Prof. Benstetter, Deggendorf, Germany, April 2018

M. Lorenz, V. Lazenka, S. Hohenberger, C. Patzig, S. Selle, D. Hirsch, T. Höche, K. Temst, M. Grundmann: *Origin of high magnetoelectric coupling in multiferroic Bi(Gd)FeO_3-$BaTiO_3$ superlattices: Chemical interface features by TOF-SIMS and STEM-EDX*, 14th International Ceramic Congress at CIMTEC 2018, Perugia, Italy, June 2018

M. Lorenz, V. Lazenka: *Magnetoelectric coupling in multiferroic epitaxial $BiFeO_3$-$BaTiO_3$ thin film composites*, Qufu Normal University, Qufu, China, September 2018

T. Michalsky, M. Wille, E. Krüger, C. Sturm, M. Grundmann, R. Schmidt-Grund: *Coherent polariton states and lasing in ZnO nano- and microstructures*, IEEE Photonics Society Summer Topical Meeting, Waikoloa, Hawaii, USA, July 2018

S. Richter, O. Herrfurth, S. Espinoza, M. Rebarz, M. Kloz, J. Andreasson, M. Grundmann, R. Schmidt-Grund: *Time-resolved spectroscopic ellipsometry with sub-ps resolution*, DPG spring meeting, Berlin, Germany, March 2018

S. Richter, O. Herrfurth, S.J. Espinoza Herrera, M. Rebarz, M. Grundmann, S. Zollner, J. Andreasson, R. Schmidt-Grund: *fs-time-resolved spectroscopic ellipsometry*, 10th Workshop Ellipsometry, Chemnitz, Germany, March 2018 (Winner of the Paul Drude Medal 2018)

S. Richter, J. Zúñiga-Pérez, C. Deparis, L. Trefflich, H.-G. Zirnstein, T. Michalsky, C. Sturm, B. Rosenow, M. Grundmann, R. Schmidt-Grund: *Exceptional Points in the Dispersion of Optically Anisotropic Planar Microcavities*, IEEE Photonics Society Summer Topical Meeting, Waikoloa, Hawaii, USA, July 2018

S. Richter, S. Espinoza, M. Rebarz, J. Andreasson, O. Herrfurth, R. Schmidt-Grund, S. Zollner: *Time-resolved VIS-UV spectroscopic ellipsometry at ELI Beamlines*, 3rd ELIps Workshop, Dolní Brezany, Czech Republic, October 2018 (invited)

P. Schlupp, S. Bitter, H. von Wenckstern, M. Grundmann: *Room temperature fabricated junction field-effect transistors and inverters on rigid and flexible substrates*, DPG spring meeting, Berlin, Germany, March 2018

R. Schmidt-Grund,T. Michalsky, M. Wille, E. Krüger, R. Buschlinger, C. Sturm, H. Franke, U. Peschel, M. Grundmann: *Coherent polariton modes and lasing in ZnO nano- and microstructures*, 34th International Conference on the Physics of Semiconductors, ICPS2018, Montpellier, France, July/August 2018

R. Schmidt-Grund, C. Sturm, C. Kranert, J. Furthmüller, F. Bechstedt, D. Fritsch, M. Grundmann: *Dielectric Function Tensor of Anisotropic Crystals*, 3rd ELIps Workshop, Dolní Brezany, Czech Republic, October 2018 (invited)

R. Schmidt-Grund: *Some Examples for Ellipsometry in Leipzig: Electronic and Magnetic Properties, Dynamics and Low-Symmetry Materials*, Colloquium, Department of Physics, New Mexico State University, Las Cruces, NM, USA, July 2018 (invited)

R. Schmidt-Grund: *Dynamics of hot charge carriers and phonons as well as lasing in ZnO*, Colloquium, Koszalin University of Technology, Koszalin, Poland, October 2018 (invited)

D. Splith, H. von Wenckstern, M. Grundmann: *Schottky diodes on gallium-oxide and indium-oxide thin-films: optimization of the sample structure and modeling of the IV characteristics*, SPIE Photonics West, San Francisco, USA, January 2018

C. Sturm, A. Werner, V. Zviagin, D. Splith, H. von Wenckstern, M. Lorenz, J. Lenzner, R. Schmidt-Grund, M. Grundmann: *Dielectric function of epsilon-(In,Ga)$_2$O$_3$ thin films*, 10th Workshop Ellipsometry, Chemnitz, Germany, March 2018

C. Sturm: *Crystal optics and tensor properties of low symmetry crystals*, EPIOPTICS-15, Erice, Italy, July 2018 (invited)

C. Sturm, A. Werner, V. Zviagin, D. Splith, H. von Wenckstern, M. Lorenz, J. Lenzner, R. Schmidt-Grund, M. Grundmann: *Dielectric function and Raman tensor of epsilon-(In,Ga)$_2$O$_3$ thin films*, 34th International Conference on the Physics of Semiconductors, ICPS2018, Montpellier, France, July/August 2018 (invited)

C. Sturm, V. Zviagin, M. Grundmann: *Determination of the pseudo-gyration tensor of KTP by ellipsometry*, 2nd International Workshop on Biophotonics and Optical Angular Momentum, Palaiseau, France, October 2018

C. Sturm: *Crystal optics and tensor properties of low symmetry crystals*, Fakultätsseminar (Universität Linz), Linz, Austria, May 2018 (invited)

C. Sturm: *Crystal optics and tensor properties of low symmetry crystals*, Gruppenseminar (Prof. Wiersig), Magdeburg, Germany, December 2018 (invited)

H. von Wenckstern, A. Werner, M. Kneiß, D. Splith, F. Storm, M. Grundmann: *Properties of ternary, kappa-phase group-III sesquioxides*, 2nd Annual GraFOx Meeting, Humboldt-Universität zu Berlin, Berlin, Germany, July 2018

H. von Wenckstern: *Exploration of ternary semiconducting oxides by compositional screening*, E-MRS Fall Meeting, Warsaw, Poland, September 2018

C. Yang: *ZnGaON project - Wurtzite zinc-based oxynitrides as promising photovoltaic absorbers*, Kick-Off Meeting ZONE, Valbonne, France, April 2018

C. Yang, M. Kneiß, P. Schlupp, Z. Zhang, H. von Wenckstern, M. Lorenz, M. Grundmann: *Copper Iodide, a High-Performance p-Type Wide Bandgap Semiconductor*, 34th International Conference on the Physics of Semiconductors (ICPS), Montpellier, France, July 2018

M. Zapf, R. Röder, K. Winkler, L. Kaden, J. Greil, M. Wille, M. Grundmann, R. Schmidt-Grund, A. Lugstein, C. Ronning: *Dynamical Tuning of Nanowire Laser Spectra*, DPG spring meeting, Berlin, Germany, March 2018

V. Zviagin, P. Huth, C. Sturm, J. Lenzner, A. Setzer, R. Denecke, P. Esquinazi, M. Grundmann, R. Schmidt-Grund: *Cationic Configuration in Relation to Magnetic Properties of PLD Grown Spinel Ferrite Thin Films*, Collaborative Research Centre SFB 762: Functionality of Oxide Interfaces International Workshop, Frauenchiemsee, Germany, February/March 2018

V. Zviagin, Y. Kumar, C. Sturm, I. Lorite, P. Esquinazi, M. Grundmann, R. Schmidt-Grund: *The Influence of Crystallographic Order on Ferrimagnetic Response of Spinel $ZnFe_2O_4$ Thin Films*, DPG spring meeting, Berlin, Germany, March 2018

V. Zviagin, P. Huth, C. Sturm, M. Bonholzer, J. Lenzner, A. Setzer, R. Denecke, P. Esquinazi, M. Grundmann, R. Schmidt-Grund: *Spectroscopic investigation of cation configuration state of Spinel Ferrite thin films*, 10th Workshop Ellipsometry, Chemnitz, Germany, March 2018

Posters

K. Dorywalski, M. Grundmann, R. Schmidt-Grund: *Hybrid GA-gradient method for thin films ellipsometric data evolution*, 10th Workshop Ellipsometry, Chemnitz, Germany, March 2018

S. Espinoza, S. Zollner, S. Richter, M. Rebarz, O. Herrfurth, R. Schmidt-Grund, J. Andreasson: *Phase-filling singularities in femtosecond transient dielectric spectra of Germanium*, International Science@FELs Conference, Stockholm, Sweden, June 2018

O. Herrfurth, S. Richter, M. Rebarz, M. Kloz, S. Espinoza, J. Andreasson, M. Grundmann, R. Schmidt-Grund: *Time-resolved dielectric function tensor of m-plane ZnO studied by femtosecond spectroscopic ellipsometry*, DPG spring meeting, Berlin, Germany, March 2018

O. Herrfurth, S. Richter, S.J. Espinoza Herrera, M. Rebarz, M. Grundmann, S. Zollner, J. Andreasson, R. Schmidt-Grund: *Pitfalls of time-resolved spectroscopic ellipsometry*, 10th Workshop Ellipsometry, Chemnitz, Germany, March 2018

O. Herrfurth, S. Richter, S. Espinoza, M. Rebarz, M. Kloz, J. Andreasson, M. Grundmann, R. Schmidt-Grund: *Charge carrier dynamics of ZnO structures studied with femtosecond-time-resolved spectroscopic ellipsometry*, 34th International Conference on the Physics of Semiconductors, ICPS2018, Montpellier, France, July/August 2018

F. Jung, S. Ellis, C. Sturm, R. Schmidt-Grund, M. Lorenz, M. Grundmann, C. Patzig, S. Selle, T. Höche: *Optical and structural properties of PLD-grown TiN single layers and TiN/MgO superlattices on MgO(100) substrates*, DPG spring meeting, Berlin, Germany, March 2018

M. Kneiß, A. Hassa, D. Splith, C. Sturm, H. von Wenckstern, T. Schultz, N. Koch, M. Lorenz, M. Grundmann: *PLD-growth of epitaxial κ-Ga_2O_3 thin films on different substrates*, E-MRS Fall Meeting 2018, Warsaw, Poland, September 2018

E. Krüger, M. Wille, S. Blaurock, V. Zviagin, R. Deichsel, G. Benndorf, V. Gottschalch, H. Krautscheid, R. Schmidt-Grund, M. Grundmann: *Optical properties of highly excited CuI based microwire cavities*, DPG spring meeting, Berlin, Germany, March 2018

E. Krüger, V. Zviagin, C. Yang, R. Schmidt-Grund, M. Grundmann: *Temperature dependent dielectric function of CuI*, 34th International Conference on the Physics of Semiconductors, ICPS2018, Montpellier, France, July/August 2018

E. Krüger, M. Wille, S. Blaurock, V. Zviagin, R. Deichsel, G. Benndorf, L. Trefflich, V. Gottschalch, H. Krautscheid, R. Schmidt-Grund, M. Grundmann: *Lasing in CuI microwires*, 34th International Conference on the Physics of Semiconductors, ICPS2018, Montpellier, France, July/August 2018

E. Krüger, V. Zviagin, C. Yang, R. Schmidt-Grund, M. Grundmann: *Temperature dependent dielectric function of CuI*, 3rd ELIps Workshop, Dolní Brezany, Czech Republic, October 2018

O. Lahr, S. Vogt, Z. Zhang, H. von Wenckstern, M. Grundmann: *Devices and integrated circuits based on amorphous zinc-tin-oxide*, DPG spring meeting, Berlin, Germany, March 2018

M. Grundmann, S. Hohenberger, M. Lorenz: *Pseudomorphic Strain in Monoclinic and Rhombohedral Heterostructures*, 34th International Conference on the Physics of Semiconductors, ICPS2018, Montpellier, France, July/August 2018

T. Michalsky, M. Wille, E. Krüger, M. Grundmann, R. Schmidt-Grund: *Dynamics of coherent polariton modes and tunable lasing in ZnO microwire cavities at room temperature*, International Conference on Superlattices, Nanostructures and Nanodevices, Madrid, Spain, July 2018

A. Reinhardt, H. von Wenckstern, M. Grundmann: *Electrical properties of unipolar devices based on amorphous zinc oxynitride*, DPG spring meeting, Berlin, Germany, March 2018

S. Richter, J. Zúñiga-Pérez, C. Deparis, L. Trefflich, H.-G. Zirnstein, T. Michalsky, C. Sturm, B. Rosenow, M. Grundmann, R. Schmidt-Grund: *Exceptional Points in the Dispersion of Optically Anisotropic Planar Microcavities*, International Conference on Superlattices, Nanostructures and Nanodevices, Madrid, Spain, July 2018

S. Richter, S. Espinoza, M. Rebarz, O. Herrfurth, M. Kloz, M. Rübhausen, M. Grundmann, R. Schmidt-Grund, S. Zollner, J. Andreasson: *Fs-time-resolved ellipsometry to study the dynamics in the electronic density of states*, 34th International Conference on the Physics of Semiconductors, ICPS2018, Montpellier, France, July/August 2018

S. Richter, J. Zúñiga-Pérez, C. Deparis, L. Trefflich, H.G. Zirnstein, C. Sturm, B. Rosenow, M. Grundmann, R. Schmidt-Grund: *Exceptional points in planar semiconductor-microcavities of optically anisotropic media*, 34th International Conference on the Physics of Semiconductors, ICPS2018, Montpellier, France, July/August 2018

D. Splith, S. Lanzinger, S. Müller, C. Sturm, H. von Wenckstern, M. Grundmann: *Influence of Ga incorporation into bixbyite In_2O_3 thin films on the performance of Schottky barrier diodes thereon*, DPG spring meeting, Berlin, Germany, March 2018

C. Sturm, M. Grundmann: *Dielectric Function and Singular Optic Axes of KTP*, 10th Workshop Ellipsometry, Chemnitz, Germany, March 2018

C. Sturm, M. Grundmann: *Dielectric Function and Singular Optic Axes of KTP*, 34th International Conference on the Physics of Semiconductors, ICPS2018, Montpellier, France, July/August 2018

L. Trefflich, F. Dissinger, M. Kakei, C. Sturm, S.R. Waldvogel, M. Grundmann, R. Schmidt-Grund: *Optical properties of carbon nanodots as active material in planar microcavities*, DPG spring meeting, Berlin, Germany, March 2018

L. Trefflich, F. Dissinger, C. Sturm, S.R. Waldvogel, M. Grundmann, R. Schmidt-Grund: *Carbon nanodot based planar microcavities*, International and dissemination work shop of the research unit FOR1616, Weimar, Germany, September 2018

A. Werner, H. von Wenckstern, M. Grundmann: *Investigations of Ge-doped (Al,Ga)$_2O_3$ thin films*, DPG spring meeting, Berlin, Germany, March 2018

A. Werner, R. Hoelldobler, V. Prozheeva, D. Splith, C. Sturm, H. von Wenckstern, M. Grundmann: *Occurence of the ϵ-phase in (In_xGa_{1-x})2O3 and (Ga_xAl_{1-x})$_2O_3$ thin films*, DPG spring meeting, Berlin, Germany, March 2018

A. Werner, H. von Wenckstern, M. Grundmann: *Influence of growth conditions on deposition of $\beta-$ and ϵ-phase (Al,Ga)$_2O_3$ thin films grown by PLD on sapphire substrates*, Annual BuildMoNa Conference, Leipzig, Germany, March 2018

V. Zviagin, P. Huth, C. Sturm, J. Lenzner, A. Setzer, R. Denecke, P. Esquinazi, M. Grundmann, Rüdiger Schmidt-Grund: *Optical and Magnetic Properties of PLD Grown Spinel Ferrite Thin Films in Relation to their Cation Configuration*, Collaborative Research Centre SFB 762: Functionality of Oxide Interfaces, International Workshop, Frauenchiemsee, Germany, February/March 2018

V. Zviagin, P. Huth, C. Sturm, D. Spemann, S. Mändl, J. Lenzner, A. Setzer, J. Meijer, R. Denecke, P. Esquinazi, M. Grundmann, R. Schmidt-Grund: *Optical and Magnetic Properties of Spinel Type Ferrites in Relation to their Crystallographic Order*, DPG spring meeting, Berlin, Germany, March 2018

V. Zviagin, P. Huth, C. Sturm, J. Lenzner, A. Setzer, R. Denecke, P. Esquinazi, M. Grundmann, R. Schmidt-Grund: *Spinel Ferrite Bulk and Surface Cation and Defect Contribution to the Ferrimagnetic Response*, International Conference on Magnetism, San Francisco, USA, July 2018

V. Zviagin, P. Huth, C. Sturm, J. Lenzner, A. Setzer, R. Denecke, P. Esquinazi, M. Grundmann, R. Schmidt-Grund: *Bulk and Surface Cation Configuration Investigation of PLD Grown Spinel Ferrites in Relation to the Magnetic Response*, 34th International Conference on the Physics of Semiconductors, ICPS2018, Montpellier, France, July/August 2018

V. Zviagin, P. Huth, C. Sturm, J. Lenzner, A. Setzer, R. Denecke, P. Esquinazi, M. Grundmannm, R. Schmidt-Grund: *Spinel Ferrite Bulk and Surface Cation and Defect Contribution to the Ferrimagnetic Response*, 3rd ELIps Workshop, Dolní Brezany, Czech Republic, October 2018

5

Graduations

Doctorate

- Robert Karsthof
  NiO/ZnO-Heteroübergänge: Charakterisierung des elektrischen Transports und Realisierung transparenter aktiver Bauelemente
  February 2018
- Tom Michalsky
  Propagating exciton-polariton states in one- and two-dimensional ZnO-based cavity systems
  April 2018
- Marcus Purfürst
  Influence of Soot on the Transport Mechanisms inside the Filter Wall of SCR-Coated Diesel Particulate Filters
  April 2018
- Anna Reinhardt
  Amorphes Zinkoxinitrid - Untersuchung einer vielversprechenden Alternative zu amorphen Oxidhalbleitern
  January 2018
- Steffen Richter
  Optically aniostropic planar microcavities
  January 2018
- Peter Schlupp
  Funktionelle amorphe Dünnschichten: Bauelemente auf Basis von Zink-Zinn-Oxid
  February 2018
- Peter Schwinkendorf
  Magnetoelektrische Kopplung in $BaTiO_3$- und $BiFeO_3$-Kompositschichten und Leitfähigkeitsphänomene in Sr_2FeMoO_6-Dünnschichten
  April 2018
- Alexander Shkurmanov
  ZnO-based nanostructures by PLD: growth mechanism, doping and geometry
  April 2018

- Marcel Wille
  ZnO- und CuI-Nano- und Mikrostrukturen: Laseremission und Komplexer Brechungsindex
  February 2018

Master

- Rafael Deichsel
  Untersuchung von Kupferiodid-Kristallen mittels Photolumineszenz
  January 2018
- Rebecca Sabine Hölldobler
  Eigenschaften von $(GaIn)_2O_3$ Dünnfilmen
  March 2018
- Florian Jung
  Optical and structural properties of TiN/MgO superlatties
  October 2018
- Evgeny Krüger
  Optische Eigenschaften von CuI-Dünnschichten und -Mikrodrähten
  May 2018
- Steffen Lanzinger
  Untersuchung von Schottkydioden auf kubischem $(Ju,Ga)_2O_3$
  March 2018

Bachelor

- Philipp Bischoff
  Herstellung und elektrische Charakterisierung von ZTO-basierten MESFETs
  January 2018
- Misuki Kakei
  The determination of the suitability of the gelatine as cavity material for planar microcavity
  October 2018
- Sandra Montag
  Modification of transparent NiO/ZnO-heterojunctions by gradual substitution with MgO
  October 2018
- Andreas Müller
  Untersuchung der optischen Phonenmoden von epsilon-Galliumoxid
  October 2018
- Sophie Müller
  Herstellung und Charakterisierung von Molybdäntrioxid-Mikroflakes
  February 2018

6

Guests

- Dr.-Ing. Krzysztof Grzegorz Dorywalski
  Politechnika Koszalinska, Koszalin, Poland
  October 2017 – June 2018
- Michitaka Fukumoto
  Japan Society for the Promotion of Science: Overseas Challenge Program for Young Researchers
  April 2018 – March 2019
- Dr. Wenlei Yu
  Wenzhou Medical University, Zhejiang, PR China
  August 2018 – July 2019

Author Index

S

T

V

W

Y

Z

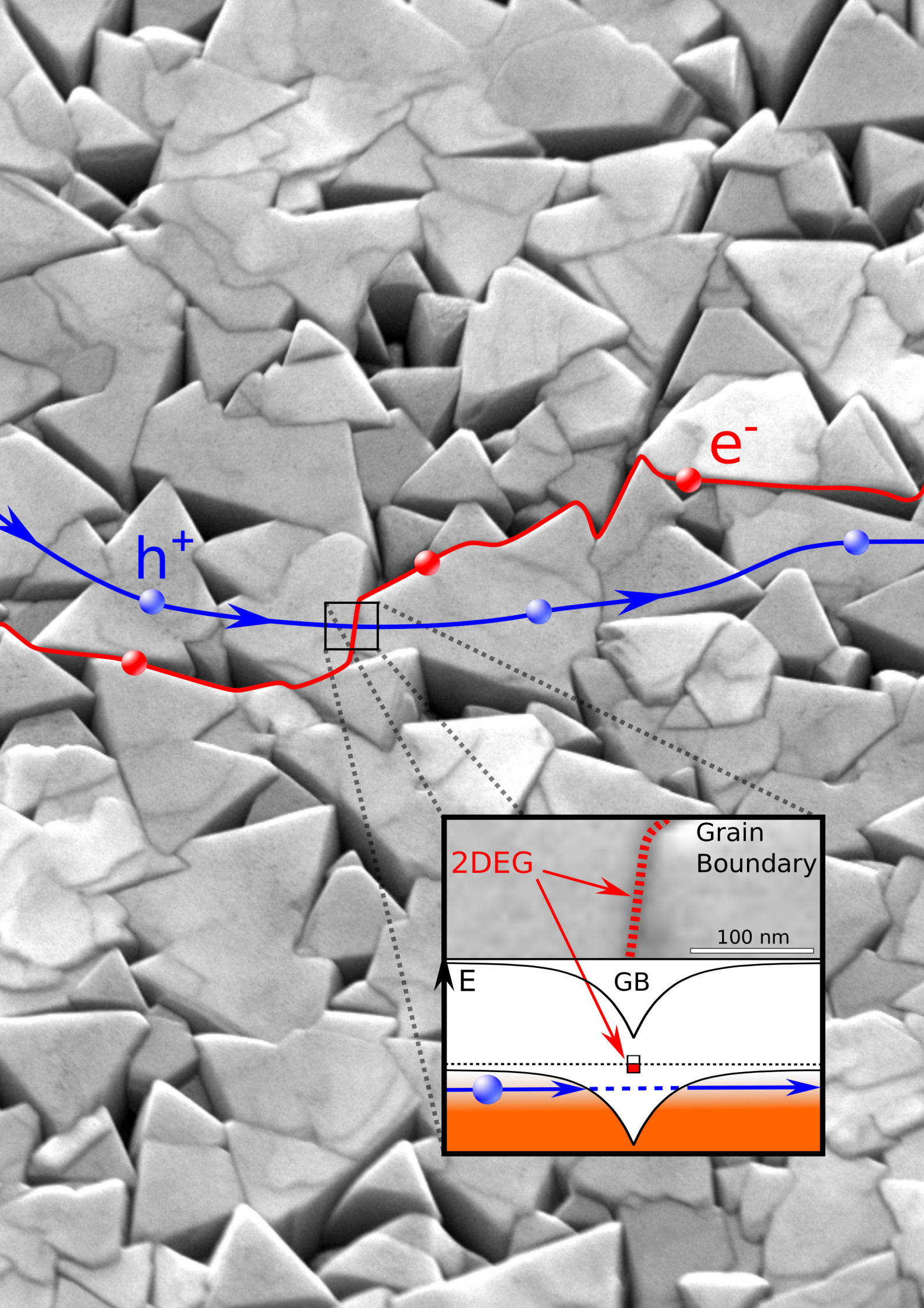
e-
h+
2DEG
Grain
Boundary
100 nm
E
GB